



HAL
open science

Population-Based Models of Shape, Structure, and Deformation in Atrial Fibrillation

Shuman Jia

► **To cite this version:**

Shuman Jia. Population-Based Models of Shape, Structure, and Deformation in Atrial Fibrillation. Medical Imaging. Université Côte d'Azur, 2019. English. NNT: . tel-02428638v1

HAL Id: tel-02428638

<https://inria.hal.science/tel-02428638v1>

Submitted on 6 Jan 2020 (v1), last revised 2 Jan 2022 (v2)

HAL is a multi-disciplinary open access archive for the deposit and dissemination of scientific research documents, whether they are published or not. The documents may come from teaching and research institutions in France or abroad, or from public or private research centers.

L'archive ouverte pluridisciplinaire **HAL**, est destinée au dépôt et à la diffusion de documents scientifiques de niveau recherche, publiés ou non, émanant des établissements d'enseignement et de recherche français ou étrangers, des laboratoires publics ou privés.

THÈSE DE DOCTORAT

Statistiques de forme, de structure et de
déformation à l'échelle d'une population pour
l'étude de la fibrillation auriculaire

Population-Based Models of Shape, Structure, and
Deformation in Atrial Fibrillation

Shuman JIA

INRIA, Équipe EPIONE

Thèse dirigée par Maxime SERMESANT et co-dirigée par Xavier PENNEC

Soutenue le 18 décembre 2019

Présentée en vue de l'obtention du grade de DOCTEUR EN AUTOMATIQUE,
TRAITEMENT DU SIGNAL ET DES IMAGES de l'UNIVERSITÉ CÔTE D'AZUR.

Devant le jury composé de :

Silvia SCHIEVANO	University College London, Royaume-Uni	Rapporteur
Sarang JOSHI	University of Utah, États-Unis	Rapporteur
Joakim SUNDNES	Simula Research Laboratory, Norvège	Examineur
Vicente ZARZOSO	I3S, IUT Nice, France	Président
Maxime SERMESANT	Inria Sophia Antipolis, France	Directeur de thèse
Xavier PENNEC	Inria Sophia Antipolis, France	Co-directeur de thèse

Résumé

La fibrillation auriculaire (FA) est le type d'arythmie cardiaque le plus commun, caractérisée par une activation électrique chaotique et une contraction non synchronisée des oreillettes. Cette maladie et ses complications potentiellement mortelles ainsi que sa progression rapide exigent de diagnostiquer et de mettre en place un traitement efficace dès que possible. L'ablation par cathéter, une procédure invasive qui établit des lésions pour bloquer les points de déclenchement de la FA et la propagation de l'arythmie, est un traitement efficace pour les patients réfractaires aux médicaments. Cependant, pour 30% des patients, la FA se redéveloppe, entraînant des interventions d'ablation multiples et affectant la fonction mécanique auriculaire.

Le but de cette étude est de combiner l'expertise mathématique et informatique à la médecine afin de mieux comprendre la physiologie sous-jacente à la FA et de fournir des outils d'aide à la décision aux cliniciens. Nous analysons des corrélations entre l'arythmie récurrente et les caractéristiques du patient avant l'ablation, y compris la forme de l'oreillette gauche extraite d'images tomographiques. Nous développons pour ce faire des méthodes semi-automatiques pour segmenter l'oreillette gauche et sa paroi à partir d'images. Ensuite, nous avons obtenu de bons résultats de segmentation avec un modèle de réseau de neurones artificiels. En outre, nous étudions des marqueurs de forme liés au remodelage global et local, et la quantification du tissu adipeux, en combinant une approche morphométrique différentiable à une analyse statistique. Enfin, le travail s'étend à l'analyse statistique de la déformation temporelle. Nous proposons une reformulation symétrique de l'échelle de perroquet qui améliore la cohérence et la stabilité numérique.

Mots clés : analyse d'images cardiaques, fibrillation auriculaire, segmentation, graisse, analyse statistique des formes, transport parallèle.

Résumé étendu en français

Contexte

La fibrillation atriale (FA) est le type d'arythmie cardiaque le plus commun. Elle est caractérisée par une activation électrique chaotique des oreillettes empêchant la contraction synchronisée du cœur. Cette maladie affecte aujourd'hui plus de 6 millions de personnes en Europe. Ses complications potentiellement mortelles ainsi que sa progression rapide exigent de diagnostiquer et de mettre en place un traitement efficace dès que possible.

L'ablation par cathéter, une procédure invasive qui établit des lésions pour bloquer les points de déclenchement de la FA et la propagation de l'arythmie, est un traitement efficace pour la FA et peut être recommandée pour les patients réfractaires aux médicaments. Pourtant, pour 30% des patients, la FA se redéveloppe, entraînant des interventions d'ablation multiples.

Objectifs

Le but de ce projet est de combiner l'expertise mathématique et informatique à la médecine afin de mieux comprendre la physiologie sous-jacente à la FA et de fournir des outils d'aide à la décision aux cliniciens. L'évaluation de l'état pathologique d'un patient FA pour prédire la récurrence d'une arythmie après ablation est essentielle pour améliorer le traitement des patients tout en évitant des interventions risquées et coûteuses.

Nous travaillons en étroite collaboration avec le CHU de Bordeaux, où 300 à 500 patients subissent une procédure d'ablation chaque année. Nous avons choisi de diviser ce projet en quatre étapes :

- Développement de méthodes automatiques pour segmenter l'oreillette gauche à partir d'images tomodensitométriques.
- Développement de méthodes automatiques pour segmenter la paroi de l'oreillette et les tissus adipeux du myocarde.

-
- Analyse des corrélations entre les caractéristiques de la forme de l'oreillette et l'arythmie récurrente à partir d'une base de données de 150 images tomodensitométriques.
 - Extension de l'analyse par l'étude statistique des déformations au sein de chaque groupe.

Segmentation de l'oreillette gauche

La segmentation automatique de l'oreillette gauche est une tâche non triviale. Nous avons dans un premier temps proposé une méthode semi-automatique. Les cliniciens définissent d'abord les limites de la région d'intérêt sur des images à l'aide du logiciel MUSIC. Ensuite, un algorithme de croissance de région avec un seuillage personnalisé est utilisé. Cette méthode intègre des contraintes spatiales, des informations d'intensité fournies par l'utilisateur et des connaissances cliniques sur la structure de l'oreillette gauche.

Pour entièrement automatiser cette tâche, nous avons entraîné des U-Nets en 3D en utilisant l'apprentissage profond, qui localisent et segmentent l'oreillette gauche avec une haute efficacité. Une fonction de coût basée sur le contour a été conçue pour ajuster la segmentation finale. Les résultats montraient une distance de Hausdorff plus petite et des erreurs moins granulaires. Nous avons amélioré la robustesse en utilisant une technique d'ensemble consistant à combiner plusieurs U-Nets dans un modèle plus puissant.

Tissus du myocarde

Une mesure précise de l'épaisseur de la paroi atriale aide à déterminer la dose de radiofréquence nécessaire pour créer des lésions au travers du mur. La plupart des travaux d'évaluation des structures atriales reposent sur des mesures en 2D plutôt que sur une segmentation, qui est une tâche difficile étant donné la finesse de la paroi, la qualité insuffisante de l'image et des structures voisines similaires.

Nous présentons un modèle de contour actif géodésique contrôlé par marqueur (MC-GAC) pour segmenter indirectement l'épicarde auriculaire gauche, en tenant compte des contraintes externes de son environnement. Cette méthode exploite les informations de valeur d'intensité spécifiques au patient et son environnement. Les résultats ont permis d'obtenir une bonne correspondance sur l'épaisseur de la paroi avec la segmentation manuelle. Notre méthode est robuste en cas d'artefacts.

Ces segmentations préliminaires ont été utilisées comme supervision faible pour entraîner un réseau U-Net, au cours duquel nous avons observé un effet de "compensation". Le réseau a pu apprendre que la cible était du tissu musculaire et n'était pas égaré par des erreurs inévitables par MC-GAC.

Analyse des formes

Dans le cadre du projet Européen ERA CoSysMed SysAFib qui vise à fournir une prédiction du succès de l’ablation, nous nous sommes intéressés aux marqueurs de forme liés à l’apparition de problèmes post-ablation dans la FA. Nous combinons pour ce faire une approche morphométrique difféomorphe à une régression des moindres carrés partiels.

Nous avons d’abord calculé une forme moyenne de l’oreillette gauche, puis établi une correspondance point à point entre les anatomies spécifiques des patients et le modèle. Une régression par moindres carrés partiels appliquée à un encodage de ces déformations difféomorphes améliore la prédiction relativement aux résultats pouvant être obtenus en utilisant le volume atrial gauche.

Enfin, nous avons identifié les régions critiques dont le remodelage local était associé à la récurrence de l’arythmie. Les résultats, tant au niveau global que régional, pourraient aider à mieux sélectionner les patients et conduire à des cibles potentielles d’ablation en dehors des veines pulmonaires pour la planification du traitement.

Analyse des déformations

Le mouvement cardiaque contient des informations sous-jacentes à la progression des maladies. Pour modéliser les mouvements, la normalisation des trajectoires temporelles est nécessaire dans un premier temps en raison de la variabilité anatomique entre les sujets. Cela peut se faire par un algorithme de transport parallèle dit de ‘l’échelle de perroquet’.

L’échelle de perroquet s’est récemment révélée être un schéma de troisième ordre dans les espaces de connexion affines généraux et exact dans les espaces symétriques affines. Nous améliorons ce schéma avec une reformulation plus stable, qui repose sur des géodésiques symétriques autour des points centraux. De plus, nous proposons un continuum de décompositions de l’espace de forme, prenant en compte les résidus des recalages difféomorphes.

Nous appliquons cette méthode pour analyser le mouvement cardiaque parmi les populations d’hypertension pulmonaire. L’évaluation est réalisée sur une base de données cardiaques 4D avec des maillages du ventricule droit obtenus à partir d’échocardiographies. Nous évaluons la stabilité des algorithmes en calculant leur erreur numérique et d’autres propriétés d’espaces symétriques. Nous avons également évalué la méthode au niveau du transport de la fonction cardiaque.

Conclusion

Ces travaux mènent à la mise en œuvre potentielle de nouveaux outils de segmentation de l’oreillette gauche et de sa paroi dans un pipeline de gestion clinique de la FA. La méthodologie employée peut aussi s’adapter à la segmentation d’autres organes, tels que les ventricules. Nous avons également proposé des schémas génériques pour

effectuer une modélisation statistique de la forme de l'oreillette et de la déformation temporelle du cœur.

Enfin cette étude pourrait conduire à une analyse de la signification physiologique des caractéristiques trouvées dans les études rétrospectives concernant les facteurs de risques sous-jacente à la FA au-delà de l'imagerie préopératoire.

Les projets ANR MIGAT et ERA CoSysMedSysAFib sont en partie financés par l'Agence Nationale de la Recherche (ANR). Ce travail se poursuivra en collaboration avec l'hôpital de Bordeaux, l'hôpital de Nice et les autres membres du projet SysAFib.

Abstract

Atrial fibrillation (AF) is the most common cardiac arrhythmia, characterized by chaotic electrical activation and unsynchronized contraction of the atria. This epidemic and its life-threatening complications and fast progression call for diagnosis and effective treatment as early as possible. Catheter ablation, an invasive procedure that establishes lesions to block the trigger points of AF and creates a barrier to the propagation of the arrhythmia, is an effective treatment for patients refractory to anti-arrhythmic drugs. However, the success rate of the first-time ablation may range from 30% to 75%, such that multiple ablation procedures may be recommended, and atrial mechanical function may be adversely affected.

With evolving imaging and digital technologies, the objective of the study is to understand the underlying physiology of AF better and to provide tools to assist clinical decision-making. We analyze the correlations between recurrent arrhythmia and patient characteristics before ablation, including the left atrial shape extracted from computed tomography images. Non-invasive extraction of the anatomical structures of the heart is a crucial prerequisite. We first developed semi-automatic methods to segment the left atrium and the left atrial wall from images. Next, we achieved good segmentation results with a neural network model. Then, we studied markers of shape related to both global and local remodeling, and the quantification of adipose tissue, deploying diffeomorphometry and statistical analysis tools. Finally, we extended the work to the statistical analysis of temporal deformation. We proposed a symmetric reformulation of the pole ladder, which improves the numerical consistency and stability.

Keywords: cardiac image analysis, atrial fibrillation, segmentation, fat, statistical shape analysis, parallel transport.

Acknowledgments

I would like to thank my supervisors, Maxime Sermesant and Xavier Pennec warmly. Thank you for your guidance when I encountered difficulties and for motivating me with your pure intention in pursuing innovative researches. I remember that Maxime said during his habilitation defense that he appreciates working with many people smarter than himself. I shall tell the same thing - it has been a great opportunity for me to learn from both of you. Hervé Delingette, I am especially grateful for your enlightenment for me in the field of medical image analysis. Thank you, Nicholas Ayache, for the chance to work within this friendly, creative, and excellent team, which shares a passion for medical imaging and adventures. I would remember the encouragement that you, Isabelle, and Jean-Claude brought me during Auron. I would like to specially mention my professor of the option Geostatistics at Mines ParisTech, Hans Wackernagel. You are a great mentor and a very kind person. I appreciate you brought me to statistics and image processing, which turned into my research field.

My sincere thanks to all colleagues who have made the journey a pleasant experience. Special thanks to *tutor* Marc-Michel for your help and my office-mates Matthieu, Julian, Tania, Nicolas G.. Thanks to Nicolas D., Marco L., Hervé L. for your generous guidance. Thanks to Loïc C., Nicolas S., Thibaud, Côme for explaining to me and helping me with your experiences in programming. Thank you to Alan, Bishesh, Cici, Fanny, Manon, Mehdi, Nina, Pawel, Qiao, Raphaël, Roch, Rocio, Sergio, Sofia, Sophie, Thomas and Wen for the cheerful time that we share. Thank you and best wishes to Antoine, Benoit, Buntheng, Clement, Florent, Gaëton, Jaume, Luigi, Nicolas C., Paul, Santiago, Sara, Yann, Yingyu and Zihao. Thank you, Isabelle, for supporting all of us.

Many thanks to our collaborators: Hubert Cochet, Hubert Nivet, Claudia Camaioni from CHU Bordeaux, Pamela Mocerri from CHU Nice, Nicolas Duchateau from Creatis Lyon, and the collaborators of SysAFib project, for all the enlightened moments and exchange. The research was partially funded by the Agence Nationale de la Recherche via ERA CoSysMed SysAFib / ANR MIGAT project. Thank you for your support!

Last, I would like to thank my family. You always support me in making my own decisions, and inspire me with your actions of continuous learning and exploring. I hope we will always grow together and encourage each other. 谢谢你们。

Contents

Résumé	iii
Résumé étendu en français	v
Abstract	ix
Acknowledgments	xi
Contents	xvi
List of Figures	xx
List of Tables	xxi
1 Introduction	1
1.1 Context	1
1.2 The ERA CoSysMed SysAFib Project	3
1.3 Objectives and Main steps	5
1.4 Technical Background	6
1.4.1 Atrial Segmentation	6
1.4.2 Myocardium Segmentation and Tissue Analysis	6
1.4.3 Statistical Shape Analysis	7
1.4.4 Parallel Transport	7
1.5 Structure of the Thesis and Contributions	8
1.5.1 Publications	9
1.5.2 Challenges	10
1.5.3 Honors	12
2 Atrial Segmentation	13
2.1 Background	14
2.1.1 Image Segmentation	14
2.1.2 Heart Structure	15
2.1.3 Imaging Modalities	16

2.1.4	Previous Work	16
2.2	Semi-Automatic Segmentation Method	17
2.2.1	Region Growing	19
2.2.2	Post-Processing	20
2.2.3	Testing on Public Database	20
2.2.4	Performance and Image Quality	20
2.3	From Semi-Automatic to Fully-Automatic	21
2.3.1	U-Net	21
2.3.2	Dual 3D U-Nets - Cropping and Segmenting	21
2.3.3	Loss Functions	23
2.3.4	Model Training and Predicting	24
2.3.5	3D GE-MRIs Atrial Segmentation Challenge Database	25
2.4	Discussions	28
2.4.1	Main Contributions	29
2.4.2	Future Work	30
3	Myocardial Tissue Analysis	31
3.1	Background	32
3.2	Methodology	35
3.2.1	Conventional Estimation	35
3.2.2	Towards Precise Wall Segmentation	37
3.3	Evaluation on Public Database	38
3.3.1	Dataset	38
3.3.2	Parameters	38
3.3.3	Wall Segmentation	38
3.3.4	Thickness Measurement	39
3.3.5	Participation in Benchmark Study	39
3.4	Training U-Net with Preliminary Results	41
3.4.1	Materials	41
3.4.2	Results	42
3.4.3	Explaining the Model	42
3.5	Discussions	42
3.5.1	Future Work	44
4	Shape Analysis	47
4.1	Background	49
4.1.1	Shape	50
4.1.2	Deformation	50
4.1.3	Statistical Learning	50
4.2	Methodology	51
4.2.1	Mesh Generation	51
4.2.2	Extraction of Remodeling Information	53
4.2.3	Quantification of Shape Variations	54
4.2.4	Extraction of Remodeling Information	58
4.2.5	Statistical Modeling	58

4.3	Materials	60
4.3.1	Data Preparation	60
4.3.2	Catheter Ablation	61
4.4	Preliminary Experiments in Paroxysmal Atrial Fibrillation	62
4.4.1	Population	62
4.4.2	Atlas of the Left Atrium	62
4.4.3	Diffeomorphic Registration	62
4.4.4	Remodeling	63
4.4.5	Principal Component Analysis	64
4.4.6	Partial Least Squares Analysis	65
4.4.7	Principal Modes Related to Post-Ablation Recurrence	66
4.4.8	Predictive Capabilities	66
4.5	Application on an Extended Database	69
4.5.1	Population	69
4.5.2	Benchmarking Left Atrial Descriptors	70
4.5.3	Inference Statistics and Multivariate Models	70
4.5.4	Results	70
4.5.5	Heterogeneous Regional Remodeling	71
4.6	Region Segmentation of Left Atrial Meshes	72
4.7	Discussions	73
4.7.1	Main Contributions	73
4.7.2	Limitations and Future Work	75
5	Deformation Analysis	77
5.1	Background	78
5.2	Methodology	80
5.2.1	Pole Ladder	80
5.2.2	Numerical Accuracy	80
5.2.3	LDDMM-Based Transport	82
5.2.4	SVF-Based Transport	83
5.2.5	Benchmark Transport Algorithm	83
5.3	Experiments	84
5.3.1	Materials	84
5.3.2	Template Estimation and Registration	84
5.3.3	Consistency	85
5.3.4	Strain Analysis	85
5.3.5	Statistical Modeling of Cardiac Deformation	88
5.4	Algorithmic Improvement for Riemannian Geodesics	90
5.4.1	Decomposition with Deformation and Residual	90
5.4.2	Formulations Accounting for Residuals	90
5.4.3	Affine Symmetric Space	92
5.4.4	Types of Errors	92
5.4.5	Decomposition Continuum	93
5.4.6	Results	95

5.5	Discussions	95
5.5.1	Limitations	95
5.5.2	Main Contributions	97
5.5.3	Future Work	98
6	Conclusion and Perspectives	99
6.1	Main Contributions	99
6.1.1	Imaging - Robust Image Segmentation	99
6.1.2	Computational Anatomy - Shape and Deformation	100
6.1.3	Clinical Implications	101
6.2	Future Work	101
6.2.1	Short Term	101
6.2.2	Long Term	102
	Appendices	105
A	Data Science Tools	105
A.1	Principal Component Analysis	105
A.2	Partial Least Squares Regression	106
B	Coding Platforms	106
B.1	DTK Visual Programming	106
C	Parameter-Setting for JFR 2018 Renal Cortex Segmentation	107
	Reference	119

List of Figures

1.1	Electrical activity of a normal heart (left) and a heart with atrial fibrillation (right) [<i>Atrial Fibrillation Fact Sheet</i> , 2016].	2
1.2	Core concepts of the SysAFib project: four-tiered system medicine. . .	4
1.3	2D renal cortex segmentation from CT images. Illustration of CT image and ground truth segmentation (left). Ensemble prediction with multiple pre-trained U-Nets (right), displaying high inter-model variability in forecasting, which works well with a majority voting strategy. We won second place at JFR 2018 Data Challenge.	11
2.1	(a) Base and diaphragmatic surface of heart, from the 1918 edition of <i>Anatomy of the Human Body</i> , by Henry Gray (1821–1865) [<i>Gray</i> , 1878]. ; (b) Heart Flow [<i>Wapcaplet</i> , 2006].	15
2.2	The flowchart of semi-automatic left atrial endocardial segmentation - pre-processing and region growing.	18
2.3	Interactive isolation of the left atrium. (a), (b) show polygons (green) drawn manually and used for interpolation; (c),(d) show automatically interpolated polygons (violet) on the rest slices, (d) shows the manual correction tool (orange circle).	19
2.4	Proposed dual 3D U-Net structure. Green blocks represent 3D features; Dark blue refers to interface operation to crop the region of interest based on first U-Net prediction.	22
2.5	The framework of successive U-Nets training I: the first U-Net - low resolution cropping. We show here axial slices of MR images, overlapped with manual segmentation of the left atrium in blue, our segmentation in red, the intersection of the two in purple.	22
2.6	The framework of successive U-Nets training II: the second U-Net - segmenting, with ensemble prediction models.	23
2.7	Visualization of a good and a bad scenario of validation datasets segmentations, with their Dice, Hausdorff distance (HD) compared with the ground truth. (a) manually segmented; (b) predicted with Dice coefficient loss; (c) predicted with Contour loss.	28

3.1	Anatomy of the heart wall [<i>OpenStax College, 2013</i>].	33
3.2	Example axial slice of cardiac CT images containing the left atrium. . .	34
3.3	Conventional method for epicardial fat analysis.	36
3.4	Axial slices of CT images, overlapped with manual segmentation of the left atrial wall in green, our segmentation in red, intersection of the two in yellow. (a) Dataset #2; (b) dataset #3; (c) dataset #5; (d) example slice zoomed in.	39
3.5	(a) Mean and interquartile range of the left atrial wall thickness for 10 datasets tested, with maximum whisker length specified as 1.5 times the interquartile range; (b) left atrial wall thickness map for dataset #8, posterior view; (c) left atrial wall thickness map for dataset #8, anterior view.	40
3.6	Correlation between algorithms and ground truth in the left atrial wall thickness measurement. Illustrated with cases of excellent image quality (left), good (middle), and poor (right) [<i>Karim et al., 2018</i>].	41
3.7	Performance of compensation Net on training and validation datasets. .	42
3.8	Performance of compensation Net on testing datasets.	43
3.9	Feature maps of the two U-Nets. (a) the model to perform the left atrial endocardium segmentation from previous chapter; (b) the model to perform the left atrial segmentation with a few training datasets. The U-Net for the left atrial wall segmentation also generates features related to the atrial shape, but its feature maps look noisier.	43
3.10	Demonstrating the relation between fat quantification and clinical factors, using U-Net with MC-GAC prediction (left) and Conventional Estimation (right).	45
4.1	Mesh generation: from binary mask to triangle-composed surface. (a) Example axial slice of binary mask; (b) mesh generated, here we refer to a triangle-composed surface.	52
4.2	Comparison of the two methods VTK and CGAL in mesh generation. (a) VTK mesh; (b) CGAL mesh. CGAL shows significant improvement in mesh regularity while VTK describes details of the left atrial appendage better.	53
4.3	The Dirac currents of a triangulated mesh are positioned at the barycenter of every triangle and oriented along their normal. These momenta that parameterize the diffeomorphic deformation are defined at the barycenter. They are not necessarily normal to surface [<i>Mansi et al., 2011</i>]. . .	56
4.4	(a) A dozen of left atrial meshes from the population under study, as an illustration of the great difference of the left atrial shape that we can find among people; (b) atlas of the left atrium, which reflects an anatomic average within a dataset.	62
4.5	Comparison of a registration result and its target subject using LDDMM. Registration result in blue, target subject in gray.	63

4.6	Extraction of remodeling information vs. controls. (a) reference for atrial remodeling offered by control subjects; (b) the template in blue, before and after warping in a registration process toward the target in orange.	64
4.7	Atlas with $+\sigma$ deformation results on the direction of the first 5 modes. (a) Atlas; (b) Atlas in gray with the 1 st mode of deformation in blue; (c) Atlas in gray with the 2 nd mode of deformation in blue; (d) Atlas in gray with the 3 rd mode of deformation in blue; (e) Atlas in gray with the 4 th mode of deformation in blue; (f) Atlas in gray with the 5 th mode of deformation in blue.	65
4.8	The first three modes of deformation involved in post-ablation recurrence. σ represents the standard derivation of each mode in the population. (top) the principal modes of deformation from less recurrence to more recurrence, where the color of meshes represents area strain. (bottom) the shape at σ on each principal axis, where the color illustrates area strain and displacement.	67
4.9	Receiver operating characteristic curves of 6-month post-ablation recurrence prediction.	68
4.10	Bayesian Model of Catheter Ablation Response.	71
4.11	Critical regions implicated in catheter ablation failure.	72
4.12	Efficient left atrial region labeling I: automatically transferring region labels on the template to another mesh through diffeomorphic registration. PVs (common left trunk, yellow and right PVs, light blue), appendage (orange), and body (dark blue). The red triangular cells are at the center of the anterior wall and posterior wall, used to compute the anteroposterior diameter of the left atrium.	74
4.13	Efficient left atrial region labeling II: more detailed anatomic divisions of the left atrium (top), according to a 22-segment model of the left atrium (bottom) [<i>Hunter et al.</i> , 2011, 2012].	74
5.1	Illustration of parallel transport of vectors a and b along a curve (left) and the application of parallel transport in cardiac motion analysis focusing on surface meshes (right).	80
5.2	The proposed symmetry-based reformulation of the pole ladder structure.	82
5.3	Artifacts (left) to avoid in registration due to inappropriate kernel size and shape representation, compared with (right) a registration with chosen parameters.	83
5.4	Illustration of stationary velocity field computation for surface matching.	84

5.5	Comparison of different algorithms for the preservation of area strain across clinical subgroups during transport. (1) H represents the healthy subgroup, II, III, IV represent NYHA classes for pulmonary hypertension. (2) Global area strain of the right ventricle, as well as the area strain of the lateral wall and the inferior wall. (3) "Original" means the original subject's ED-ES deformation, while for parallel transport algorithms, the warped template's ED-ES deformation after transport. Mismatch of the trend of area strain in disease progression for conjugate action for SVF, on the inferior wall.	87
5.6	Comparison of point-to-point displacement (top) and the pole ladder with SVF (bottom) in the compact representation of end-diastole-end-systole (ED-ES) deformation. First two modes of variation are very different after applying PCA on the transported ED-ES changes. Surface folds appear at 3σ for point-to-point displacement (arrow).	89
5.7	Midpoint with residuals	91
5.8	Symmetry with residuals	92
5.9	Type of error I: Centrality	93
5.10	Type of error II: Involutivity	94
5.11	Type of error III: Transvectivity	94
5.12	The four errors for different values of regularization α^2 , with and without residuals in the computation of the midpoint and the symmetries. . . .	96
6.1	The interface of MUSIC software.	108
6.2	The implementation of the left atrial wall segmentation pipeline with DTK Visual Programming platform.	108

List of Tables

2.1	Comparison of the loss functions: Dice coefficient loss (top) and Contour loss (bottom), with various evaluation metrics computed on validation datasets segmentation for each U-Net model. The darker the gray color, the better the performance.	27
2.2	The number of connected components found in predicted segmentation, the smaller, the more regular.	27
3.1	Intensity value thresholds used for 10 datasets tested.	38
4.1	Variations explained by the first 10 PCA modes of deformation.	64
4.2	Percentage of variance explained in the first partial least squares regression, for shape and left atrial volume index (LAVI) respectively.	65
4.3	Percentage of variance explained in the second partial least squares regression, for shape and post-ablation recurrence respectively.	66
4.4	Student's t-test to compare shape score and left atrial volume index (LAVI) in two sub-groups and area under receiver operating characteristic curves (AUC).	68
5.1	Numerical consistency of parallel transports. Fiducial localization error (FLE) due to shape registration (left) and to forward/backward transport (right) ($\mu \pm \sigma$ in <i>mm</i>).	85
5.2	Compactness of the representations	88

"The heart of animals is the foundation of their life, the sovereign of everything within them, the sun of their microcosm, that upon which all growth depends, from which all power proceeds."

— William Harvey

CHAPTER 1

Introduction

Contents

1.1	Context	1
1.2	The ERA CoSysMed SysAFib Project	3
1.3	Objectives and Main steps	5
1.4	Technical Background	6
1.4.1	Atrial Segmentation	6
1.4.2	Myocardium Segmentation and Tissue Analysis	6
1.4.3	Statistical Shape Analysis	7
1.4.4	Parallel Transport	7
1.5	Structure of the Thesis and Contributions	8
1.5.1	Publications	9
1.5.1.1	Peer-reviewed Journals	9
1.5.1.2	Peer-reviewed Conferences	10
1.5.1.3	Abstracts	10
1.5.2	Challenges	10
1.5.2.1	STACOM Challenges	10
1.5.2.2	JFR 2018 Data Challenge - Renal Cortex Segmentation	11
1.5.3	Honors	12

1.1 Context

Atrial fibrillation (AF) is the most frequently encountered arrhythmia in clinical practice, characterized by uncoordinated electrical activation and disorganized contraction of the atria (Fig. 1.1). Around 2% to 3% of the population in Europe and North America, as of 2014, were affected, and its prevalence rate is increasing worldwide, especially in the elderly population [Zoni-Berisso *et al.*, 2014; Morillo *et al.*, 2017]. This epidemic, with or without symptoms, is likely to be associated with life-threatening consequences, including heart failure and heart attack. It is a leading cause of stroke

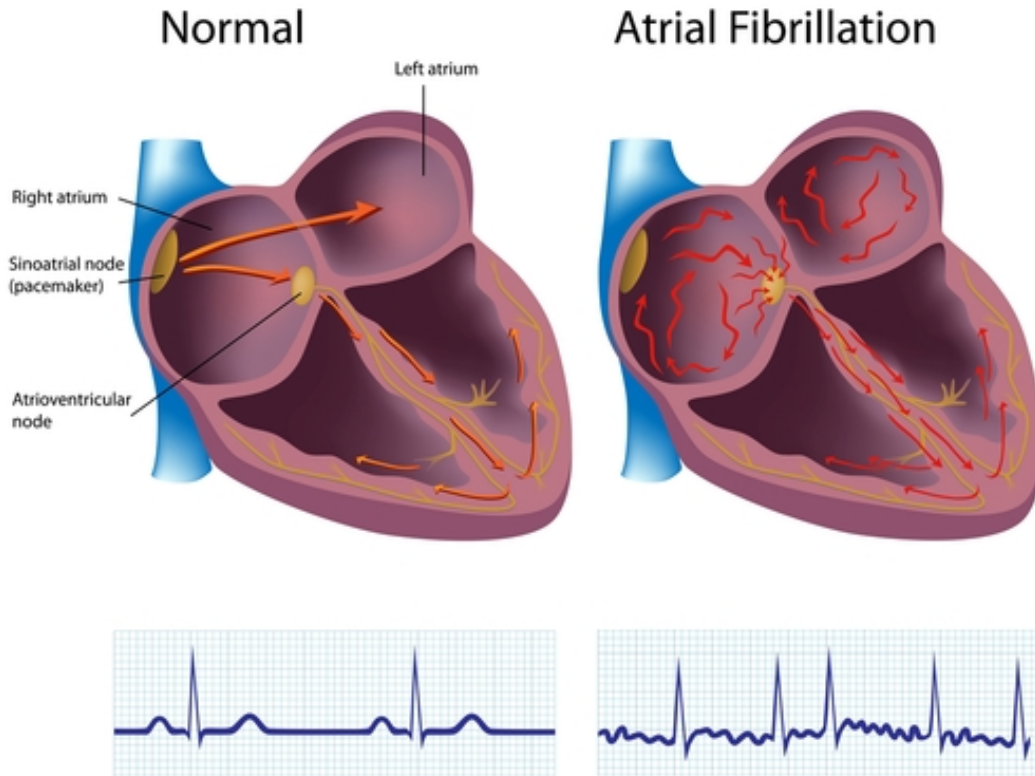


Figure 1.1: *Electrical activity of a normal heart (left) and a heart with atrial fibrillation (right) [Atrial Fibrillation Fact Sheet, 2016].*

[Benjamin *et al.*, 1998]. AF also leads to increased public resource utilization and expense on healthcare.

Catheter ablation is an effective AF treatment for drug-refractory patients. However, arrhythmia frequently recurs after ablation, which leads to multiple procedures to obtain long-term rhythm control. The efficacy of first-time ablations may range from 30% to 75% depending on the individual situation of patients, such that multiple ablation procedures may be recommended [Verma *et al.*, 2015; Balk *et al.*, 2010]. Restoration of sinus rhythm systematically fails to sustain after ablations in approximately 20% of patients. The underlying mechanisms are still insufficiently understood, except that AF persistence and left atrial structural remodeling may play a vital role [Kirchhof *et al.*, 2016]. To maximize positive treatment outcomes and ensure judicious resource allocation of healthcare systems, we need to recognize, for a particular patient with AF, whether an ablation procedure is likely to benefit the patient or the arrhythmia is likely to reoccur.

Currently, there is no decision support tool enabling clinicians to integrate patient data in a predictive model to facilitate the treatment planning of AF. Researchers are working towards a better understanding of the underlying physiology of AF and producing solutions to this matter.

With continuously developing imaging technologies, we can analyze non-invasively anatomical structures of the heart, which have been proven to be related to pathology development and treatment outcome in arrhythmia patients [Kirchhof *et al.*, 2016; Bisbal *et al.*, 2013, 2018]. Here I describe three essential foundations for this PhD thesis.

Firstly, computed tomography (CT) imaging has numerous clinical applications in cardiovascular imaging. Some hospital centers routinely perform imaging of the heart before atrial ablation therapy [Wolf *et al.*, 2010; Donal *et al.*, 2016] for the management of AF. The images provide accurate anatomical geometries for procedural registration in electro-anatomical mapping systems, which aides the ablation [Tops *et al.*, 2005]. More recently, the ability to rule out thrombus before ablation further justified the systematic use of CT [Romero *et al.*, 2013]. Therefore, large datasets are potentially readily available.

Secondly, the rapidly-developing automatic image processing techniques allow us to analyze these data and reveal important features from population-wise modeling. The techniques include and are not limited to: image segmentation, shape models, diffeomorphic deformation, statistical learning, neural network. The evolution of computer hardware also benefits the study by significantly reducing the processing time. This work was supported by the Inria Sophia Antipolis - Méditerranée, "NEF" computation cluster.

Thirdly, the intuitions of clinical experts and previous clinical research in the related field are essential for this study. We work in close collaboration with radiologists and cardiologists. The understanding of the structures of the heart, the physiology of AF, and the clinical protocol have inspired the study to look into left atrial anatomy, tissues, structure and deformation. Manual segmentation by experienced radiologists provided valuable information for the learning algorithms. Evaluation of the results by clinicians produces hypotheses of the underlying physiology and takes into account clinical implications.

1.2 The ERA CoSysMed SysAFib Project

This work is part of an international project, "SysAFib: systems medicine for diagnosis and stratification of atrial fibrillation" (Fig. 1.2), under ERA CoSysMed administration and partially funded by the Agence Nationale de Recherche, France.

The project combines diverse pre-ablation patient data and expertise, notably in the following four areas: **ECG analysis**, **statistical shape modeling**, **biophysical modeling and simulation**, and **genetic profiling**. The goal of the project is to analyze these patient historical data, convert them into an integrated prediction model to estimate a prior treatment outcome of atrial ablation, and constitute a new decision support system for AF patients.

The interdisciplinary venture is jointly carried out by partners from Simula Research Laboratory, Helmholtz Zentrum München, Oslo University Hospital, Maastricht University, Università della Svizzera Italiana and Inria. My work focuses on statistical shape modeling from pre-ablation CT images in the AF population.

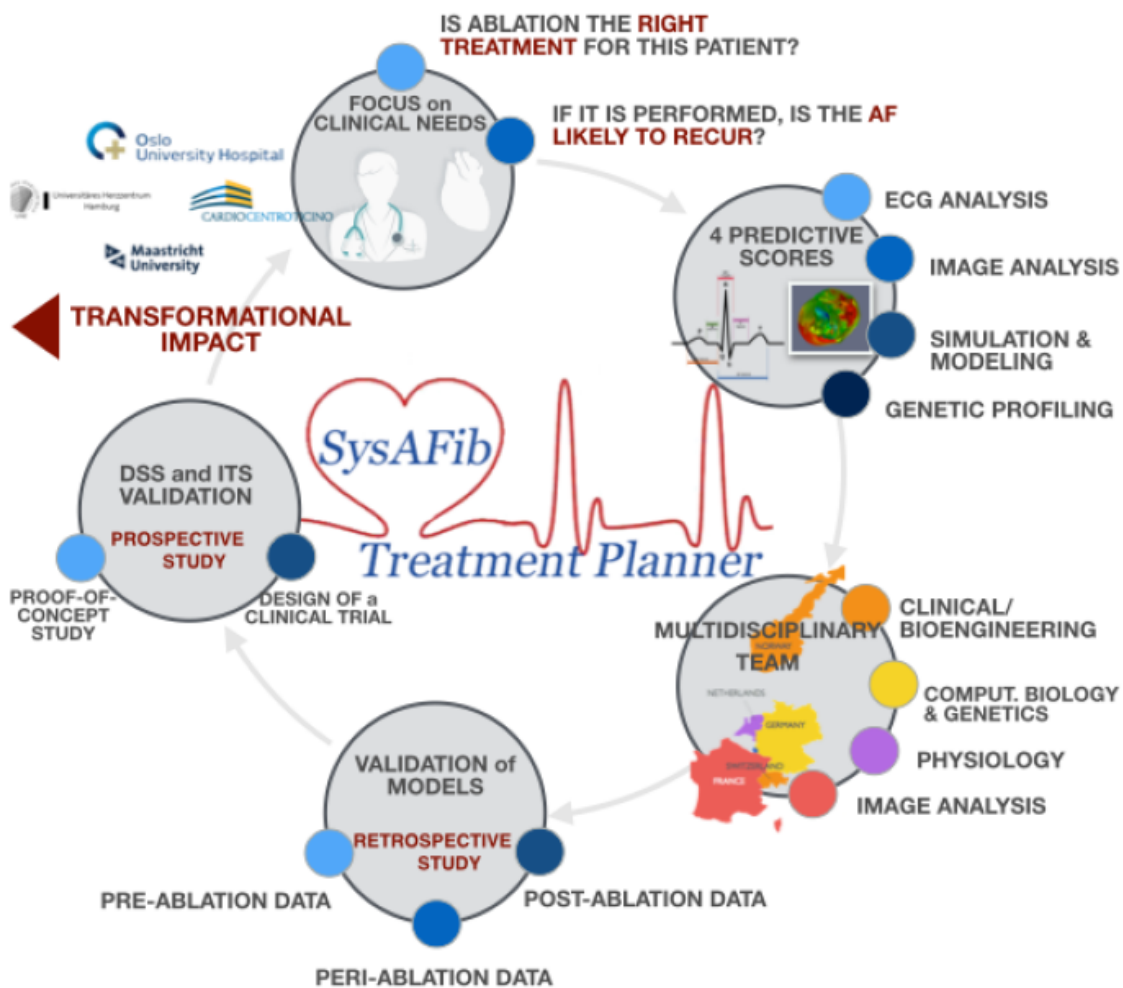


Figure 1.2: Core concepts of the SysAFib project: four-tiered system medicine.

1.3 Objectives and Main steps

The main objectives of my work are

- analyzing, in collaboration with clinicians, a large database of pre-ablation CT images with multiple clinical factors in the AF population.
- developing automatic methods for the task of segmenting the left atrium and the left atrial wall from cardiac CT and magnetic resonance imaging (MRI) images.
- integrating the existing important factors for the AF patients management, and discovering new shape-related features, predictive of arrhythmia recurrence.
- studying epicardial tissue inside the left atrial wall in the AF population.
- improving parallel transport algorithms to achieve robust and proper normalization of heart deformation, extending shape statistics to deformation statistics.
- working with partners within the SysAFib project to develop an integrated decision support system to improve the risk stratification in AF and testing it on an external cohort.

The first part of the work is to segment the left atrium and the left atrial wall from cardiac images automatically, in particular, from CTs. The inner layer of the heart chamber wall is called the endocardium, and the outer layer is called the epicardium. We tackle the segmentation of the endocardium by using the region growing algorithm in an interactive pipeline. To deal with the challenging task of segmenting the heterogeneous, thin left atrial wall (the epicardium), we propose a revised active contour approach, taking into consideration the neighboring environment next to the left atrium. Being aware of the various advantages of deep learning methods, we also investigate the use of convolutional neural network (CNN) to perform automatic segmentation. Then, measurements are done based on the segmentation and 3D anatomy models to collect information, such as the patient-specific left atrial shape variations and distribution of atrial wall thickness. The study is extended to analyze the adipose tissue inside the left atrial wall.

The second part is to analyze the shape and the deformation of the left atrium that we extract from CT images in the previous step, focusing on computational anatomy. We first generate 3D triangular meshes based on binary masks of the left atrial segmentation. Next, using tools such as currents representation of surfaces, large deformation diffeomorphic metric mapping (LDDMM), we quantify the shapes, and perform inter-subject shape registration and atlas computation. This step enables the estimation of the average left atrial anatomy (called template) in healthy and pathological groups, and the computation of patient-specific shape variations compared with the template. Then, we employ statistical tools, principal component analysis, and partial least squares regression in population-wise studies to classify disease status and pathological shape features. To model the heart contraction in the cardiac cycle and analyze it in a population-wise study, we need to perform normalization of these temporal

deformations because of subject-specific anatomical variability. We transport intra-subject deformations onto the same template/reference shape via parallel transport. We further look into parallel transport from the perspective of numerical consistency.

Finally, we raise some questions during the study about the underlying causality of AF and its associated consequences. Potential future work includes modeling whole cardiac sequences, developing parametric electrophysiology models (cardiac electrophysiology and interventions), and investigating the physiological meaning of the features found in the retrospective population-based studies.

1.4 Technical Background

1.4.1 Atrial Segmentation

Image segmentation is the procedure to divide an image into multiple regions, with pixels assigned to the same region sharing specific characteristics. The applications in medical imaging often concern the isolation of an organ, a tumor, or other meaningful representations from images of the interior of the human body. The accuracy of image segmentation has been continuously evolving, thanks to both more powerful imaging capability and computational innovations. We can partition segmentation methods in cardiac imaging into two categories: segmentation with weak or no prior, segmentation with a model prior. Methods without prior include thresholding, mathematical morphology, active contour. Priors can be an atlas, a statistical shape model, or deformation constraints.

For the specific task of the left atrial segmentation, previous studies [Tobon-Gomez *et al.*, 2013; Kutra *et al.*, 2012] used shape-constrained deformable models, auto-selection from multi-atlas models. Recently, the development in hardware, with Graphics Processing Unit, enables the implementation of deeper (larger) neural network models and reduces time to train a model. This evolvment allows testing more parameters, network settings, and structures in a given period. CNN, a type of deep feedforward network, has been widely applied in image-related tasks and shows clear advantages of high-efficiency [Cecco *et al.*, 2017]. Based on CNN, [Ronneberger *et al.*, 2015] proposed the original U-Net structure, which was later extended to 3D. Its structure with drop out and skip connection mitigates overfitting and improves performance. Previous studies reported numerous applications of CNN for the task of cardiac image segmentation [Oktay *et al.*, 2017; Zheng *et al.*, 2018], and more fields in medical imaging [Litjens *et al.*, 2017; Liu *et al.*, 2018]. Despite high efficiency, the risk in robustness and explainability has limited the usage of neural network models in clinical practice.

1.4.2 Myocardium Segmentation and Tissue Analysis

Most previous works to estimate the left atrial wall thickness rely on ruler-based measurements performed on 2D slices, without performing a prior segmentation of the wall, as summarized in [Karim *et al.*, 2018]. Besides, [Dewland *et al.*, 2013] chose to perform

a segmentation of the wall in four regions, inter-atrial septum, below right inferior pulmonary vein, appendage, and anterior wall. Whereas [Inoue *et al.*, 2015, 2014] built a multi-region segmentation pipeline based on a hierarchical constraint structure.

The segmentation of the left atrial wall is a very challenging task. The wall, only several pixels wide in images, is heterogeneous, consisting of mostly muscles but possibly fat granules and fibrosis. Also, the left atrial wall is attached to structures sharing similar intensity values in images, such as the wall of the aorta. The accuracy of the segmentation is also difficult to validate, as few manual segmentation or reliable ground truths are available.

We adapt the geodesic active contour model [Caselles *et al.*, 1997] to segment the left atrial wall. Then, with preliminary predictions, we train a U-Net to process images in an extensive database efficiently. To the best of our knowledge, no previous methods have been proposed to quantify epicardial fat volume from images automatically. Using the wall segmentation, we determine fat inside the wall using the relative linear attenuation values from CT images.

1.4.3 Statistical Shape Analysis

Computational anatomy provides tools for statistical analysis of shapes in a population: quantifying shape differences, estimating average normal and pathological anatomies, detecting and classifying disease status, and predicting the shape evolution due to progression. The reason to study anatomies is that shape variations may be related to remodeling of certain biological phenomena that we are interested in investigating, which may be not directly accessible.

Previous studies [Bisbal *et al.*, 2013; Varela *et al.*, 2017] proposed predictors of recurrent arrhythmia, which are single size-related measurements of the left atrial from images. They assessed how closely the shape of the left atrium resembles that of a perfect sphere, and how asymmetric the shape is. More generally, we can use points, curves, or surfaces, a collection of manifolds, to represent deformable shapes. The metric study of shapes can potentially capture more detailed shape characteristics. There are various ways to define metrics in the shape space, measuring the distance between each pair of shapes [Charon and Trounev, 2013; Durrleman *et al.*, 2014]. In particular, diffeomorphisms deform shapes through the orbit, resulting in invertible and folding-free deformations. The metric between two diffeomorphisms is defined as the shortest length or geodesic flow in the orbit of shapes.

The central concept with computational anatomy is to extract representative shape characteristics, from a generic atlas, group-wise patterns, to patient-specific models. Their predictive value for prognostic assessment and individual risk stratification was appraised in statistical learning studies [Mansi *et al.*, 2011; McLeod *et al.*, 2015].

1.4.4 Parallel Transport

To model temporal/longitudinal evolution or cross-sectional variations of anatomical shapes, we have to take into consideration the intrinsic differences in shapes and how

to normalize these deformations before statistical analysis. Previous works proposed conjugate action and computed local reorientation of myocardial velocities [Duchateau *et al.*, 2011; Bai *et al.*, 2015]. The vectors of myocardial velocities parametrize the cardiac deformations, and therefore, conveying them on the same coordinates realizes required normalization.

The notion of parallel transport in differential geometry refers to an infinitesimal transformation along smooth curves in a manifold. Previous works [Younes, 2007; Qiu *et al.*, 2008] introduced parallel transport to medical image analysis. We base our work on a later proposed discrete numerical scheme, the pole ladder [Lorenzi and Pennec, 2014], because of the property that the pole ladder realizes the exact parallel transport in symmetric spaces in one step [Pennec, 2018]. So far, these methods have been applied only to neuroimaging. Another work based on the fanning scheme was proposed in [Louis *et al.*, 2017].

In practice, the intersubject and intrasubject registrations are not perfectly smooth and accurate. There always exists a compromise between parsimony and precision. Inexact shape matching results in amplified errors in parallel transport. Another issue is that flows of velocity vectors endowed with right-invariant metric (LDDMM), is not symmetric by nature. The additional error terms affect the accuracy of the pole ladder. To improve the numeric implementation, we convert the pole ladder to a structure closer to being symmetric in various diffeomorphic settings.

1.5 Structure of the Thesis and Contributions

I present this thesis following the order of the different tasks needed to pursue this analysis, and highlight the main contributions in this section.

Chapter 2 aims at developing efficient methods for the task of left atrial segmentation. The step is the foundation to analyze non-invasively the anatomical structures of the heart and can provide ablation guidance.

- We developed an interactive region growing pipeline, and an efficient deep 3D convolution neural network based on U-Net, to segment the left atrium from CT images.
- We introduced a Contour loss based on additional distance maps to adjust the final segmentation, with which the prediction showed smaller Hausdorff distance and less granular errors.

Chapter 3 extends the segmentation to the dual layers of the left atrial wall, and analyzes the tissues inside.

- We solved the challenging task of segmenting the intermediate layer of the myocardium from cardiac CT images, which consists of only few pixels and is of low contrast.

- For this purpose, we adapted and revised the geodesic active contour model to include external excluding neighboring information, combining intensity-based and shape-based methodology.
- We analyzed the epicardial adipose tissue in the wall, which led to a better classification of AF severity.

Chapter 4 describes the population-wise analysis of the left atrial shapes, including both global features and local surface area change.

- We extracted features of the left atrial shape related to arrhythmia recurrence in AF, providing incremental predictive value beyond conventional indicators.
- We identified critical regions whose local remodeling was associated with arrhythmia recurrence.
- The adverse structural findings, both global and regional, could lead to potential ablation targets outside pulmonary veins for treatment planning.

Chapter 5 highlights the methodology development for parallel transport, a prerequisite to statistical analysis of the deformations.

- We extended the pole ladder to a mid-point and symmetry reformulation, which improved the numerical consistency and stability.
- We proposed a continuum of decompositions of the space of diffeomorphisms, approximated better a symmetric space by taking into account the residuals in registrations.

Chapter 6 summarizes the main contributions of the thesis and discusses potential future work and perspectives, especially cardiac motion analysis, atrial electrophysiology, and flow simulations.

1.5.1 Publications

The thesis leads to the following publications till Oct 2019.

1.5.1.1 Peer-reviewed Journals

- Jia S, Nivet H, Pennec X, Camaioni C, Jaïs P, Cochet H, Sermesant M. Arrhythmia Recurrence after Catheter Ablation in Atrial Fibrillation: a CT-Based Statistical Study of the Left Atrial Shape. Manuscript submitted.
- Karim R, Blake LE, Inoue J, Tao Q, Jia S, Housden RJ, Bhagirath P, Duval JL, Varela M, Behar J, Cadour L. Algorithms for left atrial wall segmentation and thickness–Evaluation on an open-source CT and MRI image database. *Medical image analysis*. 2018;50:36-53.

1.5.1.2 Peer-reviewed Conferences

- Guigui N, Jia S, Sermesant M, Pennec X. Symmetric Algorithmic Components for Shape Analysis with Diffeomorphisms. In Geometric Science of Information 2019.
- Jia S, Duchateau N, Mocerri P, Sermesant M, Pennec X. Parallel transport of surface deformations from pole ladder to symmetrical extension. In International Workshop on Shape in Medical Imaging 2018;116-124. Held in conjunction with MICCAI. (Oral)
- Jia S, Despinasse A, Wang Z, Delingette H, Pennec X, Jaïs P, Cochet H, Sermesant M. Automatically segmenting the left atrium from cardiac images using successive 3D U-nets and a contour loss. In International Workshop on Statistical Atlases and Computational Models of the Heart 2018;221-229. Held in conjunction with MICCAI. (Oral)
- Jia S, Camaioni C, Rohé MM, Jaïs P, Pennec X, Cochet H, Sermesant M. Prediction of Post-Ablation Outcome in Atrial Fibrillation Using Shape Parameterization and Partial Least Squares Regression. In International Conference on Functional Imaging and Modeling of the Heart 2017;311-321.
- Jia S, Cadour L, Cochet H, Sermesant M. STACOM-SLAWT challenge: left atrial wall segmentation and thickness measurement using region growing and marker-controlled geodesic active contour. In International Workshop on Statistical Atlases and Computational Models of the Heart 2016;211-219. Held in conjunction with MICCAI. (Oral)

1.5.1.3 Abstracts

- Cedilnik N, Jia S, Jaïs P, Cochet H, Sermesant M. Automatic non-invasive substrate analysis from CT images in post-infarction VT. European Heart Rhythm Association (EHRA) 2019.

1.5.2 Challenges

Participation in challenges and benchmark studies has been an exciting part of my PhD project. I think this benefits me in several ways: understanding different ways to solve the same problems, knowing where and why some methods achieve excellent performance, what is the state-of-art. Thanks to all organizers.

1.5.2.1 STACOM Challenges

We participated in two challenges as a part of the International Workshop on Statistical Modelling and Computational Modeling of the Heart (STACOM), held in conjunction with the International Conference On Medical Image Computing and Computer Assisted Intervention (MICCAI).

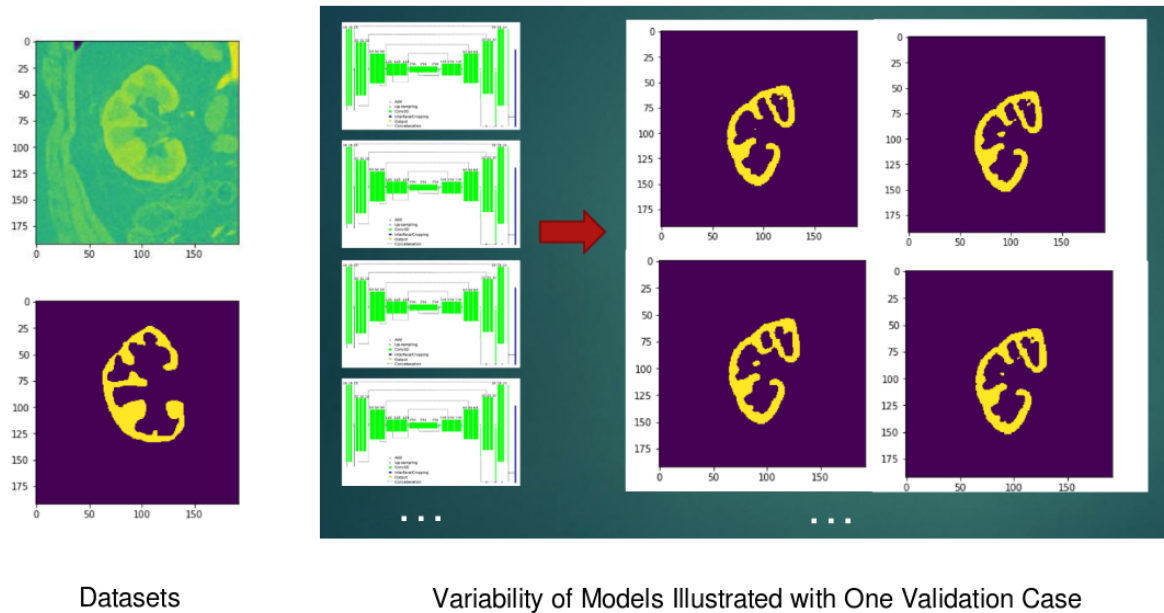


Figure 1.3: *2D renal cortex segmentation from CT images. Illustration of CT image and ground truth segmentation (left). Ensemble prediction with multiple pre-trained U-Nets (right), displaying high inter-model variability in forecasting, which works well with a majority voting strategy. We won second place at JFR 2018 Data Challenge.*

- STACOM Left Atrial Wall Thickness Challenge, which focused on algorithms for left atrial segmentation and wall thickness measurement from 3D MRI and CT images. 2016
- STACOM Atrial Segmentation Challenge, which required producing a fully automatic computational framework to segment the left atrial cavity from 3D MRI images without manual assistance. 2018

The work leads to the development of a fully automatic segmentation package for the left atrium from CT images, with potential clinical applications.

1.5.2.2 JFR¹ 2018 Data Challenge - Renal Cortex Segmentation

The database consists of 498 2D renal cortex CT images and their segmentation (.nii.gz) (Fig. 1.3), in addition to 299 testing sets to exam the performance of the model. We use 498 datasets in the training phase, split them into training and validation to control early stop to avoid over-fitting.

We used an ensemble technique of combining several 2D U-Net models to achieve a stronger model together. To do so, we trained several U-Nets with different parameter settings. More details of parameter-setting can be found in Appx. C.

¹Journées Francophones de Radiologie

Additionally, we analogized the **bootstrapping** procedure, which initially refers to random sampling with replacement to get an estimate of the variability of the data. Similarly, in cross-validation, we trained a pair of U-Nets with the same parameters, but with randomly split training-validation samples for each, to mitigate the bias introduced by choosing a particular training dataset.

Data Observation Among the 498 training datasets, 13 cases have potentially misleading ground truth segmentation, where we see a second renal cortex in the CT image while only one was segmented manually. We chose to exclude these cases in the learning procedure for half of the U-Nets.

Overall prediction In total, we trained 12 U-Net models with the approach mentioned above. The final segmentation prediction is based on the average of the 12 probability maps generated by the U-Nets at a pixel level. We call this a majority voting system with degrees of confidence, with each U-Net evaluating on each pixel how likely it belongs to the renal cortex.

Materials We used computing cluster with GPU capacity 6.1, 16G for training, personal computer with Intel Core i7 processor for predicting.

Results Final validation loss (Dice) for individual U-Net varied in the range from 0.85-0.87. The testing results was 0.864. We ranked second in the final competition.

Discussions Multiple hospital centers provided the CT images and segmentation ground truths. The segmentation of different experts cannot be precisely identical. They may use various imaging equipment. Furthermore, CT Images can present with varying levels of intensity due to the decay of contrast between the peak after injection and the time of imaging. Learning a segmentation model separately for each hospital may offer better solutions to cope with such variability.

1.5.3 Honors

I was honored to receive a Best Paper Award at STACOM workshop in October 2016, and the second prize of Prix Pierre Laffitte (pioneer of Sophia Antipolis Technology Park) in October 2018, which rewards high-quality, innovative PhD work, closely linked with industry or the common good.

"Time, which changes people, does not alter the image we have of them."

— Marcel Proust

CHAPTER 2

Atrial Segmentation

Analyzing the structure of the left atrium can provide precious insights into the pathology of atrial fibrillation, eventually resulting in the optimization of treatment plans. We present an interactive, patient-specific method to segment the left atrial endocardium¹ from cardiac computed tomography (CT) images, and then a neural network model trained on 500+ samples with expert segmentation (using the interactive method).

Automatic segmentation without manual manipulation of the left atrium is a non-trivial task. Clinicians first define boundaries of the region of interest on the images via computer-assisted polygon drawing. Then, we adapted the region growing algorithm to segment the left atrial endocardium as a growing connected volume. To achieve fully-automated segmentation, we finally propose an efficient deep 3D convolutional neural network based on U-Net, to localize and then segment the left atrium from CT images.

A Contour loss based on additional distance maps is devised to adjust the final segmentation, with which the prediction showed smaller Hausdorff distance and less granular errors.

We improved the robustness using an ensemble technique of combining several U-Nets into a stronger model, deploying the concept of bootstrapping, and majority voting.

Aimed at facilitating the segmentation of the left atrial structures, these methods are partially implemented in the MUSIC software for clinical use.

Part of this chapter corresponds to the following scientific articles:

1. Jia S, Cadour L, Cochet H, Sermesant M. STACOM-SLAWT challenge: left atrial wall segmentation and thickness measurement using region growing and marker-controlled geodesic active contour. In International Workshop on Statistical Atlases and Computational Models of the Heart 2016;211-219 [*Jia et al.*, 2017a].

¹We refer to the segmentation of the region inside the left atrial endocardium as the segmentation of the left atrial endocardium.

2. Jia S, Despinasse A, Wang Z, Delingette H, Pennec X, Jais P, Cochet H, Serresant M. Automatically segmenting the left atrium from cardiac images using successive 3D U-nets and a contour loss. In International Workshop on Statistical Atlases and Computational Models of the Heart 2018;221-229 [*Jia et al.*, 2018a].

Contents

2.1	Background	14
2.1.1	Image Segmentation	14
2.1.2	Heart Structure	15
2.1.3	Imaging Modalities	16
2.1.4	Previous Work	16
2.2	Semi-Automatic Segmentation Method	17
2.2.1	Region Growing	19
2.2.2	Post-Processing	20
2.2.3	Testing on Public Database	20
2.2.4	Performance and Image Quality	20
2.3	From Semi-Automatic to Fully-Automatic	21
2.3.1	U-Net	21
2.3.2	Dual 3D U-Nets - Cropping and Segmenting	21
2.3.3	Loss Functions	23
2.3.4	Model Training and Predicting	24
	2.3.4.1 Fixed Experimental Setting	25
	2.3.4.2 Varying Experimental Setting	25
	2.3.4.3 Overall Prediction	25
2.3.5	3D GE-MRIs Atrial Segmentation Challenge Database	25
	2.3.5.1 Materials	25
	2.3.5.2 Evaluation Metrics	26
	2.3.5.3 Visualization	26
	2.3.5.4 Connected Components	26
	2.3.5.5 Ensemble Prediction	28
2.4	Discussions	28
2.4.1	Main Contributions	29
2.4.2	Future Work	30
	2.4.2.1 Generalization Ability to Other Datasets	30

2.1 Background

2.1.1 Image Segmentation

In computer vision, image segmentation is the process of partitioning a digital image into multiple segments. The goal of segmentation is to simplify and change the representation of an image into something more meaningful and more natural to analyze

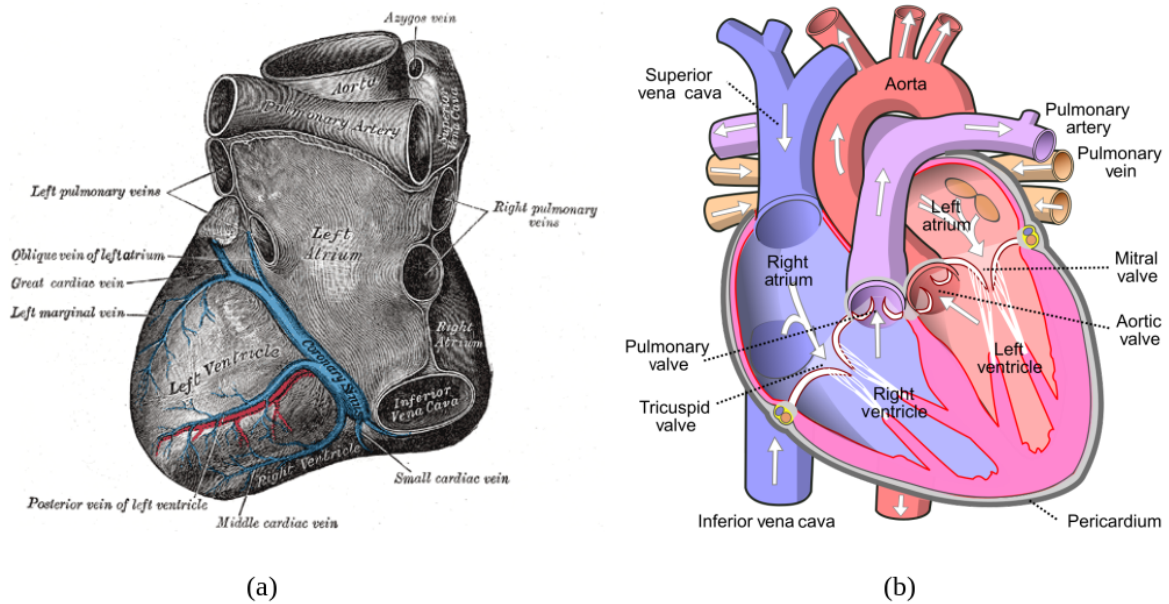


Figure 2.1: (a) Base and diaphragmatic surface of heart, from the 1918 edition of *Anatomy of the Human Body*, by Henry Gray (1821–1865) [Gray, 1878]. ; (b) *Heart Flow* [Wapcaplet, 2006].

[Shapiro and Stockman, 2001; Barghout and Lee, 2004], assigning a label to every pixel in an image such that pixels with the same label share specific characteristics [Singh and Singh, 2010]. Image segmentation is typically used in medical imaging to locate organs, lesions and to draw their boundaries (lines, curves, curved surfaces).

Image segmentation serves as an essential prerequisite to computational anatomy analysis in order to identify pathological shape features. Anatomical structures of the heart have proven to be related to pathology development and treatment outcome in arrhythmia patients [Kirchhof et al., 2016; Bisbal et al., 2013, 2018].

2.1.2 Heart Structure

As shown in Fig. 2.1, the human heart consists of four chambers: upper left and right atria; and lower left and right ventricles. Our study focuses on the left atrium. The left atrium is connected with four pulmonary veins, and an appendage called the left atrial appendage or the left auricle. It is separated from the right atrium via the inter-atrial septum. During the cardiac cycle, the blood flows from the pulmonary veins to the left atrium, then through the opening of the mitral valve to the left ventricle, and then circulates to the aorta and the body.

The anatomy of the left atrium presents high intersubject variations, which makes its segmentation a challenging task. Differences lay in the number and distribution of pulmonary veins, the morphology of the appendage, and the curvature of the body. In some cases, the left inferior and superior veins may be connected via a common ostium, called common left trunk. The appendage may look like a "chicken wing" for

some subjects, while for others, it may look similar to a "cauliflower", "windsock" or "cactus" [Lupercio et al., 2016].

2.1.3 Imaging Modalities

Evolving imaging techniques have allowed us to extract detailed anatomies non-invasively. Among different imaging techniques, CT and MRI images exhibit high and consistent quality.

Computed tomography (CT) images are computed using multiple projection data measured from different angles to reconstruct cross-sectional/tomographic slices. They display relative linear attenuation values of tissues and can be used in tissue classification. The intensity values of CT images are Hounsfield units (HU), transformed from the original linear attenuation coefficient measurement. The intensity value for distilled water at standard pressure and temperature is fixed at zero, while for air, it is at -1000 HU.

In current clinical practice, CT imaging is valuable to provide accurate anatomical geometries for procedural registration in electro-anatomical mapping systems [Tops et al., 2005]. More recently, the systematic use of CT was further justified by its ability to rule out thrombus before ablation [Romero et al., 2013].

Magnetic resonance imaging (MRI) uses strong magnetic fields to generate images of human organs. Different from CTs, MR images need intensity normalization in the pre-processing step. MRI is not applicable in patients with metal implants, in which cases, CT images are a suitable alternative. Nevertheless, metal artifacts may be introduced in CTs. MRI is recognized in assessing delayed enhancement in the left atrial wall [Flüchter et al., 2007] and for imaging adipose tissue [Gronemeyer et al., 2000].

2.1.4 Previous Work

Previous studies tested model-based segmentation methods for the segmentation of the left atrium, such as shape-constrained deformable models and auto-selection from multi-atlas models [Tobon-Gomez et al., 2013; Kutra et al., 2012]. Segmentation methods with weak or no prior, including region growing, also possess high potential in this task thanks to the sharp contrast at the level of the endocardium.

Recently, the development in hardware, with Graphics Processing Unit, enables the implementation of deeper (larger) neural network models and reduces time to train a model. This evolution allows testing more parameters, network settings, and structures in a given period. With its continuous development, the neural network has shown significant advantages in visual and image processing problems [Cecco et al., 2017].

Convolutional neural network (CNN), a type of deep feedforward network, has been widely applied in image-related tasks and shows clear advantages of high-efficiency.

Based on CNN, [Ronneberger et al., 2015] proposed the original U-Net structure, which was later extended to 3D. Its structure with drop out and skip connection mitigates overfitting and improves performance. Previous studies reported numerous applications of CNN for the task of cardiac image segmentation [Oktay et al., 2017; Zheng et al., 2018], and more fields in medical imaging [Litjens et al., 2017; Liu et al., 2018].

Previous studies also showed that 3D CNN outperformed 2D CNN when dealing with 2D sequence issues. [Tran et al., 2015] used 3D CNNs to extract temporal and spatial features, and experimented with different sets of data. [Hou et al., 2017] used 3D CNN to detect and segment pedestrians in a video sequence.

The challenging issue with neural networks is how to measure and mitigate the risk in robustness and explainability, especially in clinical practice. I present first a semi-automatic pipeline based on region growing, and then a neural network model trained on 500+ samples with expert segmentation generated using the interactive method. In the end, I compare these methods ranging from traditional active contour to the neural network and discuss the perspective of image segmentation tasks, which is one of the most popular research field in medical image analysis currently.

2.2 Semi-Automatic Segmentation Method

We introduce first the interactive pipeline using region growing combined with patient-specific intensity value threshold, to segment the left atrium with high accuracy and reliability.

Following the pipeline illustrated in Fig. 2.2, the images were manually cropped around the region of interest, namely the left atrium. The intensity values outside the range from -500 HU to 500 HU were set to nearer bound so as to obtain a better visualization of the blood pool, muscles, and other tissues within the region that is meant to be segmented. After this pre-processing, we summarize our method into the following steps:

1. Drawing polygons on axial slices of CT images to isolate the left atrium².
2. Sampling intensity values of blood and muscles.
3. Segmenting the left atrial endocardium using region growing according to intensity values statistics.

Implementation This interactive pipeline has been implemented in MUSIC software³ [Cochet et al., 2013].

The expertise of clinicians is integrated as they define the boundary of the region of interest in images in the first step of polygon drawing (details in Fig. 2.3). This step

²For step 1, polygons are drawn manually on a dozen of slices for each case and then interpolated automatically on the rest. Images are shown in axial planes.

³Multimodality software for specific imaging in cardiology, developed by IHU Liryc, University of Bordeaux, and Inria Sophia Antipolis

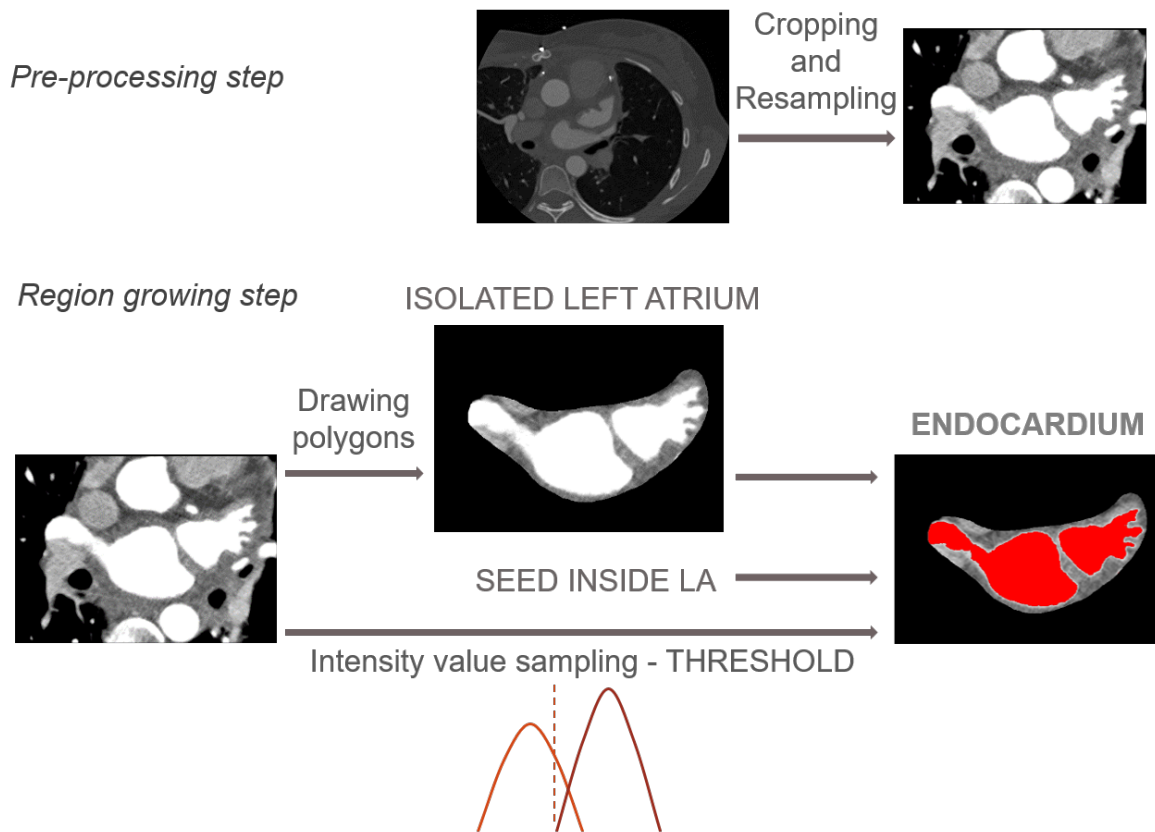


Figure 2.2: The flowchart of semi-automatic left atrial endocardial segmentation - pre-processing and region growing.

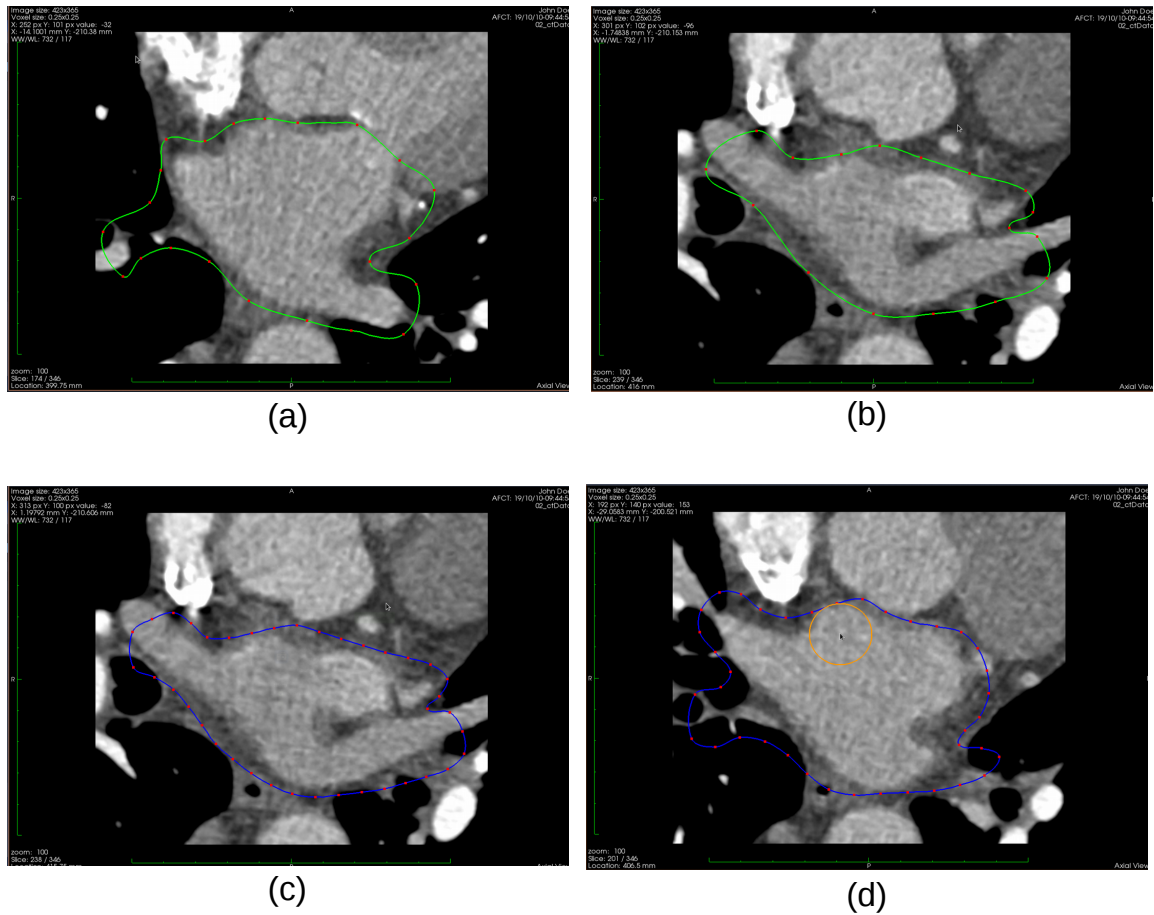


Figure 2.3: *Interactive isolation of the left atrium. (a), (b) show polygons (green) drawn manually and used for interpolation; (c),(d) show automatically interpolated polygons (violet) on the rest slices, (d) shows the manual correction tool (orange circle).*

is essential in separating the left atrium from structures with similar intensity value range in images, such as the aorta.

2.2.1 Region Growing

Region growing is an iterative procedure to segment a connected component, which differentiates itself from the surrounding environment in terms of intensity value. We planted a seed of one pixel inside the left atrium. As the blood pool is a connected component, the seed was raised into a growing region within the polygon boundary. At each iteration, neighboring pixels next to the growing region whose intensity values fell within a certain range were considered part of the left atrium blood pool. The region evolved until no additional pixel was assigned. To determine whether a pixel belonged to the left atrium, we assumed that the intensity values of each tissue follow a Gaussian distribution. Statistical analysis was performed on the intensity values

of tissue samples. Given the histogram of muscle samples and blood samples, we computed the mean and standard deviation of intensity values, for muscles $I(\mu, \sigma^2)$ and for blood $I'(\mu', \sigma'^2)$. Then we set a threshold to distinguish these two classes as

$$th = \frac{\mu\sigma' + \mu'\sigma}{\sigma + \sigma'}. \quad (2.1)$$

Neighbor pixels of the growing region with intensity values upper than the threshold th were assigned to the left atrium. Accordingly, spatial constraint and user-provided intensity information are combined in the algorithm.

2.2.2 Post-Processing

To negate the impact of noise in original CT images, alternating sequential filters (ASFs) were used to post-process the left atrial endocardium segmentation. This step is compulsory for CT images with low quality. Alternating sequential filters are composed of pairs of idempotent morphological filters with structuring elements of increasing sizes. They extract the geometrical characteristics and minimize the distortion of objects [Jean, 1983; Pei *et al.*, 1997]. In our experiment, we used pairs of closing and opening with structuring elements of increasing radius from 0.25 mm, 0.50 mm to 0.75 mm sequentially.

2.2.3 Testing on Public Database

The STACOM 2016 Left Atrial Wall Segmentation Thickness Measurement Challenge provided 10 3D CTs from patients with AF. Coronary Computed Tomography Angiography (CCTA) was performed on a Philips 256 iCT scanner. All patients were injected with an intravenous contrast agent. The scans were ECG-gated in a single breath-hold. The images were acquired at 0.5 mm in-plane resolution with a slice thickness of 1 mm, and reconstructed to a 0.8 to 1.0 mm slice thickness with a 0.4 mm slice increment and a 250 mm field of view. The image matrix was kept at 512×512 matrix, constructed with a sharp reconstruction kernel [Karim, 2016]. The 10 CTs were chosen to include scenarios of both good and tedious image quality.

2.2.4 Performance and Image Quality

This method was used by a radiologist to create 3D pre-ablation anatomy models and works well for the public database despite the varying image quality. The performance of the pipeline relies on plausible image quality and an appropriate threshold th in the region growing.

Because the step of polygon drawing can be modified directly by clinicians using the interactive software interface, as shown in Fig 2.3, the results of our method are highly accurate. They can be used for manual ground truth creation.

As the manual manipulation is time-consuming, the approximated processing time for a radiologist to segment one case is 15 – 30 min. Fully automatic segmentation methods could significantly reduce image processing time.

2.3 From Semi-Automatic to Fully-Automatic

2.3.1 U-Net

U-Net and its variations have been demonstrated to be the state of the art for medical image segmentation in benchmark studies. U-Net has a typical encoder-decoder neural network structure. The input images are encoded by the CNN layers in the encoder. The output characteristics and the feature maps at different feature levels of the encoder serve as input to the decoder. The decoder executes an inverse layer-by-layer decoding. Such a codec structure can effectively extract image features at different resolution levels to analyze the images at different scales.

Based on CNN, [Ronneberger *et al.*, 2015] proposed the original U-Net structure. Traditional 2D U-Net has achieved excellent results in the field of medical image segmentation [Li *et al.*, 2018]. However, it performs convolution on the 2D slices of the images and cannot capture the spatial relationship between slices. Its 3D extension [Çiçek *et al.*, 2016] expands the filter operator into 3D space. This feature takes into account the spatial continuity between slices in medical images, and may better reflect shape features of the corresponding anatomy.

3D U-Nets showed clear advantages compared with traditional feature extraction algorithms [Zeiler and Fergus, 2014; Bengio *et al.*, 2013]. 3D U-Net was also used in [Çiçek *et al.*, 2016] to realize semi-automatic segmentation of volumetric images, and in [Oktay *et al.*, 2017] to segment the ventricle from magnetic resonance (MR) images. Its structure with drop out and skip connection mitigates overfitting and improves performance.

2.3.2 Dual 3D U-Nets - Cropping and Segmenting

The 3D U-Net I used is a specialization of the 3D U-Net proposed in [Çiçek *et al.*, 2016]. The implementation of U-Net follows the work of [Isensee *et al.*, 2017]. We propose a successive dual 3D U-Net architecture, illustrated in Fig. 2.4. Due to memory issues when dealing with 3D images, the network consists of two successive 3D U-Nets. The first U-Net is used to locate the segmentation target in a low-resolution version of the image. The second U-Net performs detailed segmentation from a high resolution cropped region of interest. We introduce a new loss function, Contour loss for the second U-Net. Results are shown in Section 2.3.5.

The first 3D U-Net (Fig. 2.5) locates and coarsely extracts the region of interest. Its input is MR images normalized and re-sized to [128, 128, 128]. Its output is preliminary predicted masks of the left atrium. We keep the largest connected component in the masks and compute the spatial location of the left atrium. Then, we crop the MR images and ground truth masks with a cuboid centered at the left atrium.

The second network (Fig. 2.6(top)) performs secondary processing of the cropped images using the full resolution. Because the higher is the image resolution, the more demanding is the network for memory, we keep only the region around the left atrium as input images, to preserve information that is essential for left atrial segmentation.

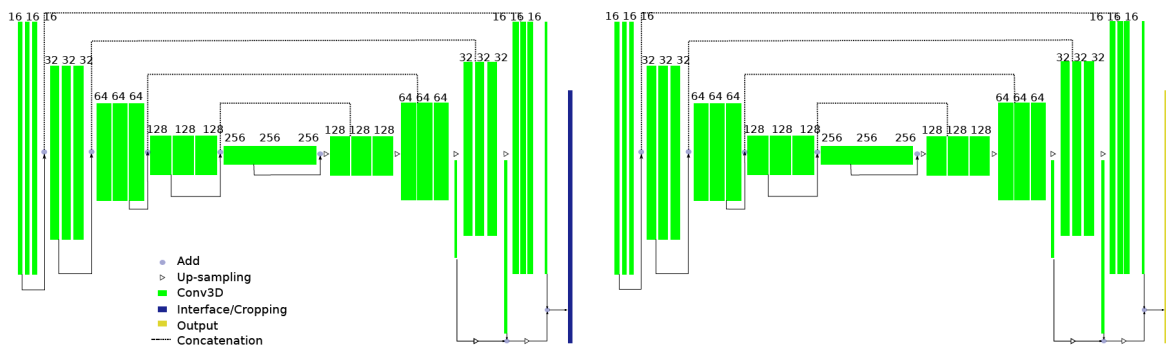
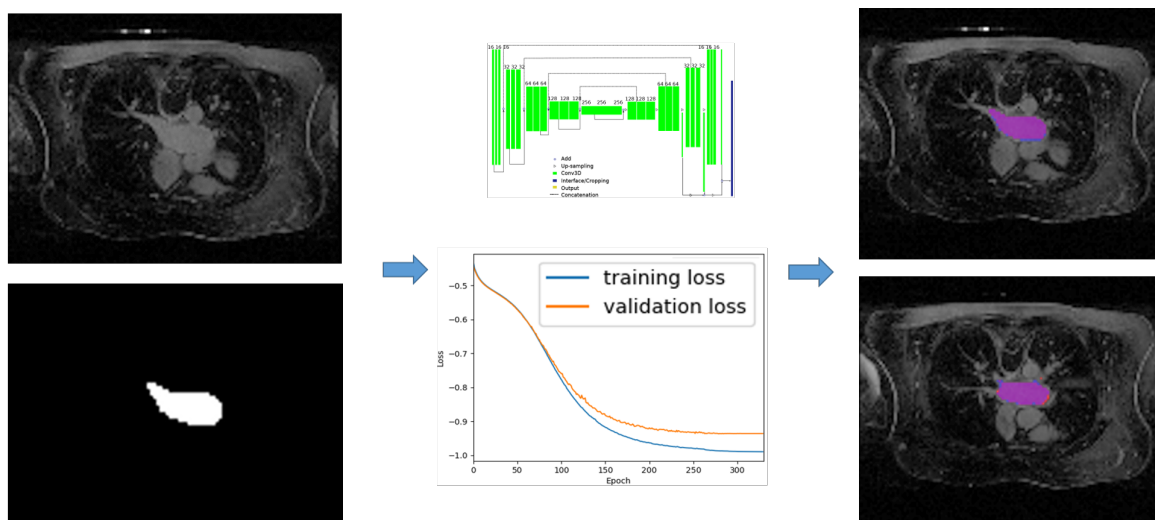


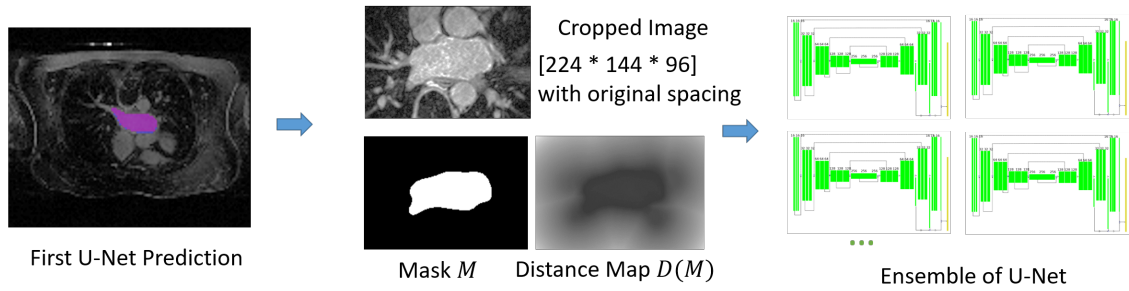
Figure 2.4: Proposed dual 3D U-Net structure. Green blocks represent 3D features; Dark blue refers to interface operation to crop the region of interest based on first U-Net prediction.



Resampled Image [128 * 128 * 128]

Figure 2.5: The framework of successive U-Nets training I: the first U-Net - low resolution cropping. We show here axial slices of MR images, overlapped with manual segmentation of the left atrium in blue, our segmentation in red, the intersection of the two in purple.

Training Step



Ensemble Prediction Step

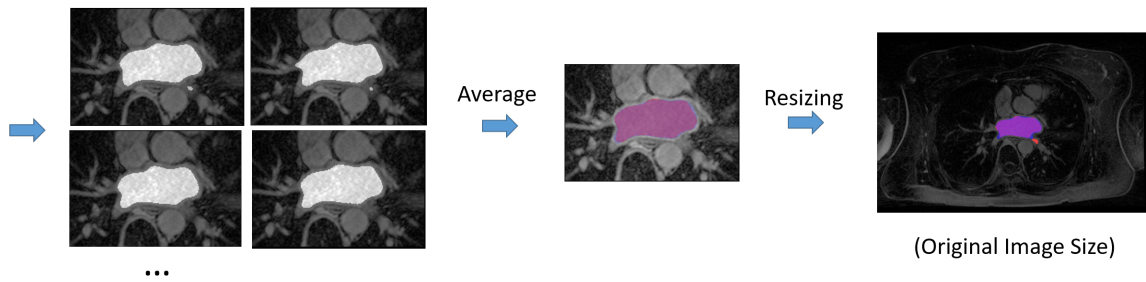


Figure 2.6: The framework of successive U-Nets training II: the second U-Net - segmenting, with ensemble prediction models.

Also, this allows reaching a higher resolution on the region of interest with the same amount of memory resource. The input for the second U-Net is MR images cropped around the predicted left atrium without resampling of size [224, 144, 96]. Its output is our prediction for the left atrial segmentation. We train the second U-Net with two kinds of ground truths, binary segmentation masks M and Euclidean distance maps $D(M)$. Here, we introduce a new loss function based on Contour distance.

2.3.3 Loss Functions

Using Dice coefficient as loss function can reach high accuracy. However, experiments show that, because the inside of the left atrial body accounts for most pixels, the network would stop to optimize when it finds satisfying segmentation of the left atrial body. Instead of the volume inside, the contour is what we want to obtain accurately for the segmentation. It is challenging to segment accurately, especially the region around the pulmonary veins and the appendage. Hence, we introduce the Contour distance into the loss function. Previous work [Oktay et al., 2017] introduced an anatomical regularization factor into the model, while we choose to use loss function at the pixel level.

The definition of a Hausdorff distance is symmetric between two point sets. However, to make it easy to be implemented in neural networks, we do not compute the

distance map of the changing prediction P in the training process, and use a unitary distance:

$$loss_{contour} = \sum_{p \in C(P)} \min_{m \in M} \|p - m\|_2 = \sum (D(M) \circ C(P)), \quad (2.2)$$

where \circ performs element-wise multiplication. P is the prediction of the U-Net, after sigmoid activation of the output layer. $D(M)$ is the distance map to the ground truth segmentation M . $C(P)$ is the contour of the prediction.

To compute a contour of the predicted left atrium, we can

- apply 3D Sobel filters on P and add the absolute value of results in three directions:

$$C(P) = |P * s_x| + |P * s_y| + |P * s_z|, \quad (2.3)$$

where $*$ denotes 3D convolution operation and $+$ denotes pixel-wise addition. s_x , s_y and s_z are 3D Sobel–Feldman kernels in x-, y- and z-direction, for example:

$$s_z = \left[\begin{bmatrix} +1 & +2 & +1 \\ +2 & +4 & +2 \\ +1 & +2 & +1 \end{bmatrix}, \begin{bmatrix} 0 & 0 & 0 \\ 0 & 0 & 0 \\ 0 & 0 & 0 \end{bmatrix}, \begin{bmatrix} -1 & -2 & -1 \\ -2 & -4 & -2 \\ -1 & -2 & -1 \end{bmatrix} \right]. \quad (2.4)$$

- clip the value in that range $[0.1, 0.9]$ from the probabilistic map.

The distance maps $D(M)$ illustrate how far is each pixel from the ground truth contour of the left atrium. We compute the distance for pixels inside and outside the left atrium based on the Euclidean distance transform algorithm implemented in Scipy. The value of the distance is set to be positive both inside and outside the left atrium, because we want to contour to fall exactly onto the boundary.

In the optimization process, the Contour loss $loss_{contour}$ decreases when the contour of the prediction is closer to the ground truth contour. However, the $contour(P)$ is consistently equal or larger than zero (Eq. 2.3). If $D(M)$ is positive, a wrong global minimum exists: if prediction P remains empty, $C(P) = 0$ and therefore the loss is zero. To avoid this, we need to add a *drain* on distance maps $D(M)$.

For example, we set $drain = -1.8$, and therefore $D(M) + drain$ has negative value on the contour of M , since all pixels on the contour of M have an Euclidean distance $\leq \sqrt{3}$. This negative value creates a drain channel for the model to continue the optimization process towards negative loss value.

$$loss_{contour} = \sum ((D(M) + drain) \circ contour(P)). \quad (2.5)$$

The loss function is differentiable and converging in 3D U-Net training trials.⁴

2.3.4 Model Training and Predicting

Contour loss provides spatial distance information for the segmentation, while the Dice coefficient measures the volume inside the contour. We combine these two loss functions in an ensemble prediction model. We visualize the process in Fig. 2.6 (bottom).

⁴The code is available on https://gitlab.inria.fr/sjia/unet3d_contour.

2.3.4.1 Fixed Experimental Setting

In this study, we set the batch size to 1. The training-validation split ratio equals to 0.8. Intensity normalization layers are added. The initial learning rate is $5e^{-4}$. The learning rate is set to be reduced to half after 10 epochs if the validation loss is not improving. The early convergence is defined as no improvement after 50 epochs. The number of base filters is 16. The maximum number of epochs is 500, and 200 steps per epoch. Using a large initial learning rate reduces the time to find the minimum and may overstep the local minima to converge closer to the global minimum of the loss function. However, the accuracy of segmentation also relies on when we stop the training to avoid over-fitting.

We use a computation cluster with GPU capacity 6.1 for training. The first U-Net takes around 200 - 300 epochs to reach convergence. We extract the largest connected components in predictions of the first U-Net to crop the original MRI images around the left atrium, without re-sampling, of size [224, 144, 96]. The second U-Net takes around 150 - 200 epochs to reach convergence. Then the prediction results of the second U-Net are re-sized without re-sampling to the original image size.

2.3.4.2 Varying Experimental Setting

For the second U-Net, we change on the one hand, the options for augmentation: horizontal/vertical flip set to True or False; rotation range set to 0, 7, 10 degree; width/height shift range set to 0.0 - 0.1; zoom in or not, zoom range set to 0.1, 0.2. On the other hand, we alter the loss function option, Dice coefficient and Contour loss.

We also apply the concept of **bootstrapping** in cross-validation, as detailed in Sec. 1.5.2.2. We trained a pair of U-Nets with the same parameters, but with randomly split training-validation samples for each, to mitigate the bias introduced by choosing a particular training dataset.

2.3.4.3 Overall Prediction

We choose multiple U-Net models trained with the above experimental settings, with satisfying performance in validation datasets (Dice $>$ 0.90) for ensemble prediction. The final segmentation prediction is based on the average of all probability maps generated by the U-Nets at a pixel level. We call this a majority voting system with degrees of confidence, similar to letting multiple agents vote for each pixel how likely it belongs to the left atrium.

2.3.5 3D GE-MRIs Atrial Segmentation Challenge Database

2.3.5.1 Materials

The STACOM 2018 Atrial Segmentation Challenge provides a total of 100 3D GE-MRIs (Gadolinium Enhanced) from patients with AF. The original resolution of the data is $0.625 \times 0.625 \times 0.625$ mm³. 3D MR images were acquired using a clinical whole-body

MRI scanner, and experts in the field manually segmented the corresponding ground truths of the left atrial masks to compare with all submissions.

2.3.5.2 Evaluation Metrics

We assess the segmentation results of individual U-Net, trained with different experimental settings, as described in Sec. 2.3.4.2, to compare the prediction performance using Dice loss and Contour loss.

The evaluation metrics are the Dice coefficient, Hausdorff distance (HD), and confusion matrix. Multiple evaluation metrics provide us different views to assess the performance of models. Based on the results shown in Table 2.1, we can conclude that

- The Dice index for predicted segmentation in validation datasets attained 0.91 - 0.92.
- The sensitivity of prediction was around 0.90 - 0.94 and the specificity 0.99.
- The proposed method closely segmented the atrial body, with both loss functions, compared with manual segmentation.
- Different from traditional Dice loss, models trained with Contour loss in general offered smaller Hausdorff distance with similar Dice coefficient.

2.3.5.3 Visualization

We visualize the predicted segmentation results of validation datasets in Fig. 2.7 in a 3D view. Case 1 and Case 2 are selected to represent, respectively, a good scenario and a bad scenario.

- Differences using the two loss functions laid in the boundary, the region close to the pulmonary veins and septum.
- With the Dice loss function, there were more details and sharp edges, and therefore more disconnected spots not belonging to the left atrium.
- With the Contour loss function, the smoothness of the contour, and shape consistency were better maintained.

2.3.5.4 Connected Components

The left atrium should be a single connected component in the binary segmentation mask. We present in Table 2.2 the number of connected components in raw predictions given by U-Nets and compare the two loss functions.

- Using Contour loss produced less wrongly-segmented disconnected components that do not belong to the left atrial structures.

Table 2.1: Comparison of the loss functions: Dice coefficient loss (top) and Contour loss (bottom), with various evaluation metrics computed on validation datasets segmentation for each U-Net model. The darker the gray color, the better the performance.

Performance of U-Nets	Confusion Matrix		Dice	Contour distance (pixel)		
	Sensitivity	Specificity		Average HD	HD	
Model (Dice loss)	1	0.93 ± 0.03	0.99 ± 0.00	0.910 ± 0.032	1.71 ± 0.53	34.29 ± 15.00
	2	0.94 ± 0.04	0.99 ± 0.00	0.913 ± 0.029	1.63 ± 0.57	27.39 ± 12.19
	3	0.91 ± 0.05	0.99 ± 0.00	0.914 ± 0.023	1.62 ± 0.42	30.04 ± 11.76
	4	0.92 ± 0.04	0.99 ± 0.00	0.920 ± 0.030	1.41 ± 0.51	23.50 ± 12.34
	5	0.91 ± 0.05	0.99 ± 0.00	0.918 ± 0.019	1.47 ± 0.47	21.66 ± 7.75
	6	0.91 ± 0.04	0.99 ± 0.00	0.921 ± 0.024	1.45 ± 0.48	26.52 ± 16.14
	7	0.92 ± 0.03	0.99 ± 0.00	0.923 ± 0.027	1.40 ± 0.67	23.38 ± 12.03
	8	0.93 ± 0.04	0.99 ± 0.00	0.927 ± 0.024	1.28 ± 0.46	22.48 ± 16.35
Model (Contour loss)	1	0.90 ± 0.05	0.99 ± 0.00	0.911 ± 0.020	1.60 ± 0.41	19.80 ± 6.82
	2	0.92 ± 0.04	0.99 ± 0.00	0.906 ± 0.045	1.60 ± 0.58	18.88 ± 7.13
	3	0.91 ± 0.04	0.99 ± 0.00	0.917 ± 0.025	1.48 ± 0.51	21.57 ± 8.13
	4	0.92 ± 0.04	1.00 ± 0.00	0.917 ± 0.024	1.40 ± 0.33	20.21 ± 7.53
	5	0.90 ± 0.04	1.00 ± 0.00	0.919 ± 0.024	1.53 ± 0.51	24.81 ± 6.57
	6	0.89 ± 0.03	1.00 ± 0.00	0.921 ± 0.019	1.58 ± 0.59	24.04 ± 11.72
	7	0.91 ± 0.04	0.99 ± 0.00	0.914 ± 0.021	1.56 ± 0.47	22.65 ± 7.52
	8	0.92 ± 0.04	1.00 ± 0.00	0.917 ± 0.030	1.41 ± 0.45	19.66 ± 4.52

Table 2.2: The number of connected components found in predicted segmentation, the smaller, the more regular.

	Number of Connected Components	Maximum
Models (Dice loss)	2.85 ± 2.83	20
Models (Contour loss)	1.28 ± 0.65	5

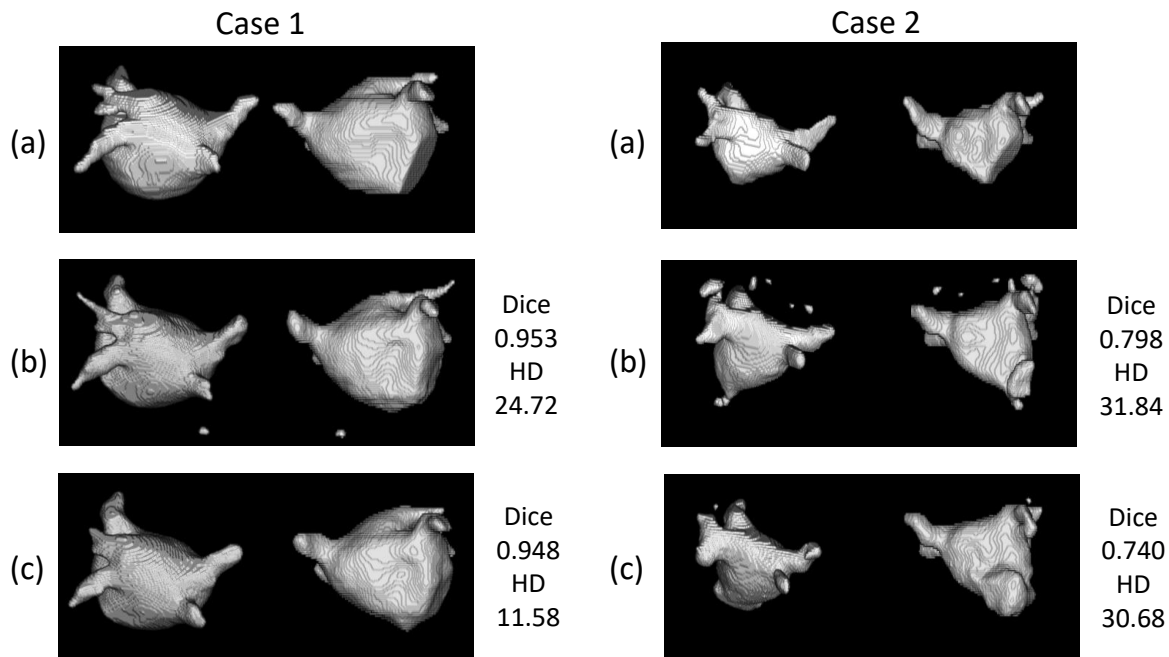


Figure 2.7: Visualization of a good and a bad scenario of validation datasets segmentations, with their Dice, Hausdorff distance (HD) compared with the ground truth. (a) manually segmented; (b) predicted with Dice coefficient loss; (c) predicted with Contour loss.

2.3.5.5 Ensemble Prediction

To reduce the irregular bumps and disconnected components, we chose 11 trained U-Net models in total with both loss functions, to perform an ensemble prediction for testing datasets. We added the probabilistic prediction maps of all U-Nets and threshold their sum ≥ 5.5 .

With Dice loss, more details can be captured. With Contour loss, the shapes looked more regular and smoother globally.

The difficult regions to segment remained the septum and especially the appendage for both loss functions.

The manual segmentations were usually performed slice-by-slice, in which case, sudden discontinuity existed between two axial slices. While our segmentation was based on 3D operators, the segmented region was continuous between slices, which accounts for part of mismatch between manual segmentation and network segmentation that cannot be avoided.

2.4 Discussions

We worked in collaboration with clinicians from Bordeaux University Hospital, on a growing database of 500+ multi-detector CT 3D images. Using the dual U-Net structure, we could achieve a Dice of 0.97 for the task of the left atrial endocardial

segmentation, and the average distance between prediction and ground truth was less than the size of a pixel.

Compared with the region growing algorithm with manual interaction, the neural network has shown significant advantages in efficiency (processing time), which makes it more appealing for practical usage. Compared with different fully-automatic model-based segmentation methods, U-Nets, among other algorithms used by the Atrial Segmentation Challenge participants, performed better in terms of the Dice coefficient. However, given that the loss function of U-Net models during the training phase might be set to be variations of the Dice coefficient, we cannot conclude that U-Nets perform better than the other more conventional methods. Instead, the robustness of neural network models needs to be measured. Manual modification and validation are necessary as a post-validation for implementations in clinical practice.

The difficult regions to segment remain the septum and especially the appendage for both methods.

The atrial segmentation is particularly useful for the computational anatomy studies to explore correlations between shape features with clinical factors in AF such as age, gender, type of arrhythmia, AF duration, the occurrence of stroke, RF duration/number of procedures to restore sinus rhythm.

2.4.1 Main Contributions

We introduced an interactive region growing pipeline to segment semi-automatically the left atrial endocardium, the inner chamber of the left atrium. The region growing framework integrates spatial constraint, user-provided intensity information, and clinical knowledge of the left atrial structure. Experienced radiologists can manually draw polygons around the left structures on the images.

The usage of 3D operators captures spatial continuity of the left atrial structures in images and results in smooth segmentation with the slice-to-slice mismatch.

To achieve fully-automated segmentation, we developed an efficient dual U-Net model based on CNN, to accurately localize and then segment the left atrium from CT images. We proposed to include distance information. We created a Contour loss function, with which the prediction showed smaller Hausdorff distance with similar Dice coefficient, and produced less wrongly-segmented granules not attached to the left atrium. The new loss function achieved a fine-tuning of contour distance and ameliorated shape consistency.

We improved the robustness using an ensemble technique of combining several U-Nets into a stronger model, deploying the concept of bootstrapping, and majority voting. This technique reduces the impact of random effects. Experiments show that the proposed method well captured the anatomy of the atrial volume in 3D space from both MRI and CT images. It was proven efficient for two different types of data, the left atrial segmentation and the renal cortex segmentation.

Aimed at facilitating the segmentation of the left atrial structures, these methods are partially implemented in the MUSIC software for clinical use. The automated segmentation model based on expert segmentation can in return reduce manual workload

for clinicians and has promising applications.

2.4.2 Future Work

2.4.2.1 Generalization Ability to Other Datasets

A common issue with neural network models is that the models can only recognize the image comparable to these in the training database. In collaboration with SysAFib project, we are also testing our trained model with external datasets from Maastricht University.

We continue the segmentation of the left atrial structures in Chapter 3, with a focus on the thin left atrial wall, which inner layer segmentation is given in this chapter.

In Chapter 4 and Chapter 5, the computational anatomy analyses are based on the 3D anatomical model generated from the binary segmentation mask of the left atrium.

"When the sun has set, one's heart is moved by the sound of the wind and the hum of the insects."

— Sei Shōnagon

CHAPTER 3

Myocardial Tissue Analysis

Analyzing the detailed structure of the left atrium can potentially lead to new strategies for atrial ablation. Precise measurement of the left atrial wall thickness helps determine the radio-frequency dose to create transmural scars, and the local myocardial thickness demonstrates relation with atrial fibrillation (AF) pathology.

Most previous works to assess the left atrial structures rely on ruler-based measurements instead of performing a prior segmentation. The task of segmenting the left atrial wall is challenging due to the generally thin layer, insufficient image quality, and similar neighboring structures attached to the left atrium.

We present a marker-controlled geodesic active contour (MC-GAC) model to segment the left atrial epicardium indirectly from cardiac computed tomography (CT) images, taking into account external constraints in its surrounding environment. The segmentation is also the first step to measure epicardial fat. The method integrates the expertise of clinicians via patient-specific parameters, although this choice remains optional owing to the robustness of the approach.

We participated in a benchmark study on an open-source CT image database. Our method was proved to be efficient, robust in case of artifacts, and achieved a high correlation in wall thickness measurement with ground truth.

The preliminary predictions were used as weak supervision to train a U-Net, during which we observed a "compensation" effect. The network was capable of learning that the target was muscle tissues, and was not misguided by inevitable defects from MC-GAC.

Part of this chapter corresponds to the following scientific articles:

1. Jia S, Cadour L, Cochet H, Sermesant M. STACOM-SLAWT challenge: left atrial wall segmentation and thickness measurement using region growing and marker-controlled geodesic active contour. In International Workshop on Statistical Atlases and Computational Models of the Heart 2016;211-219 [*Jia et al.*, 2017a].
2. Karim R, Blake LE, Inoue J, Tao Q, Jia S, Housden RJ, Bhagirath P, Duval JL, Varela M, Behar J, Cadour L et al. Algorithms for left atrial wall segmenta-

tion and thickness—Evaluation on an open-source CT and MRI image database. Medical image analysis. 2018;50:36-53 [*Karim et al.*, 2018].

Contents

3.1	Background	32
3.2	Methodology	35
3.2.1	Conventional Estimation	35
3.2.2	Towards Precise Wall Segmentation	37
3.2.2.1	Base Model	37
3.2.2.2	Creation of Excluding Marker	37
3.3	Evaluation on Public Database	38
3.3.1	Dataset	38
3.3.2	Parameters	38
3.3.3	Wall Segmentation	38
3.3.4	Thickness Measurement	39
3.3.5	Participation in Benchmark Study	39
3.4	Training U-Net with Preliminary Results	41
3.4.1	Materials	41
3.4.2	Results	42
3.4.3	Explaining the Model	42
3.5	Discussions	42
3.5.1	Future Work	44
3.5.1.1	Fat Analysis	44
3.5.1.2	Joint U-Net for the Left Atrial Structure Segmentation	45

3.1 Background

Analyzing in detail the structures of the left atrium, including the left atrial myocardium, also called the wall (muscle, fat, fibrosis), can provide precious insights into the pathology of atrial fibrillation (AF), potentially resulting in new strategies for atrial ablation.

In catheter ablation, ablating and scaring using radio-frequency creates lesions in the regions of the atrial wall where ectopic foci are. The formation of small chaotic circuits instead of a regular propagation of electrical signals results in the observation of AF. This invasive procedure establishes transmural lesions to block the arrhythmia while avoiding impairing extra-cardiac tissues. Thereby the radio-frequency power dose to create transmural scars, delivered for ablation during the procedure, relies on local myocardial thickness, which is a vital prerequisite for ablation guidance [*Karim et al.*, 2018].

The local myocardial thickness demonstrates variations by region and by subject [*Ho et al.*, 1999; *Sánchez-Quintana et al.*, 2005]. The reduction of left atrial wall

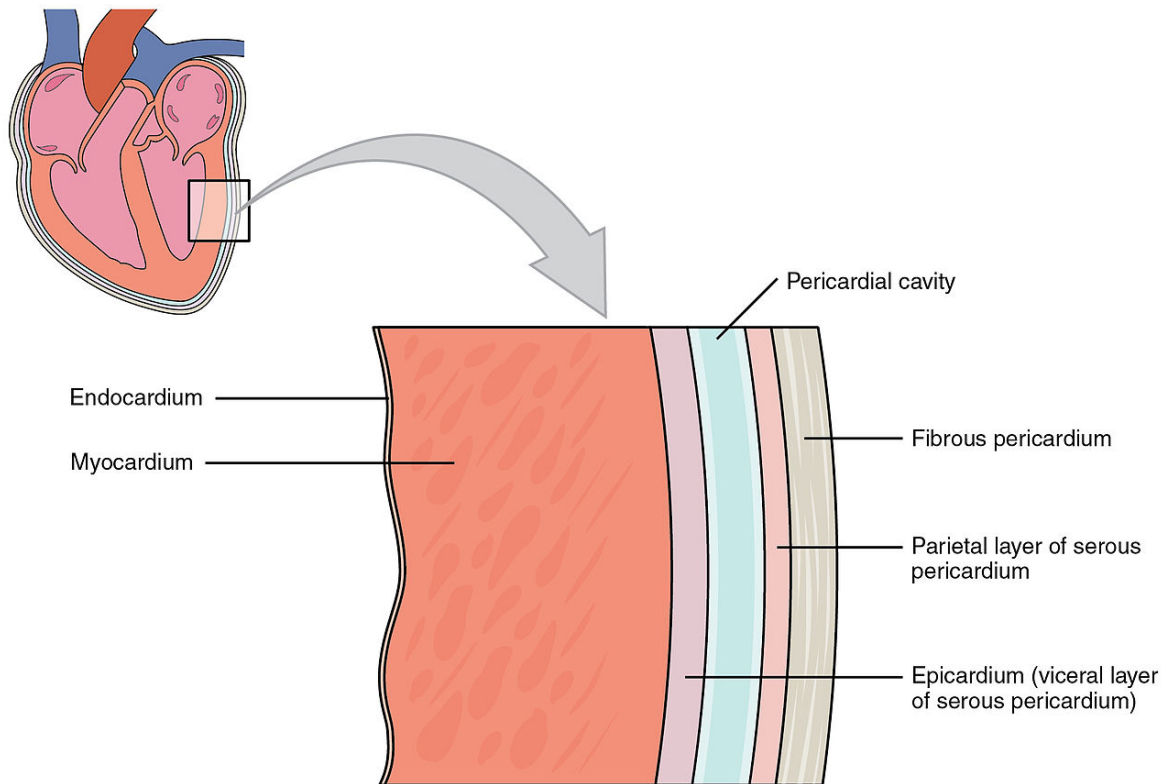


Figure 3.1: Anatomy of the heart wall [OpenStax College, 2013].

thickness also appears in AF patients when compared with controls, according to a study by autopsy [Hassink *et al.*, 2003].

The wall of the heart has three concentric layers that wrap around the atria, from an anatomical point of view. The myocardium refers to an involuntary and striated muscle, which is the histological foundation of the heart. The inner layer is called the endocardium, while the outer layer is called the epicardium, which is also composed of several sub-layers, as shown in Fig. 3.1.

The precision of segmentation is limited by imaging capabilities. An example of cardiac computed tomography (CT) images containing the left atrium is shown in Fig. 3.2. From the image, we can see that the left atrial wall is hardly visible.

Most previous works to estimate the left atrial wall thickness rely on ruler-based measurements performed on 2D slices, without performing a prior segmentation of the wall [Karim *et al.*, 2018]. Several methods have been developed to measure the left atrial wall thickness automatically from CT images. [Dewland *et al.*, 2013] chose to perform a segmentation of the wall in four regions, inter-atrial septum, below right inferior pulmonary vein (PV), appendage, and anterior wall. Whereas [Inoue *et al.*, 2015, 2014] built a pipeline based on a hierarchical constraint structure to perform multi-region segmentation.

The segmentation of the left atrial wall is a very challenging task, as

- The myocardium is very thin, usually within the range of 1 – 4 mm, only several

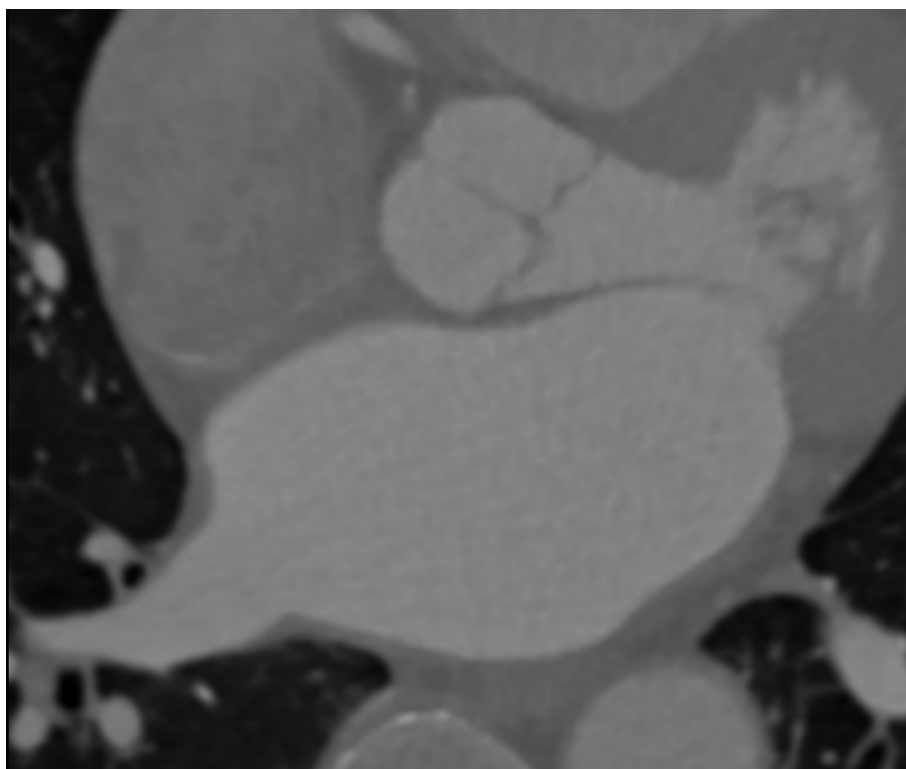


Figure 3.2: Example axial slice of cardiac CT images containing the left atrium.

pixels wide in images.

- The wall is heterogeneous, consisting of mostly muscle but possibly fat granules and fibrosis, especially in patients with myocardial diseases or persistent AF.
- The left atrial wall is attached to structures sharing similar intensity values in images, such as the wall of the aorta.
- The intensity values of muscle, fat, and surrounding tissues vary in each CT image, and their intensity value ranges overlap. The intensity values are affected by the decay of contrast between the peak after injection and the time of imaging.

Thus, there may not be a clear boundary to segment the left atrial wall. The accuracy of the segmentation is difficult to validate, as few manual segmentation or reliable ground truths are available.

To measure patient-specific myocardial and epicardial fat volume¹, the segmentation of the left atrial wall is the first step, as well.

Obesity has been recognized as an indicator of increasing AF burden. Though, the quantification of epicardial adipose tissue is currently not included in AF risk stratification recommendations [Donal *et al.*, 2016].

¹We do not distinguish myocardial fat and epicardial fat in this study. As mentioned previously, these structures are thin and hard to be separated based on current imaging technology.

[*Iacobellis, 2009*] clearly distinguished between the pericardial fat and the epicardial fat. Methods are available to assist in the assessment of pericardial adipose tissue volume [*Nelson et al., 2009*]. Various image modalities are used in fat assessment, such as echography, magnetic resonance imaging (MRI). Previous clinical studies show that pericardial fat is associated with AF and its severity and ablation outcome [*Thanassoulis et al., 2010; Al Chekatie et al., 2010; Wong et al., 2011*]. However, it is much more challenging to study the epicardial adipose tissue. We hope to design a complete, automatic method for accurately quantifying and analyzing the left atrial epicardial fat, making use of the good image quality of CT.

We divide the task of segmenting the left atrial wall into two parts. The previous chapter investigated the left atrial endocardium segmentation. In this chapter, we focus on the left atrial epicardium segmentation².

The intensity value or shape alone is not enough to enable reasonable segmentation. We consider combining thresholding with model-based segmentation methods. We adapt the geodesic active contour (GAC) model [*Caselles et al., 1997*] to segment the left atrial epicardium indirectly. The GAC model is modified to account for external constraints with controlling markers defined in its surrounding environment. The results of the left atrial wall thickness are mapped onto meshes generated from the endocardium segmentation.

The preliminary predictions serve as weak supervision for a U-Net. We use them to train a model to process large image datasets.

Then, we use the intensity value of CT images, displaying relative linear attenuation values of tissues corresponding to the Hounsfield units (HU) scale, to characterize tissues (fat) inside the wall [*Huda, 2010*].

To the best of our knowledge, no previous methods have been proposed to quantify epicardial fat from images automatically.

3.2 Methodology

3.2.1 Conventional Estimation

Without a reliable and tailored segmentation of the left atrial wall, we could use an approximation, which is a dilation of 4 - 8 pixels of the endocardium segmentation, corresponding to a layer of 1 - 2 *mm*. Clinicians estimate that the myocardium is present in this region.

Multi-scale thickness dilation provides a more comprehensive investigation into the epicardial fat tissue. This estimation serves as a benchmark for our segmentation. The pipeline is summarized in Fig. 3.3. The part of the left atrial endocardial segmentation - cropping and region growing filling inner chamber - has been presented in the previous chapter.

²We refer to the segmentation of the region inside the left atrial epicardium as the segmentation of the left atrial epicardium.

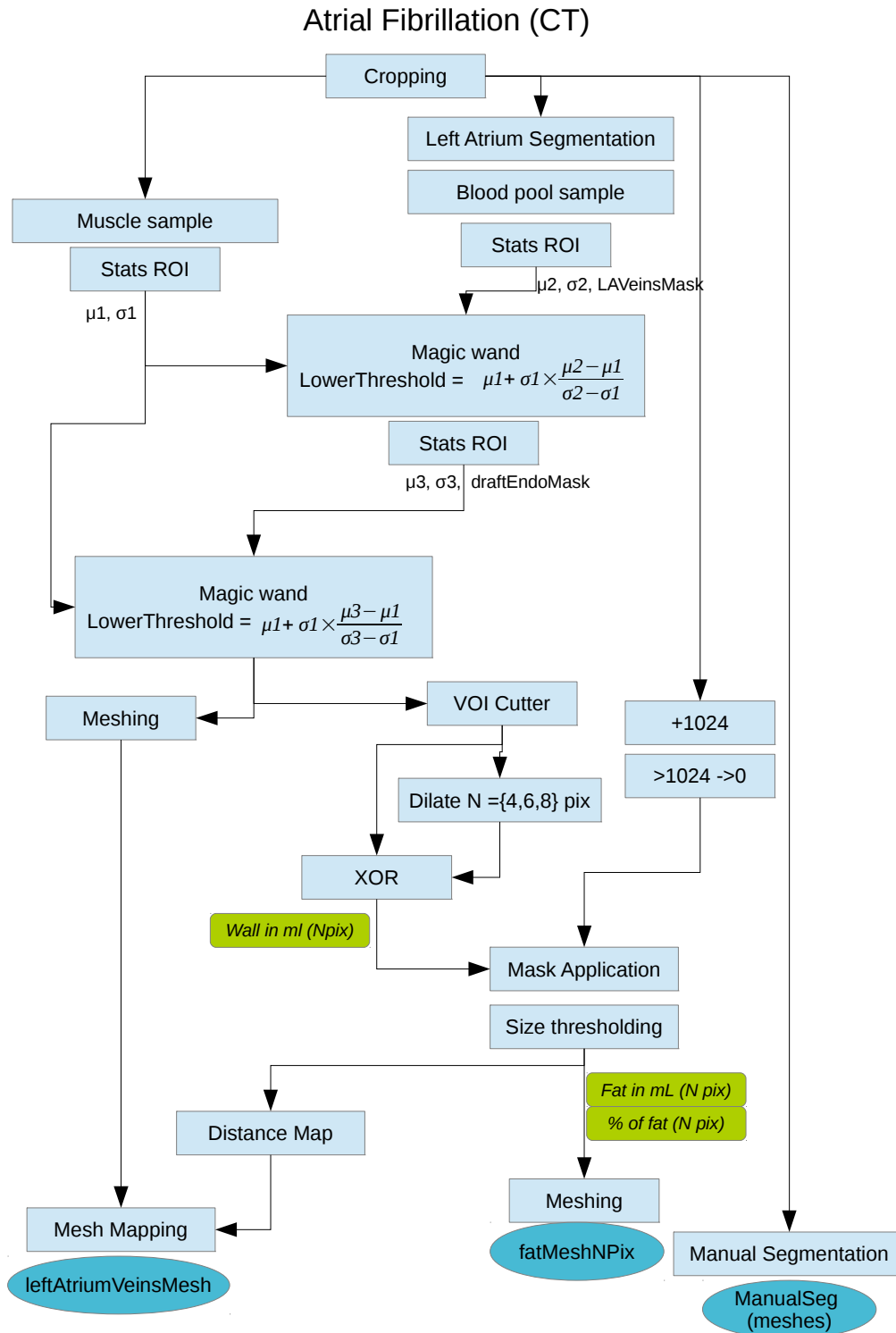


Figure 3.3: Conventional method for epicardial fat analysis.

3.2.2 Towards Precise Wall Segmentation

Because of thinness and low contrast of the left atrial wall, we cannot rely on intensity-based methods alone to achieve the task of left atrial wall segmentation. The idea is to combine the intensity information with shape-based algorithms.

3.2.2.1 Base Model

GAC algorithm [Caselles *et al.*, 1997] represents contour as zero crossing of a level-set function. An initial contour propagates to touch the shape boundaries, as the level-set function progresses in time until

$$\frac{\partial u}{\partial t} = 0, \quad (3.1)$$

where u is the level-set function under following conditions:

$$u|_{t=0} = u_0 \quad (3.2a)$$

$$\frac{\partial u}{\partial t} = g(c + \kappa)|\nabla u| + \nabla u \nabla g, \quad (3.2b)$$

with u_0 the initial level-set function; c a constant to provide a steady velocity; κ related to the curvature of the level-set function as $\kappa = \text{div}(\frac{\nabla u}{|\nabla u|})$; g an edge detector function of image, which is strictly decreasing towards the outside of the region to be segmented and has values near 0 at the boundary to stop the evolution of curves.

In equation 3.2b, three terms affect the way that a level-set function evolves:

- Advection term: $gc|\nabla u|$, related to progression speed of curves.
- Curvature term: $g\kappa|\nabla u|$, related to curvature of curves.
- Propagation term: $\nabla u \nabla g$, related to expansion of curves.

The algorithm is implemented in the Insight Segmentation and Registration Toolkit (ITK), which uses three parameters (advection, curvature, and propagation scaling, noted here as S_a , S_c and S_p) to assign weighting ratios to each term and adjust their influence in the evolution process of the level-set function.

We chose manually $S_a = 10 \times S_c = S_p = 5$, from visual inspection and interaction with clinicians. The initial level-set function u_0 was computed as a distance map of the left atrial endocardium segmentation. The edge detector function g was simply set to 0 on excluded regions and 1 on the rest of the image.

3.2.2.2 Creation of Excluding Marker

As for excluded regions, neighboring tissues other than muscles outside the left atrial wall were marked as excluded for the segmentation. CT images display relative linear attenuation values of tissues that correspond to the Hounsfield scale. Based on approximate HU values for air (-1000), fat (-100 to -50), muscle (10 to 50) and blood (300 to

Table 3.1: Intensity value thresholds used for 10 datasets tested.

Dataset	#1	#2	#3	#4	#5
Threshold th	224.3 HU	419.5 HU	485.7 HU	226.6 HU	131.6 HU
Dataset	#6	#7	#8	#9	#10
Threshold th	136 HU	448.2 HU	358.4 HU	345.8 HU	267.1 HU

400), we set 0 HU as upper threshold for fat (and air) and th , as defined in equation 2.1, as lower threshold for blood. Besides, fat granules of size smaller than 1 mm^3 were regarded as inside the left atrial wall, thus not excluded. Margins were kept to avoid misleading markers resulting from noise or density variation. At last, all pixels further than 6 mm away from the left atrium were also excluded, according to studies of the left atrial wall thickness on excised hearts [Ho et al., 1999; Sánchez-Quintana et al., 2005].

The markers of neighboring tissues were introduced to address the fuzzy boundaries problem, as the intensity gradient between the left atrial wall and its neighboring tissues is small, and noise may blur original CT images. Then, we adapted GAC model based on excluding markers. Because the left atrial wall may be attached to muscles belonging to other organs such as esophagus, aorta, lung, and hence cannot be segmented only based on intensity information. GAC, on the other hand, involves curvature constraint of shape to solve this problem.

3.3 Evaluation on Public Database

3.3.1 Dataset

The segmentation method can be applied to the 10 3D CT images from the STACOM Left Atrial Wall Segmentation and Thickness Measurement challenge, as detailed in Sec. 2.2.3.

3.3.2 Parameters

The parameter setting mentioned in Section 2 can be altered depending on cases. However, we chose to follow the same rule for all 10 cases to test the robustness of the algorithm with respect to different inputs.

Intensity value thresholds th used during region growing process were shown in Table 3.1.

3.3.3 Wall Segmentation

Here we present preliminary results of the left atrial wall segmentation, and comparison with manual segmentation, as shown in Fig. 3.4.

The proposed method closely approximated the wall thickness, as compared with manual segmentation. Differences lay in the segmentation of the anterior left atrial

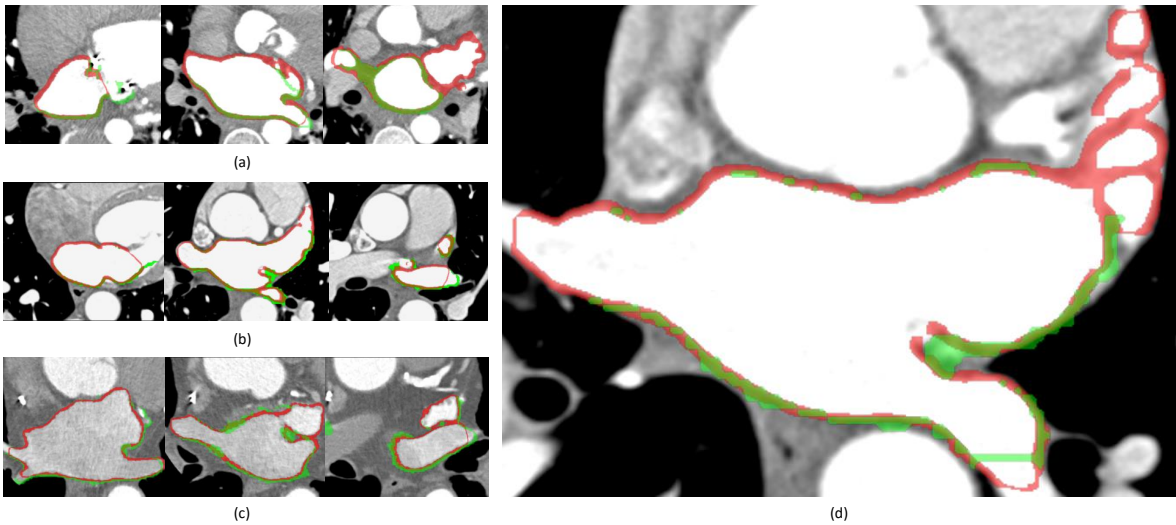


Figure 3.4: Axial slices of CT images, overlapped with manual segmentation of the left atrial wall in green, our segmentation in red, intersection of the two in yellow. (a) Dataset #2; (b) dataset #3; (c) dataset #5; (d) example slice zoomed in.

wall, which is not fully involved in the manual segmentation provided. The intersecting surfaces inside PVs and on the mitral valve are presented in our segmentation with a rather thinner wall, which should not have been included.

Remark. We segmented the left atrial appendage and PVs connected to the left atrium as well, which is different from the manual segmentation provided.

3.3.4 Thickness Measurement

We computed the left atrial wall thickness using the nearest distance from each point on the left atrial endocardium to the left atrial epicardium. Meshes of the left atrial endocardium were generated using The Visualization Toolkit (VTK).

The left atrial wall thickness varies by subject as well as by region, as shown in Fig. 3.5. From the mean and range of the wall thickness, we can see that dataset #8 has a thicker left atrial wall compared with other datasets, whereas dataset #5 and #6 have a thinner left atrial wall. The results for dataset #8 are shown as an example.

Alternating sequential filters may be used to post-process the segmentation results. The left atrial epicardium segmentation, using marker-controlled GAC, takes into account the heterogeneity of the left atrial wall, and therefore can have small granules excluded. Whether or not to smooth the contour of the left atrial epicardium, depends on how the left atrial wall is defined.

3.3.5 Participation in Benchmark Study

[Karim *et al.*, 2018] conducted a benchmark study on an open-source CT image database for the segmentation of the left atrial wall. Three participants devised and implemented

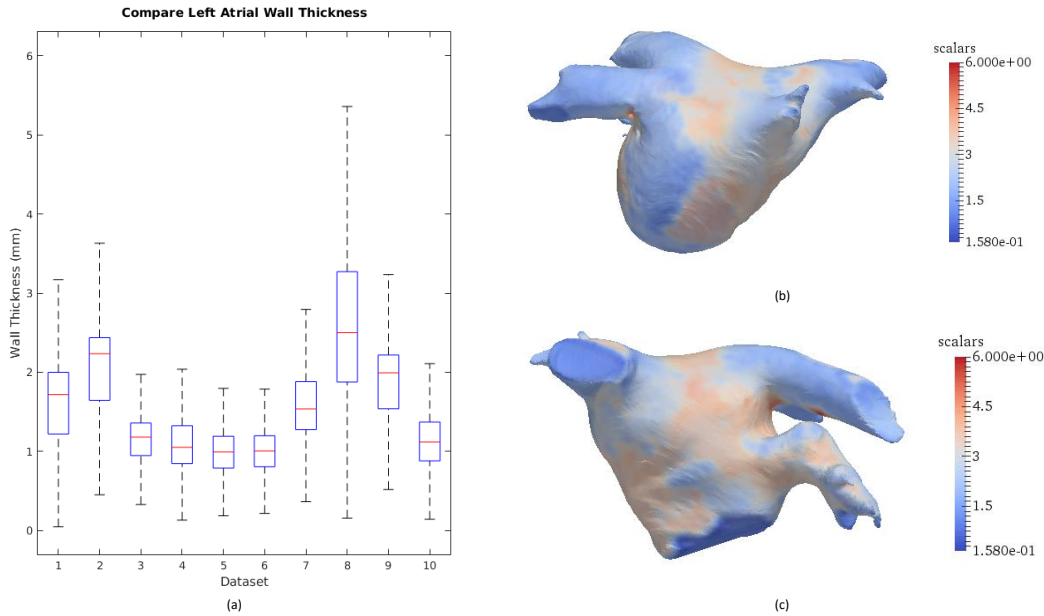


Figure 3.5: (a) Mean and interquartile range of the left atrial wall thickness for 10 datasets tested, with maximum whisker length specified as 1.5 times the interquartile range; (b) left atrial wall thickness map for dataset #8, posterior view; (c) left atrial wall thickness map for dataset #8, anterior view.

algorithms that segmented the atrial wall from CT images. Robarts Research Institute (ROBI) designed a blood pool mesh vertex normal traversal method. Leiden University Medical Centre (LUMC) developed a multi-atlas registration and level-set method. We participated in the study with the MC-GAC method.

The study confirmed that the left atrial segmentation is a challenging task due to the generally thin wall structure. The algorithms were assessed with three metrics: **wall thickness**, **Dice**, and **tissue volume/mass**. The first measurement, the correlation between algorithms and ground truth thickness measurement is shown in Fig. 3.6, which demonstrated that our method (red) achieved high accuracy in terms of wall thickness measurement. The accuracy reduced with degrading image quality. Our method was also robust in the case with the cardiac resynchronization therapy lead artefact.

Second, the Dice metric evaluates the overlap between algorithms and the ground truth segmentation. On the anterior wall, the Dice metrics were 0.33, 0.43, and 0.30 for ROBI, LUMC, and us, respectively. On the posterior wall, the Dice metrics were 0.39, 0.21, and 0.50 for ROBI, LUMC, and us, respectively. The inter-observer Dice was 0.67.

Third, wall tissue mass (in grams) measured by the algorithms were consistently higher than that of ground truth. The inter-observer difference was 10.53 *g*. More details can be found in [Karim *et al.*, 2018].

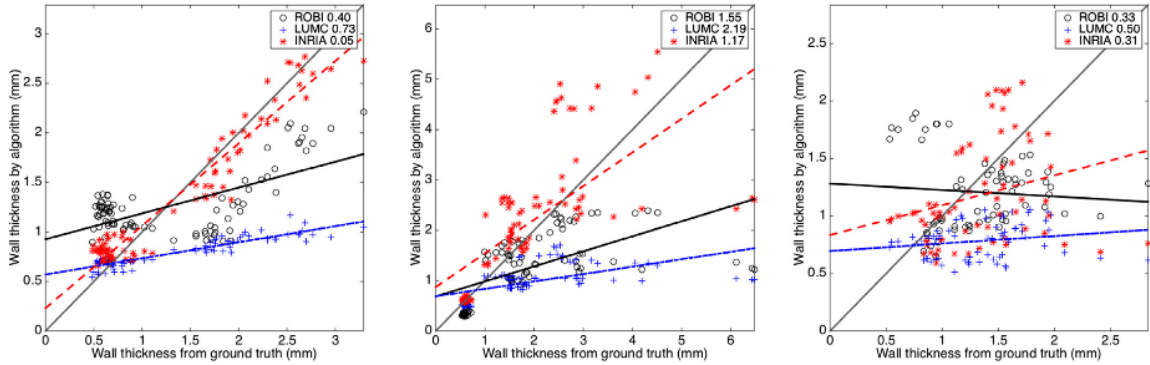


Figure 3.6: Correlation between algorithms and ground truth in the left atrial wall thickness measurement. Illustrated with cases of excellent image quality (left), good (middle), and poor (right) [Karim et al., 2018].

3.4 Training U-Net with Preliminary Results

In this section, we look into using the preliminary segmentations as weak supervision for a U-Net, to train a model to process large image datasets.

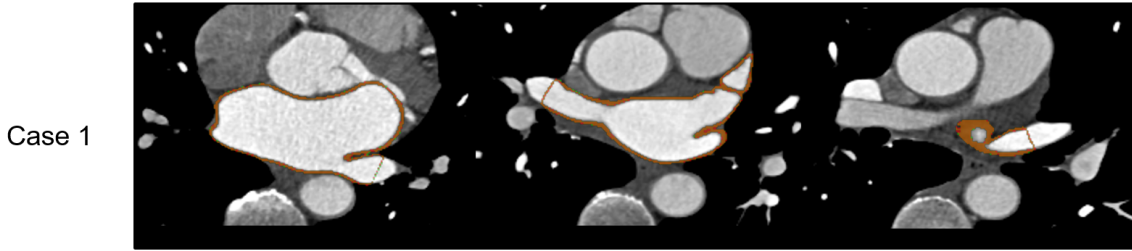
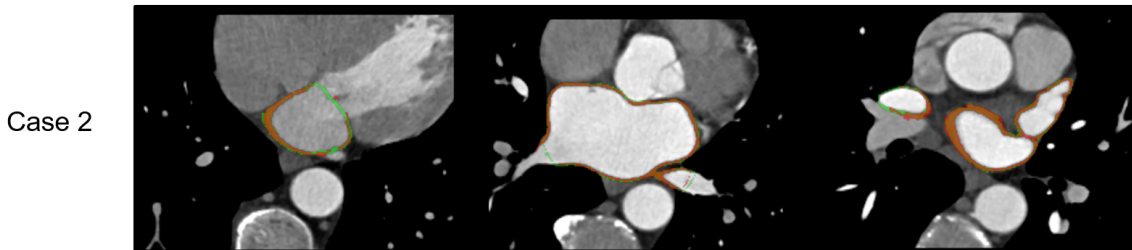
The sampling procedure in MA-GAC requires manual manipulation and is time-consuming. The algorithm performance depends on CT quality and manual verification. Besides, the results with MC-GAC are necessarily connected components, while the actual atrial wall is not, cut at the ostia of the PVs. The labeled results from MC-GAC are not perfect but fairly sufficient. They contain valuable information about which pixels are likely to be muscle and belong to the myocardium. The wide individual variety of left atrial anatomy makes it difficult for a single general algorithm to achieve excellent performance in all cases systematically.

Recent studies look into whether, with a few or only one training case, we could build a neural network model efficiently [Zhao et al., 2019]. We use the preliminary results as training data to train a U-Net to segment the left atrial wall and report the results and effects here.

It is very costly to generate manual segmentation truth for the atrial wall from high-resolution CTs. One option is to use computer-aided painting tools. We generated a few manual segmentations in this way and used them separately as testing datasets.

3.4.1 Materials

We chose 10 high-quality CTs, without metal-induced and minimal motion-induced artefacts, and carefully segmented the left atrial wall using the MC-GAC method. This preliminary analysis generated 10 training datasets, which are augmented in the training phase, including zooming, shifting (0.1 - 0.3), and rotation (0 - 10 degree).

On training dataset**On validation dataset**

Red: Net segmentation

Green: MCGAC segmentation

Figure 3.7: Performance of compensation Net on training and validation datasets.

3.4.2 Results

The segmentation results are illustrated in Fig. 3.7 and Fig. 3.8. From the results, we observed an important "compensation" effect. The network learned by itself that the target was muscle tissues. It is not misguided by the ostia at the PVs, which are inevitable defects from MC-GAC. On both validation and testing datasets, the results of network segmentation did not include the ostia or the mitral valve.

3.4.3 Explaining the Model

To improve the results, we analyzed the results and found that the network identified well the muscle tissue but not well the left atrial structure. It also captures the walls of other neighboring structures, including the aorta and the right atrium.

We compare the activation map of the U-Net described in the previous chapter trained with 500+ datasets for the left atrial segmentation, and the U-Net for the left atrial wall segmentation. We found that the wall segmentation network also looked for features related to the atrial shape, but the feature maps were noisier. The visualization of channels in intermediate decoder activation is shown in Fig. 3.9. This finding may be useful for further developing a joint-segmentation network to perform robust left atrial endocardium and left atrial wall segmentation together.

3.5 Discussions

We proposed an automatic method to address the challenging task of segmenting the left atrial wall, measure the wall thickness, and quantify the epicardial fat in AF. To the

On testing data

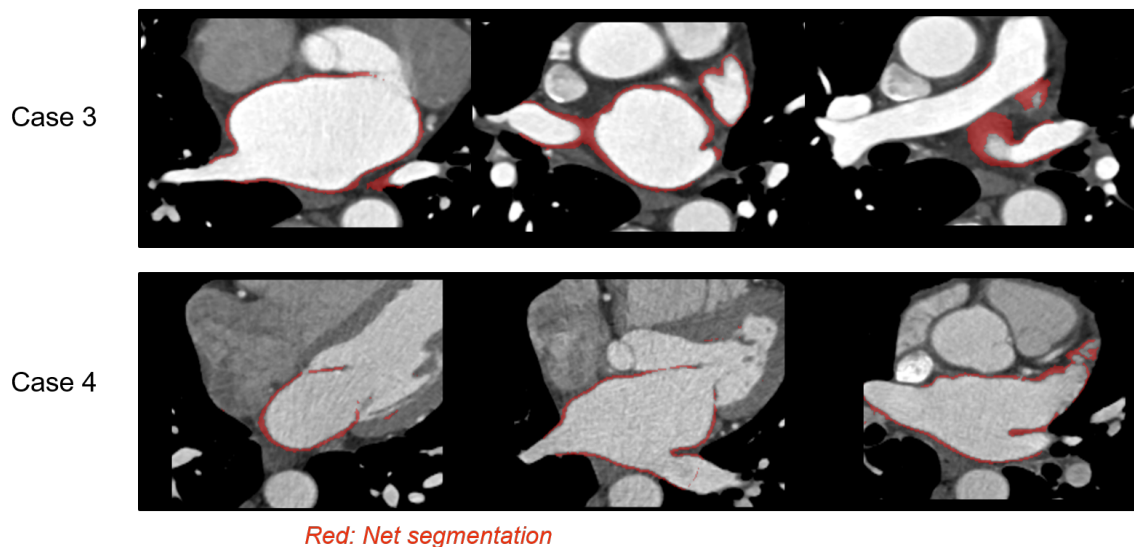
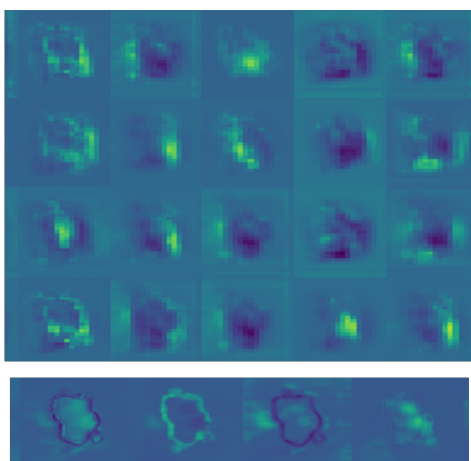


Figure 3.8: Performance of compensation Net on testing datasets.

Model – Endocardium Segmentation



Model – Wall Segmentation

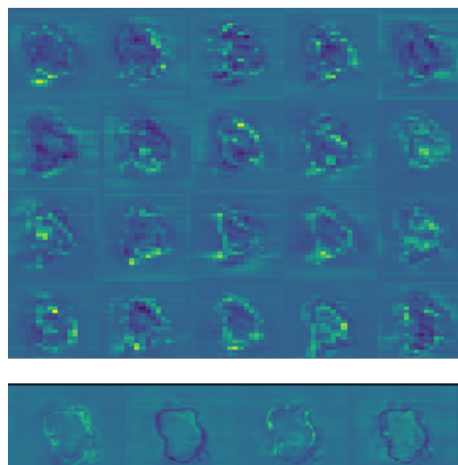


Figure 3.9: Feature maps of the two U-Nets. (a) the model to perform the left atrial endocardium segmentation from previous chapter; (b) the model to perform the left atrial segmentation with a few training datasets. The U-Net for the left atrial wall segmentation also generates features related to the atrial shape, but its feature maps look noisier.

best of our knowledge, no previous methods have been proposed to quantify epicardial fat from images automatically, which limits the study of adipose tissue, potentially related to AF pathological remodeling.

The proposed MC-GAC method makes use of patient-specific intensity value information and the surrounding environment of the left atrial wall. The markers of neighboring tissues were introduced to address the fuzzy boundaries problem, as the intensity gradient between the left atrial wall and its neighboring tissues is small, and noise may blur original CT images. Then, we adapted GAC model based on excluding markers. Because the left atrial wall may be attached to muscles belonging to other organs such as esophagus, aorta, lung, and hence cannot be segmented only based on intensity information. GAC, on the other hand, involves curvature constraint of shape to solve this problem.

We participated in a benchmark study on an open-source CT image database. The MC-GAC achieved a high correlation in wall thickness measurement with ground truth, which supports the potential computational analysis of the wall thickness. Our method was proved to be efficient, robust in the case of artifacts.

Differences lay in the segmentation of the anterior left atrial wall, which is not fully involved in the manual segmentation provided. The intersecting surfaces inside PVs and on the mitral valve are presented in our segmentation with a slightly thinner wall, which should not have been included. Another limitation is that the proposed MC-GAC method, applying uniform parameters to all regions of the left atrial wall, cannot achieve a region-wise constraint on curvature.

Potential future work to improve the accuracy of the segmentation may include: further eliminating the influence of noise; region-wise segmentation of the left atrial wall, which takes into consideration different surrounding environments of the left atrial sub-regions; parameters testing; integrating alternative methods to define how to measure the wall thickness, such as using a symmetric minimum distance between the epicardium and the endocardium [Varela *et al.*, 2015], measuring the thickness in the surface normal direction of the endocardium.

The preliminary predictions were used as weak supervision to train a U-Net, whose feature maps interestingly correspond to the atrial shape. We observed a "compensation" effect of the neural network. The network was capable of learning that the tissue information of the segmentation target, and was not misguided by inevitable defects in the training samples from MC-GAC.

3.5.1 Future Work

3.5.1.1 Fat Analysis

Analyzing fat in the left atrial wall brings insights into AF pathology, and may inspire new ablation strategies in treatment planning. We did a preliminary test to see if the epicardial fat is associated with clinical factors and AF progression using both U-Net with MC-GAC prediction and conventional estimation method, as demonstrated in Fig. 3.10. Fig. 3.10.

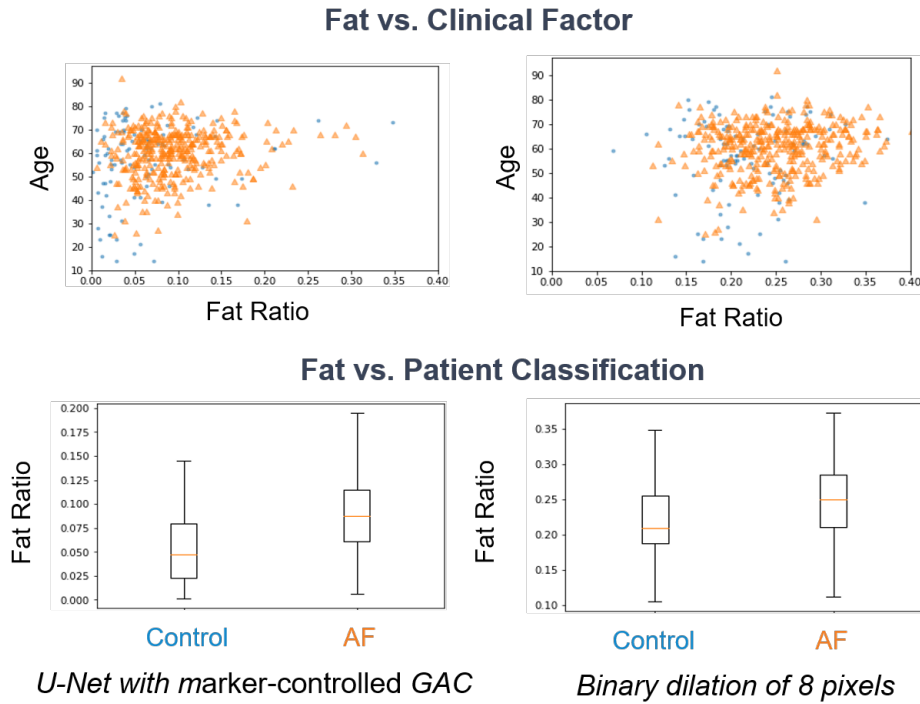


Figure 3.10: *Demonstrating the relation between fat quantification and clinical factors, using U-Net with MC-GAC prediction (left) and Conventional Estimation (right).*

3.5.1.2 Joint U-Net for the Left Atrial Structure Segmentation

The limitation for the left atrial wall segmentation is related to less available manual segmentations. The task is difficult, even for clinicians, to perform a detailed segmentation. However, large datasets with ground truth segmentation for the endocardial segmentation is accessible. The coupled U-Nets to segment both the endocardium and the epicardium should provide improved wall segmentation.

In the next chapters, we discuss computational anatomy analyses, built upon the 3D anatomical models from image segmentation.

"We sit together,
the mountain and me,
until only the mountain remains."

— Li Bai

CHAPTER 4

Shape Analysis

Understanding left atrial remodeling may reveal shape features related to post-ablation outcome in atrial fibrillation (AF), which helps in identifying suitable candidates before catheter ablation. In this chapter, we propose an application of diffeomorphometry and partial least squares regression to address this problem. We evaluate the framework on a large AF database with pre-ablation computed tomography (CT).

We compute a template of the left atrial shape and then encode the shapes using their diffeomorphic deformations from the template. Large sets of vectors/initial momenta associated with the same control points parameterize the deformations. In a two-step partial least squares regression, the first step eliminates the influence of atrial volume in shape parameters. The second step links deformations directly to post-ablation recurrence. It derives a few principle modes of deformation, which are unrelated to volume change but are involved in post-ablation recurrence.

These modes contain information on ablation success due to shape differences, resulting from remodeling or influencing ablation procedure. Some details are consistent with the most complex area of ablation in clinical practice. The extracted features of the left atrial shape provide incremental predictive value, with the area under the receiver operating characteristic (ROC) curves higher than the current state of the art. A multivariate model achieves better prediction capabilities, combining the shape score and conventional indicators.

Finally, we identified critical regions whose local remodeling was associated with arrhythmia recurrence. The adverse structural findings, both global and regional, could lead to potential ablation targets outside pulmonary veins (PVs) for treatment planning.

Part of this chapter is based on the following scientific articles:

1. Jia S, Camaioni C, Rohé MM, Jaïs P, Pennec X, Cochet H, Sermesant M. Prediction of Post-Ablation Outcome in Atrial Fibrillation Using Shape Parameterization and Partial Least Squares Regression. In International Conference on Functional Imaging and Modeling of the Heart 2017;311-321 [*Jia et al.*, 2017b].
2. Jia S, Nivet H, Pennec X, Camaioni C, Jaïs P, Cochet H, Sermesant M. Ar-

rhythmia Recurrence after Catheter Ablation in Atrial Fibrillation: a CT-Based Statistical Study of the Left Atrial Shape. Manuscript submitted.

Contents

4.1	Background	49
4.1.1	Shape	50
4.1.2	Deformation	50
4.1.3	Statistical Learning	50
4.2	Methodology	51
4.2.1	Mesh Generation	51
4.2.2	Extraction of Remodeling Information	53
4.2.2.1	Definition of Registration and Atlas Computation	53
4.2.2.2	Iterative Closest Point (ICP)	53
4.2.3	Quantification of Shape Variations	54
4.2.3.1	Currents Representation of Surface	54
4.2.3.2	LDDMM Framework for Inter-Subject Surface Registration and Atlas Construction	55
4.2.3.3	Implementation Using Deformetrica	57
4.2.4	Extraction of Remodeling Information	58
4.2.4.1	Whitening Transform	58
4.2.5	Statistical Modeling	58
4.2.5.1	Dependency Analysis with Left Atrial Volume	59
4.2.5.2	Correlation with Post-Ablation Recurrence	59
4.3	Materials	60
4.3.1	Data Preparation	60
4.3.1.1	Datasets	60
4.3.1.2	Imaging Protocol	60
4.3.1.3	Endocardium Segmentation	61
4.3.2	Catheter Ablation	61
4.3.2.1	Ablation Procedure	61
4.3.2.2	Follow-up	61
4.4	Preliminary Experiments in Paroxysmal Atrial Fibrillation	62
4.4.1	Population	62
4.4.2	Atlas of the Left Atrium	62
4.4.3	Diffeomorphic Registration	62
4.4.4	Remodeling	63
4.4.5	Principal Component Analysis	64
4.4.6	Partial Least Squares Analysis	65
4.4.7	Principal Modes Related to Post-Ablation Recurrence	66
4.4.8	Predictive Capabilities	66
4.5	Application on an Extended Database	69
4.5.1	Population	69
4.5.2	Benchmarking Left Atrial Descriptors	70

4.5.3	Inference Statistics and Multivariate Models	70
4.5.4	Results	70
4.5.4.1	Univariate Predictability	70
4.5.4.2	Probabilistic Predictive Modeling	71
4.5.5	Heterogeneous Regional Remodeling	71
4.6	Region Segmentation of Left Atrial Meshes	72
4.7	Discussions	73
4.7.1	Main Contributions	73
4.7.2	Limitations and Future Work	75

4.1 Background

To optimize the planning of atrial fibrillation(AF) treatment, researchers have conducted numerous studies to look into predictors of recurrent arrhythmia after catheter ablation. Previous studies reported that hypertension, Holter duration, and left atrial shape measurements [Berruezo *et al.*, 2007; Dagues *et al.*, 2010; Shin *et al.*, 2008; Bisbal *et al.*, 2013] were potentially related to post-ablation recurrence. However, their underlying mechanism is still unclear, as is the left atrial remodeling in AF. In current clinical practice, predictors of AF recurrence are often limited to imaging-based left atrial size measurement and the duration of the most prolonged AF episode. Unfortunately, the assessment of AF duration is not robust, given the prevalence of asymptomatic AF episodes. The left atrial volume index (LAVI) has been the only clinically accessible and reproductive index for identifying suitable candidates for ablation. However, its relation to the post-ablation outcome has been constantly reported to be weak [Marrouche *et al.*, 2014]. The left atrial dimensions or volume show limited incremental predictive power to derive a cut-off threshold for clinical decision-making efficiently [Kirchhof *et al.*, 2016].

Recent studies introduced several markers of the left atrial shape, including roof flattening [Kurotobi *et al.*, 2011], anteroposterior asymmetry [Nedios *et al.*, 2011], sphericity [Bisbal *et al.*, 2013, 2018] and vertical asymmetry [Varela *et al.*, 2017], to predict recurrent arrhythmia after catheter ablation. They assessed how closely the shape of the left atrium resembles that of a perfect sphere, and how asymmetric the shape is. [Oakes *et al.*, 2009] looked into local left atrial remodeling from delayed-enhancement magnetic resonance imaging (MRI).

This study aims to examine the hypothesis that the anisotropic left atrial deformation during remodeling, more comprehensive than LAVI, not necessarily related to enlargement, carries incremental predictive value to prognostic AF assessment.

The introduction of computational methods has significantly improved the efficiency of anatomic studies and made it possible to deal with extensive databases. Computational anatomy provides tools for statistical analysis of shapes in a population, including estimating average organ anatomies, modeling the organ development across time, establishing normal variability, detecting and classifying pathology, and adapting generic (atlas-based) to patients-specific models. The reason to study anatomies is that shape

variations may be related to remodeling of certain biological phenomena that we are interested in investigating, which may be not directly accessible.

Previously, Sec. 2 details how to efficiently segment the left atrium in computed tomography (CT) using automatic algorithms and deep learning. CT imaging ensures detailed and accurate anatomical descriptions. We focus on extracting features from 3D anatomical models of the left atrium and their variability as predictors.

4.1.1 Shape

The shape of organs can be expressed in either a 3D surface model or a 4D (3D + tissue information) volume model. "Shape is what remains when location, size, and rotational effects are filtered out" [Bookstein *et al.*, 1986]. We can use points, curves, or surfaces, a collection of manifolds, to represent deformable shapes. Mathematically, there are various ways to define metrics in the shape space, measuring the distance between each pair of shapes, such as

- Landmark: a set of corresponding points $p_1, p_2 \dots p_n$ on each shape S .
- Varifold: non-oriented surfaces [Charon and Trounev, 2013].
- Mathematical Current: oriented surfaces [Durrleman *et al.*, 2014].

The metric study of shapes can potentially capture more detailed shape characteristics.

4.1.2 Deformation

Deformation refers to the process of transforming one shape into another shape, which encodes the variations or biological variability of the shapes. Unlike in [Varela *et al.*, 2017], we propose an application of diffeomorphometry to quantify patient-specific shape variations. The deformations of organs are smooth and unfoldable. Thus it is reasonable to choose to work on diffeomorphisms [Trounev, 1998]. Diffeomorphisms deform shapes through the orbit, resulting in invertible and folding-free deformations. The metric between two diffeomorphisms is defined as the shortest length or geodesic flow in the orbit of shapes. The choice of the metric and regularization parameter affects the geometric structure of the space of deformations under consideration.

The initial velocity fields parameterize the trajectory in the space of diffeomorphic deformations. They belong to a Reproducing Kernel Hilbert Space (RKHS), which can be generated with a Gaussian kernel.

4.1.3 Statistical Learning

Previous clinical studies deployed the shape-based statistical learning framework recently [Bruse *et al.*, 2016]. Under the condition that a consistent framework to represent the shape is available, we can correlate the shapes with clinical factors that measure the degree of illness or treatment outcome. By studying principal deformation modes associated with a higher post-ablation recurrence rate, we expect to find cartographic/local criteria that help us stratify the risk of post-ablation recurrence.

One approach is principal component analysis (PCA) with pathological analysis, which calculates the correspondences on modes of variation for subjects and relates the low-dimensional shape representation to clinical parameters to identify the mode related to pathology. Resulting modes may be influenced by noise, and therefore modes with low variances should be discarded.

Contrarily, PLS regression recognizes the components that are directly linked to recurrence, discarding noise in the shape space. Thus, some studies applied partial least squares regression (PLS) to predict deformation patterns that were related to a certain axis, for example, normal or not. PLS has been applied in the recent decade in medical imaging [Ablitt *et al.*, 2004; Rao *et al.*, 2008; Mansi *et al.*, 2011]. Given that it has been proven more compact, more precise, and provided better predictions compared to PCA regression in some studies, we intend to test these methods and explore the best results.

Details of PCA and PLS formulation can be found in Appx. A.

We further account for the dependency on current routine predictors, in particular, LAVI, and devise a two-step PLS regression approach, eliminating the influence of atrial volume in shape parameters in the first step.

4.2 Methodology

To analyze the comprehensive left atrial shape in AF, we firstly generate meshes (triangle-composed surfaces, which estimate the shape of an object) of the left atrium based segmentation from 3D CT images. Using the iterative closest point (ICP) algorithm, we register all meshes rigidly to be close to one common location in space. After that, we calculate the atlas/average shape of the left atrium for this population. Then, with *currents* representation of surface and large deformation diffeomorphic metric mapping (LDDMM), deformation from the atlas towards each subject is quantified as a set of vectors, initial momenta, which corresponded to the specific left atrial shape for each subject. Shape features could then be described and analyzed using statistical modeling in two steps, dependency analysis with LAVI, and correlation with post-ablation outcome.

4.2.1 Mesh Generation

As we obtained binary masks of the left atrium from the previous step, we generated meshes (triangle-composed surfaces, which estimate the shape of an object) of the left atrium, as illustrated in Fig. 4.1. The left atrial meshes include the left atrial appendage (LAA) and the pulmonary veins (PVs) (cut about 1 cm from their ostia).

For mesh generation, we tested two methods separately: VTK [VTK, 2016] and CGAL [CGAL, 2016].

- VTK: in VTK library, `vtkTriangleFilter` generated a 3D surface composed of triangles, given an input 3D contour. Afterward, smoothing might be needed to correct imperfections that resulted from segmentation and original imaging.

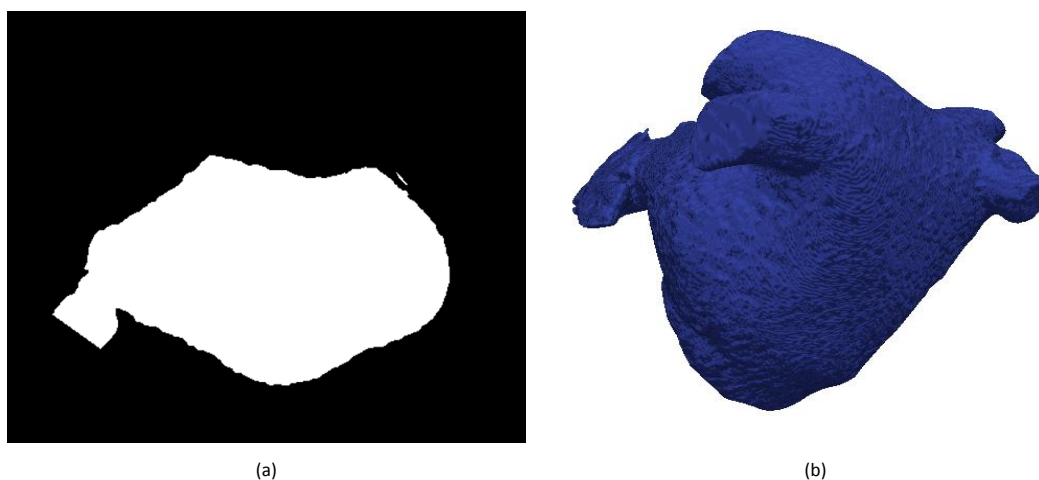


Figure 4.1: *Mesh generation: from binary mask to triangle-composed surface. (a) Example axial slice of binary mask; (b) mesh generated, here we refer to a triangle-composed surface.*

vkDecimateFilter was applied to reduce the number of triangles, and thus, the size of mesh files.

- CGAL: different from VTK, the resulting mesh of CGAL is a 3D volume tetrahedral subcomplex of a restricted Delaunay triangulation, in a class providing various iterators on mesh elements [Jamin *et al.*, 2015]¹. The regularity of mesh elements was controlled via input parameters (allowed range for the angle in tetrahedrons, size of triangles). Delaunay refinement process eliminated the violation of criteria concerning the size, shape of mesh cells, and surface facets, while optimization processes also improved mesh quality and minimized the mesh energy/error. In our case, we extracted the surface from the output volume mesh to represent the left atrium.

Comparison of the two methods: CGAL generated meshes with higher quality, especially it kept meshes significantly more regular even after size reduction; VTK library is more popularly employed in currently algorithms in medical image analysis. Besides, CGAL meshes were of smaller size compared with VTK meshes, which benefited the speed of computation. In total, we chose CGAL mesh generation and made it work for the next steps. Some examples of mesh generation results of the two methods are shown in Fig. 4.2. We choose to use CGAL meshes for the tasks where the LAA complex and other details can be ignored.

¹We used CGAL 3D mesh generation algorithm http://doc.cgal.org/latest/Mesh_3/index.html.

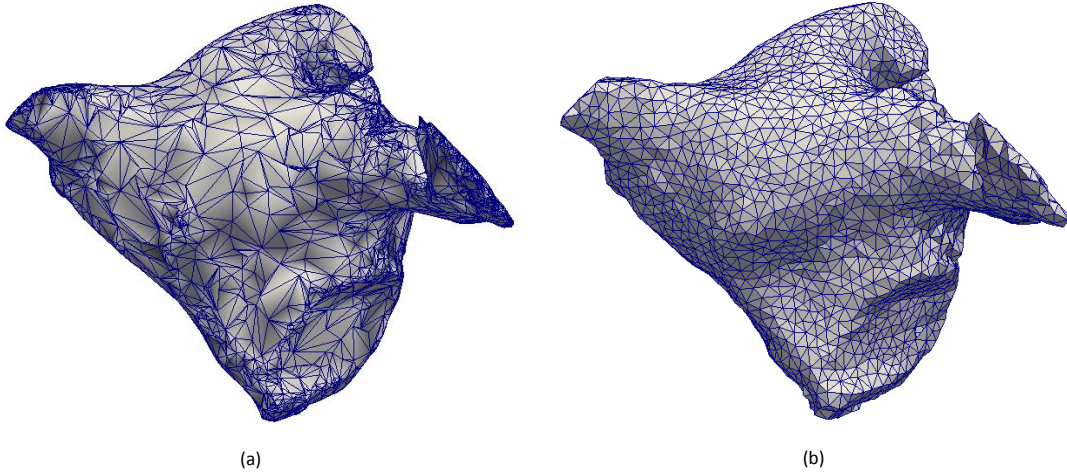


Figure 4.2: Comparison of the two methods VTK and CGAL in mesh generation. (a) VTK mesh; (b) CGAL mesh. CGAL shows significant improvement in mesh regularity while VTK describes details of the left atrial appendage better.

4.2.2 Extraction of Remodeling Information

4.2.2.1 Definition of Registration and Atlas Computation

Here, we define some basic notations for the following text, unless otherwise stated. For patient $\#i$, the surface S_i could be represented as the sum of deformed template T and some residuals δ_i , as

$$S_i = \phi_i(T) + \delta_i. \quad (4.1)$$

For registration, we minimized the residuals δ , in other words, the distance between S_i and $\phi_i T$. For atlas construction, we minimized the sum of distances from the template to every mesh, resulting in a Fréchet mean of shape complex,

$$T = \arg \min_T \sum_i d^2(T, S_i). \quad (4.2)$$

The template and the deformations were estimated simultaneously.

4.2.2.2 Iterative Closest Point (ICP)

A rigid alignment of all meshes was performed in the first place, to reduce the impact of different origin in CT images. The iterative closest point (ICP) algorithm was applied to calculate an optimized rigid registration in the least square sense.

ICP minimizes the distance between two meshes or two clouds of points. We used ICP as a pre-processing step to bring all meshes to be close to a given location in

the space, in preparation for the diffeomorphic registration in the next step. More specifically, we used rigid transformations to limit the loss of information.

$$\text{Criterion : minimize } \sum_{\phi_i} d^2(\phi_i(S_i), S_0) \quad (4.3)$$

Essentially, the algorithm consists of following steps: finding the closest point in the target cloud of points for each point in the source cloud of points, estimating the optimized point-to-point rigid translation using a mean squared error cost function, and iterating these two steps.

As mentioned before, shapes can be represented by a collection of manifolds, points, curves, or surfaces. Here, in the case of clouds of points $p_1, p_2 \dots p_n$, the distance between two shapes S (resp. S') are given by

$$d^2(S, S') = \sum_{k=0}^n \|p_k - p'_k\|^2 \quad (4.4)$$

4.2.3 Quantification of Shape Variations

We encoded patient-specific left atrial shapes variations, applying diffeomorphometry. The term refers to the comparison of shapes and forms using a metric structure based on diffeomorphism. Methods under this framework have been proven to be efficient to qualify anatomical configurations and their differences for computational anatomy studies [Miller *et al.*, 2014].

4.2.3.1 Currents Representation of Surface

To compute on anatomic variety, we have to formulate the representation of shapes mathematically first. In the following context, shapes refer to surfaces, by default. There are several ways to do so, for example, spectral decomposition [Lombaert *et al.*, 2014], Riemannian manifolds. I introduce here a powerful method, mathematical *currents*, to represent surfaces.

The basic principle of the currents approach is to probe a surface by a set of vector fields in a space W , subset of the square integrable three-dimensional vector fields. In this way, a surface S is represented by a current, which maps any vector field w in W to the flux of the vector through the surface as

$$C_S(w) = \int_S w(x)^t \vec{n}(x) d\lambda(x). \quad (4.5)$$

In equation 4.5, $\vec{n}(x)$ is the unit normal of the surface at a point x , and $d\lambda$ is the Lebesgue measure on the surface. The space W , called the test space, is chosen as the set of convolutions between any square integrable vector field and a smoothing kernel. Hence, W is a RKHS. In this work we use a Gaussian kernel, which can be defined, for any points (x,y) , as

$$K_W(x, y) = \exp \left(- \frac{\|x - y\|^2}{\lambda_W^2} \right), \quad (4.6)$$

where λ_W is the standard deviation. With this choice of reproducing kernel, we can then control a metric in the space of currents that allows the distance between two surfaces to be efficiently computed, though other choices of kernels are possible. This space also has the important property that it is the dense span of basis vector fields of the form $w(x) = K_W(x, y)\beta$, for any fixed point y and fixed vector β . As a consequence, any vector field w can be written as an infinite linear combination of the basic elements $K_W(x, y)\beta$. We can also define an inner product in W using the kernel K_W with these basis vectors as

$$\langle K_W(\cdot, x)\alpha, K_W(\cdot, y)\beta \rangle_W = \alpha_t K_W(x, y)\beta. \quad (4.7)$$

This inner product holds for any vector field $w(x) = K_W(x, y)\beta$ in W .

The space of currents is defined as the *dual* space of W , denoted W^* , representing the vector space of linear mappings from W to \mathbb{R} . Since W is a RKHS, the evaluation functionals are bounded. According to the properties of W (the fact that W is densely spanned by the vector fields $w(x)$, and has an associated inner product) its dual space W^* is densely spanned by the dual representations of the basis vectors $w(x)$, called the Dirac delta currents, defined as

$$\langle \delta_x^\alpha, w \rangle_W = \langle K_W(x, \cdot)\alpha, w \rangle_W = \alpha_t w(x, y). \quad (4.8)$$

Given that W^* is a vector space, we can define the sum of two surfaces (represented by currents) C_{S_1} and C_{S_2} (obtained from equation 4.5) as $(C_{S_1} + C_{S_2})(w) = C_{S_1}(w) + C_{S_2}(w)$. In terms of the flux, this means that the flux through the sum of two surfaces is the sum of the flux through each surface. The vector space property of scalar multiplication in this case means that we can scale a current by simply scaling the Dirac delta currents. We can also define an inner product in W^* as

$$\langle \delta_x^\alpha(w), \delta_y^\beta(w) \rangle_{W^*} = \langle K_W(\cdot, x)\alpha, K_W(\cdot, y)\beta \rangle_W = \alpha_t K_W(x, y)\beta. \quad (4.9)$$

In summary, shape S can be represented by flux of 3D vector field/current w across the surface, that belongs to a Gaussian RKHS W with kernel K_w . The current w was parameterized by a set of $\vec{\delta}_{c_k}$, attached to distinct points on surface S .

A key advantage of the currents representation is that a metric can be defined, which does not assume point correspondences between surfaces. Rather than measuring the Euclidean distances between points on the surface, surfaces are compared at a global level. The distance between two surfaces can then be expressed as the norm of the difference between the surfaces, which is the distance between their currents [Guibert *et al.*, 2013]:

$$\|C_{S_1} - C_{S_2}\|_{W^*}. \quad (4.10)$$

4.2.3.2 LDDMM Framework for Inter-Subject Surface Registration and Atlas Construction

LDDMM framework uses a group of diffeomorphisms constructed through the integration of time-varying velocity fields, determined by the initial velocity at time $t = 0$

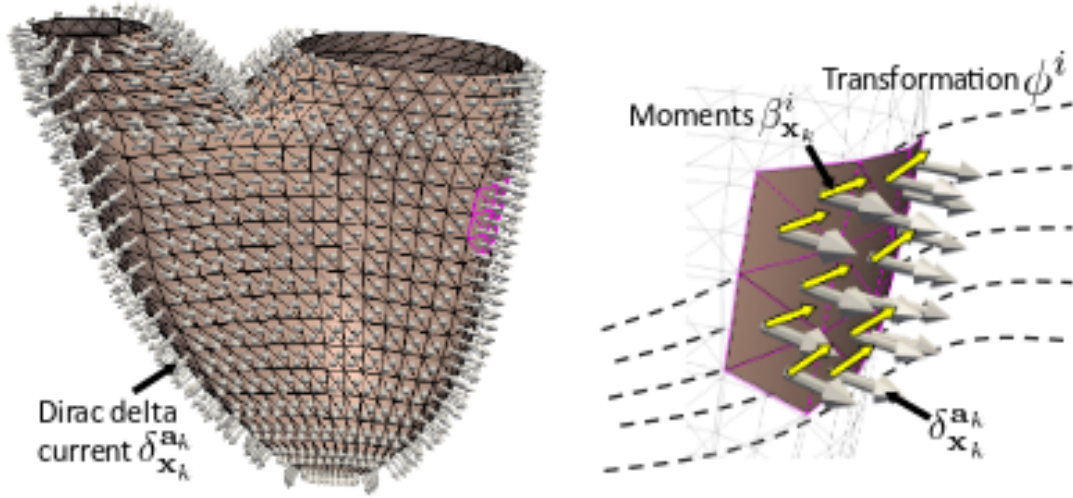


Figure 4.3: The Dirac currents of a triangulated mesh are positioned at the barycenter of every triangle and oriented along their normal. These momenta that parameterize the diffeomorphic deformation are defined at the barycenter. They are not necessarily normal to surface [Mansi et al., 2011].

parameterized by momenta, vectors that belong to a RKHS. This yields a diffeomorphism ϕ as well as a differentiable flow of the diffeomorphism ϕ_k for a continuous parameter k within the interval $[0, t]$. At time $k = 0$, we have the identity mapping ϕ_0 . The mapping at time t gives the desired transformation ϕ_t which we require for the atlas estimation. We can then define the path at any point x as $\phi_k(x)$ that leads to the final position $\phi_t(x)$. By following the path that passes through the point x , we can compute easily operations on diffeomorphisms, such as the inverse path from point t to 0. Using this framework, we minimize the difference between a deformed surface $\phi_t(S_1)$ and another surface S_2 , therefore finding the geodesic path from $\phi_t(S_1)$ to S_2 . The deformation ϕ_t is estimated by the minimization of a weighted sum of two terms: $\varepsilon(\phi) = d^2(\phi_t(S_1), S_2) + \lambda \int \|v_t\|^2$, the first term is the distance between surfaces (measured in the space of currents), and the second is the energy of the trajectory in the space of deformations, with conditions $\frac{\partial \phi_t(x)}{\partial t} = v_t(x)$, $\phi_0(x) = x$. The $v_t(x)$ are time-varying velocity fields parameterized by the initial velocity field $v_0(x)$, which belongs to a RKHS generated by a Gaussian kernel $K_V(x, y)$ [Guibert et al., 2013].

The reader is encouraged to refer to [Vaillant and Glaunès, 2005; Durrleman et al., 2009] for further details.

4.2.3.3 Implementation Using Deformetrica

The methodology is implemented in Deformetrica². First, we estimated an atlas of left atrial anatomic shape that was representative of the population under study using the software. During this process, control points $\{c_k\}_{k=1,\dots,N_{cp}}$ near the most variable parts of the atlas were placed automatically. Momenta $\vec{\alpha}$ associated with these points defined the deformation of the ambient 3D space towards each subject, and minimize the total error after registration [Durrleman *et al.*, 2014]. Then, we approximately deformed the atlas towards every subject.

There were two important parameters:

- Kernel width of the currents space λ_W , the larger, the more blurry the shape representation and fewer details.
- Kernel width of the velocity space λ_V , the larger, the less smooth/more rigid the transformations.

The deformation ϕ was estimated using the LDDMM on surface, characterized by initial velocity \vec{v}_0 . The velocity vector belongs to a Gaussian RKHS V with kernel K_V , and was weighted by a set of momenta $\vec{\alpha}_{c_k}$. $\{c_k\}_{k=1,\dots,N_{cp}}$ refers to the control points of deformation. At point x , the velocity is

$$v(x) = \sum_{k=1}^{N_{cp}} K_V(x, c_k) \vec{\alpha}_{c_k}. \quad (4.11)$$

In order to be independent of the surface orientation, the distance between surface meshes was defined based on Varifold metric [Charon and Trounev, 2013] as

$$d_W(S, S')^2 = \|S - S'\|_{W^*}^2 = \langle S, S \rangle_{W^*} + \langle S', S' \rangle_{W^*} - 2 \cdot \langle S, S' \rangle_{W^*} \quad (4.12a)$$

$$\text{with } \langle S, S' \rangle_{W^*} = \sum_p \sum_q K_W(c_p, c'_q) \frac{(n_p^T n'_q)^2}{|n_p^T| |n'_q|} \quad (4.12b)$$

where c (resp. c') refers to control points on surface S (resp. S') and n (resp. n') denotes normals related to controls points.

The line search strategy was used in the optimization process. Carefully testing of parameters is needed, including essentially the kernel width of the shape space, that of the deformation space, and the regularization factor λ . More details can be found in [Durrleman *et al.*, 2014].

²Open-access software developed by the Aramis Lab. Atlas estimation and registration have been integrated in the software <http://www.deformetrica.org/>

4.2.4 Extraction of Remodeling Information

We used methods in Sec. 4.2.3 to estimate an average shape in the population under study. Then, we warped the template to match each subject-specific shape. Deformations were parameterized as momenta $\vec{\alpha}_{c_k}$ attached to a same set of control points on the template for all patients. We use \mathbf{M}_i to represent the deformation momenta for patient $\#i$

$$\mathbf{M}_i = \left[\vec{\alpha}_{c_1}^i \quad \vec{\alpha}_{c_2}^i \quad \cdots \quad \vec{\alpha}_{c_k}^i \quad \cdots \quad \vec{\alpha}_{c_{N_{cp}}}^i \right]^T, \quad (4.13)$$

where $\vec{\alpha}_{c_k}^i = [\alpha_{c_k1}^i \quad \alpha_{c_k2}^i \quad \alpha_{c_k3}^i]^T$ is the deformation momenta associated with control point $\#k$ for patient $\#i$; N_{cp} is the total number of control points.

4.2.4.1 Whitening Transform

Then, we used whitening transform to express the deformation momenta in an orthonormal basis.

According to Eq. 4.11, the norm of the velocity vector for patient $\#i$

$$\|v^i\|^2 = \left[\vec{\alpha}_{c_1}^i \quad \vec{\alpha}_{c_2}^i \quad \cdots \quad \vec{\alpha}_{c_{N_{cp}}}^i \right] \mathbf{K} \left[\vec{\alpha}_{c_1}^i \quad \vec{\alpha}_{c_2}^i \quad \cdots \quad \vec{\alpha}_{c_{N_{cp}}}^i \right]^T = \mathbf{M}_i^T \mathbf{K} \mathbf{M}_i, \quad (4.14)$$

where \mathbf{K} is a positive definite matrix that defined a metric, with its blocks $K_{ij} = K_V(c_i, c_j) \otimes \mathbb{1}_3$. We used the Gaussian kernel $K_V(x, y) = \exp\left(\frac{-|x-y|^2}{\sigma_V^2}\right)$. Since the velocity vector v belongs to a RKHS space, the whitened momenta $\mathbf{K}^{1/2} \mathbf{M}_i$ belongs to the Euclidean space with L_2 norm. This allows us to apply seamlessly standard statistical methods like PLS.

We arranged the whitened deformation momenta $\mathbf{K}^{1/2} \mathbf{M}_i$ into a matrix as

$$\mathbf{A} = \left[\vec{\lambda}_1 \quad \vec{\lambda}_2 \quad \cdots \quad \vec{\lambda}_i \quad \cdots \quad \vec{\lambda}_{N_p} \right]^T, \quad (4.15)$$

where $\vec{\lambda}_i$ is a column vector that contains all the elements in $\mathbf{K}^{1/2} \mathbf{M}_i$; $N_p = 40$ is the total number of patient. Thus, the dimension of \mathbf{A} turns out to be $N_p \times (3N_{cp})$.

To sum up, modeling complex geometries with mathematical currents avoided using pre-defined markers and therefore has the potential to summarize any shape feature related to specific clinical factors. The finite-dimensional approximation of shape as deformation momenta was robust to detect subtle anatomical differences. Finally, the whitening transform reduced the correlation due to the kernel metric and constructed a L_2 space for statistical analysis.

4.2.5 Statistical Modeling

PLS regression combines PCA with linear regression by projecting inputs \mathbf{X} and \mathbf{Y} to a new space. \mathbf{X} is a $n \times m$ matrix of m predictors for n observations, and \mathbf{Y} is a $n \times w$ matrix of w response variables for n observations. It relates predictors

directly to response variables by finding multidimensional directions in X that explain the maximum variance in Y . Here, we use same notations as the tutorial [Geladi and Kowalski, 1986].

We chose PLS regression to find the principle dimensions in deformation parameters that correlate with post-ablation recurrence.

4.2.5.1 Dependency Analysis with Left Atrial Volume

In the first PLS regression, the whitened deformation parameters were considered as predictors, while the LAVI was considered as the response variable, as

$$\mathbf{X} = \mathbf{A} \quad \text{and} \quad Y = [LAVI_1 \quad LAVI_2 \quad \cdots \quad LAVI_i \quad \cdots \quad LAVI_{N_p}]^T,$$

where \mathbf{A} is defined in Eq. 4.15; $LAVI$ was calculated for each subject as $LAVI = V_{LA}/BSA$, based on the size of the atrium V_{LA} in units of mL and the body surface area BSA in units of m^2 .

According to the percentage of variance explained shown in Table 4.2, the first mode spanned an optimal subspace that explained 84.61% of LAVI variance for the population under study. It was expected that this principle mode of variation would be linked to volume change. To analyze shape features that are complementary to the atrial size, we subtracted, for every patient, the components in deformation projected on this mode, as

$$\mathbf{A}' = \mathbf{X} - \mathbf{T}(:, 1)\mathbf{P}(:, 1)^T, \quad (4.16)$$

where \mathbf{A}' is the matrix of volume-reduced deformation parameters; $\mathbf{T}(:, 1)$ is the first column of X score matrix \mathbf{T} ; $\mathbf{P}(:, 1)$ is the first column of X loading matrix \mathbf{P} , referring to the first PLS component of deformation related to LAVI.

We, therefore, created a new matrix of deformation parameters that reduced the components linearly related to left atrial volume change.

4.2.5.2 Correlation with Post-Ablation Recurrence

In the second PLS regression, we studied the correlation between atrial shape and post-ablation recurrence, using discriminant analysis, and leave-one-out prediction. The volume-reduced deformation parameters were considered as predictors, while the post-ablation outcome was considered as the response variable.

Here we illustrate the leave-one-out method. To predict the treatment outcome for patient $\#i$, PLS regression was performed among all the other patients as

$$\mathbf{X} = \mathbf{A}'([1 : i - 1, i + 1 : end], :) \quad (4.17)$$

$$Y = [R_1 \quad R_2 \quad \cdots \quad R_{i-1} \quad R_{i+1} \quad \cdots \quad R_{N_p}]^T, \quad (4.18)$$

where \mathbf{A}' was computed based on Eq. 4.16; R_i represents the post-ablation outcome for patient $\#i$, with $R_i = 1$ standing for with recurrence, $R_i = 0$ without recurrence.

Then, we projected the deformation parameters of patient $\#i$ on the subspace constructed by the first n PLS components, to calculate a predicted response for this new observation

$$Score_i = \mathbf{A}'(i, :) \mathbf{P}(:, 1:n) \mathbf{B}(1:n, 1:n) \mathbf{Q}(:, 1:n)^T, \quad (4.19)$$

where $\mathbf{A}'(i, :)$ is the volume-reduced deformation parameters for patient $\#i$; \mathbf{P} refers to the X loading matrix; \mathbf{B} is the diagonal matrix of coefficients b_h ; \mathbf{Q} is the Y loading matrix.

We repeated the leave-one-out regression and prediction for every patient, and thus obtained shape score $\{Score_i\}_{i=1,2,\dots,N_p}$ which qualified their potential for recurrence.

4.3 Materials

4.3.1 Data Preparation

4.3.1.1 Datasets

We worked in collaboration with clinicians from Bordeaux University Hospital, a leading center in the treatment of AF. They provided an existing database of 150+ multi-detector CT 3D images, along with clinical factors of patients including age, gender, type of arrhythmia, AF duration, the occurrence of stroke, RF duration/number of procedures to restore sinus rhythm, acute procedural endpoint, post-ablation recurrences.

4.3.1.2 Imaging Protocol

Contrast-enhanced cardiac CT was performed within 48 hours prior to ablation using dual-source CT scanners³ [Labarthe *et al.*, 2012]. Compared with previous literature [Bisbal *et al.*, 2013; Varela *et al.*, 2017; Biegging *et al.*, 2018], prospective ECG gating was applied to acquire data at end-systole, when left atrial motion is minimal, which is important for reducing the impact of heartbeat in shape modeling. An intravenous bolus of Iomeprol 400 mg I/mL (Bracco, Milan) at the rate of 5 mL/s was followed by a saline flush at the same rate to wash out contrast and prevent beam-hardening artifacts within the superior vena cava and right atrial chamber. A bolus tracking method was applied to acquire data with optimal left atrial enhancement. Contrast media volume differed between the two CT system and was adapted to patient morphology, as well as tube voltage and tube current. Temporal resolution was 66 *ms*. An intermediate level of iterative reconstruction and a soft tissue convolution filter were applied to reconstruct images at ventricular systole with axial sections of 0.5 mm thickness and typical in-plane pixel size of 0.4 * 0.4 *mm*. Mean X-ray exposure was 2.3 ± 1.0 *mSv*. The local research ethics committee approved the protocol of this study.

³(SOMATOM Definition or SOMATOM Force, Siemens.

4.3.1.3 Endocardium Segmentation

We segmented the left atrial endocardium from CT images using a region growing algorithm, as described in Sec. 2. After cropping and resampling, the voxel size of the CT images was $0.25 \times 0.25 \times 0.25 \text{ mm}^3$. The endocardium segmentation resulting from region-growing pipeline was post-processed, with alternating sequential filters (ASFs), pairs of idempotent morphological opening and closing filters.

4.3.2 Catheter Ablation

4.3.2.1 Ablation Procedure

Catheter ablations were performed without interruption of anticoagulant therapy, initiated at least 4 weeks before the procedure. Both radiofrequency ablation or cryotherapy methods could be applied. The use of contact force or electro-anatomical mapping systems was not mandatory in radiofrequency ablation. The left atrium was catheterized under fluoroscopic guidance by venous femoral access followed by a trans-septal puncture. Heparin anticoagulation adapted to the patient weight was dispensed. All patients underwent isolation of the four PVs. Complete isolation of PVs was defined by elimination or dissociation of PV potentials, as assessed using a Lasso catheter, which was the procedural endpoint in the paroxysmal AF. The complete block was systematically confirmed after adenosine injection to detect potential dormant conduction. In the persistent AF, the procedural endpoint was complete PV isolation and AF termination, and additional ablation could be performed after PV isolation on various targets. These could include linear lesions on the roof or mitral isthmus, focal ablation on areas exhibiting complex fractionated electro-grams on contact mapping, or focal ablation on regions exhibiting reentrant drivers on non-invasive electrocardiographic imaging. Catheter ablation of the cavotricuspid isthmus was performed in case of a history of atrial flutter. The radiofrequency and fluoroscopy duration and the total duration of the procedure were recorded.

4.3.2.2 Follow-up

Follow-up consisted of a short hospitalization with a physical examination, a 24-hour ECG, a stress test, and echocardiography. Patients were systematically reassessed 3 months after ablation. Then, paroxysmal AF patients were followed at 9 months and persistent AF patients at 6 and 12 months, earlier if symptomatic recurrence. Long-term follow-up could be done in our hospital or by the referring cardiologist. Management of anticoagulant and antiarrhythmic therapy was up to the discretion of the referring cardiologist. Arrhythmia recurrence was defined by one or more episodes of sustained atrial arrhythmia ($> 30\text{s}$), considering a blanking period of 3 months. In case of recurrence, one or more ablations could be proposed on a case-by-case basis. The assessment endpoint was a multi-procedural failure, i.e. arrhythmia recurrence since the last catheter ablation procedure. In patients undergoing multiple procedures, follow-up duration was computed from the date of the last ablation procedure.

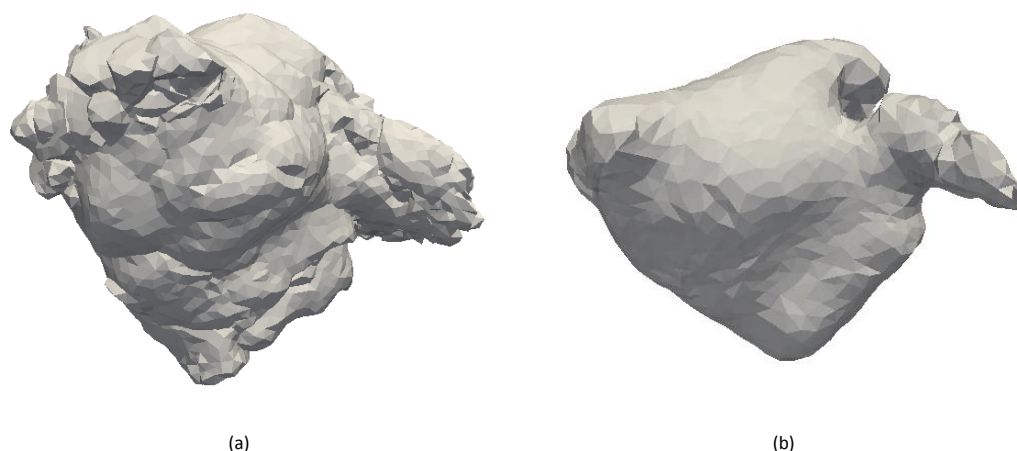


Figure 4.4: (a) A dozen of left atrial meshes from the population under study, as an illustration of the great difference of the left atrial shape that we can find among people; (b) atlas of the left atrium, which reflects an anatomic average within a dataset.

4.4 Preliminary Experiments in Paroxysmal Atrial Fibrillation

4.4.1 Population

40 paroxysmal AF patients were studied. They had no previous ablation at the time of imaging. The average age was 59 ± 11 years old, and 31/40 of the patients are male. Post-ablation recurrence within six months was observed in 13/40 patients. Meanwhile, we chose 24 control subjects without a significant difference in age or gender from the paroxysmal AF group.

4.4.2 Atlas of the Left Atrium

We show here the results of atlas computation and inter-subject registration, using methods described in Sec. 4.2.3.2. The morphology of the left atrium has a great variation among people. To study the shape, deformation pattern, and its relation with pathology, we generated a 3D atlas which represented an average anatomic model for the left atrium of this population, as shown in Fig. 4.4.

4.4.3 Diffeomorphic Registration

Then the template complex was warped to each subject's complex in a way that preserved the anatomic structures. No pre-defined landmark was needed to do the dif-



Figure 4.5: Comparison of a registration result and its target subject using LDDMM. Registration result in blue, target subject in gray.

feomorphic registration with Deformetrica. We compared the deformed atlas with the target subject and studied the error/distance in Fig. 4.5. The error, shown here as regions that do not overlap, is related to parameters chosen for the shape kernel λ_W and the deformation kernel λ_V during the registration process. While smaller parameters can bring more precise results, the computation time augments largely at the same time. In consequence, we chose reasonable kernel sizes to balance precision and computation efficiency, which revealed meaningful atrial deformation patterns. We chose $\lambda_W = 10$ and $\lambda_V = 10$.

4.4.4 Remodeling

The template offered a reference for anatomical invariant. Then, we warped this template towards each mesh of paroxysmal AF patients and calculated its deformation momenta. We illustrate the process in Fig. 4.6(a).

Kernel width parameters were set as Varifold kernel width $\sigma_W = 10 \text{ mm}$ and deformation kernel width $\sigma_V = 10 \text{ mm}$, ensuring respectively a suitable scale of shape variations and deformation to capture. $N_{cp} = 3952$ control points were placed near the most variable parts on the template and helped in representing shape differences between the template and the meshes of paroxysmal AF patients. With chosen parameters, atlas estimation and pairwise registration were performed efficiently with surfaces. The diffeomorphic registration generated a reasonable approximation of the left atrium of the target subject, as in Fig. 4.6(b).

We use the whitened momenta attached to a same set of controls points on the surface of the atlas to represent each left atrial shape.

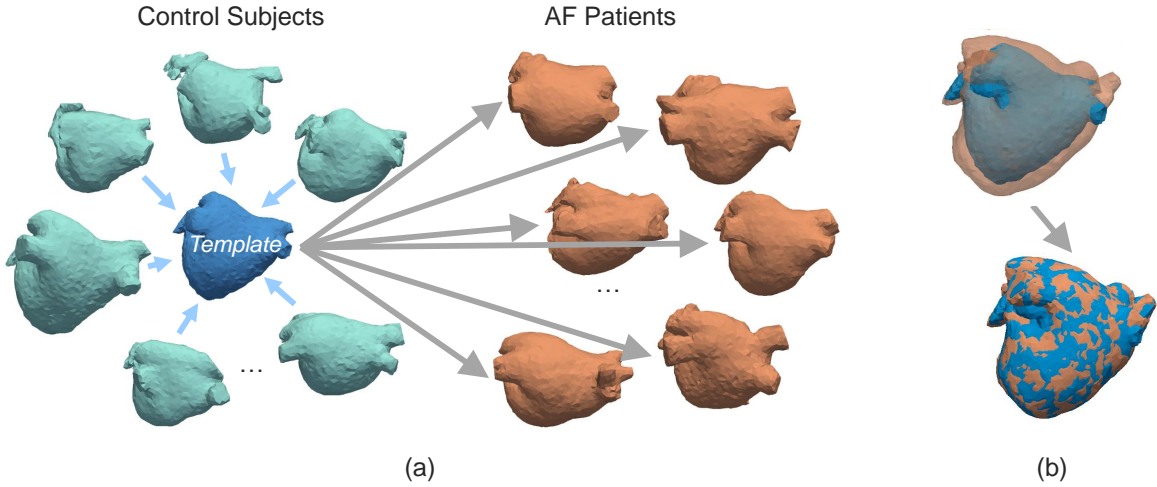


Figure 4.6: *Extraction of remodeling information vs. controls. (a) reference for atrial remodeling offered by control subjects; (b) the template in blue, before and after warping in a registration process toward the target in orange.*

Table 4.1: *Variations explained by the first 10 PCA modes of deformation.*

PCA Component	1 st	2 nd	3 rd	4 th	5 th
% of Variations	19.79	8.86	4.32	3.97	3.43
PCA Component	6 th	7 th	8 th	9 th	10 th
% of Variations	3.13	2.68	2.36	2.12	2.07

4.4.5 Principal Component Analysis

Here we present PCA results and analyze the first 5 modes of deformation in the control group. As shown in Fig. 4.7, +1 deformation results on the direction of the first 5 modes are compared with the atlas to identify the meaning of these 5 modes of deformation.

With 3D visualization, we can distinguish clearly these modes of deformation. For example, the 1st mode of deformation represents a change in volume. The 2nd, 3rd, and 4th represent the placement and the orientation of the four veins and the twisting of the surface.

Table 4.1 shows the variations explained by the first 10 modes of deformation.

From the variations explained, starting from the 5th mode, we can no longer use them as principal components of deformation, because noise may overlap with these modes only representing 2% to 3% of shape variations.

After performing PCA analysis of the sets of vector for all subjects, we obtained the most prominent deformation modes. A shape that is a standard-error (σ) distance away from the average shape on principal axes is a reasonable shape to be analyzed. Suppose that the left atrial shape in the population under study follows a multidimensional distribution, a shape that is a standard-error distance away from the average shape has a relatively high possibility to appear, even with increasing variable dimension. Hence,

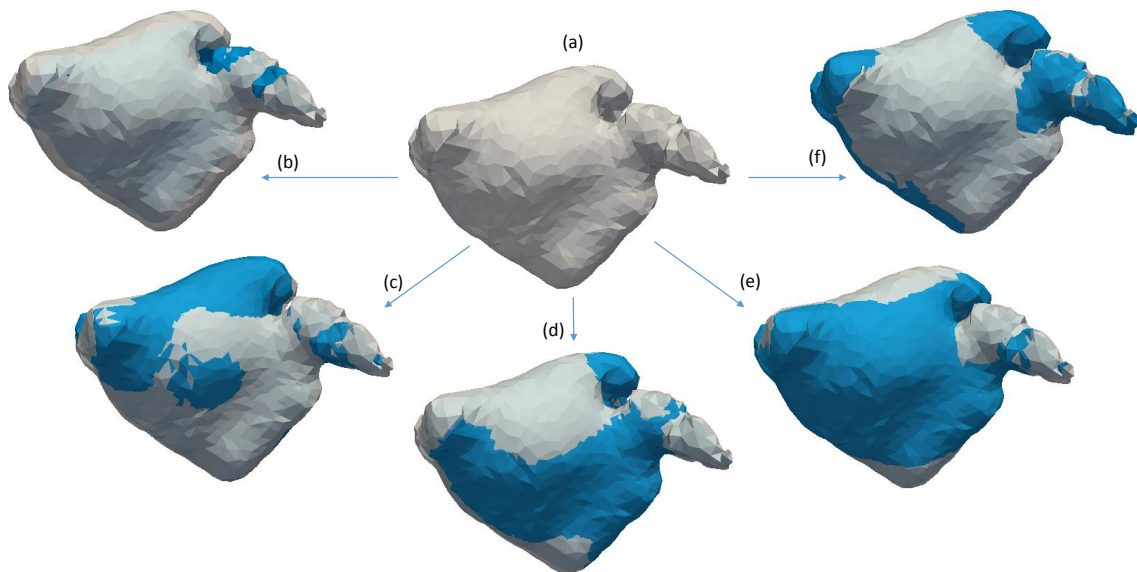


Figure 4.7: Atlas with $+\sigma$ deformation results on the direction of the first 5 modes. (a) Atlas; (b) Atlas in gray with the 1st mode of deformation in blue; (c) Atlas in gray with the 2nd mode of deformation in blue; (d) Atlas in gray with the 3rd mode of deformation in blue; (e) Atlas in gray with the 4th mode of deformation in blue; (f) Atlas in gray with the 5th mode of deformation in blue.

Table 4.2: Percentage of variance explained in the first partial least squares regression, for shape and left atrial volume index (LAVI) respectively.

PLS component	1 st	2 nd	3 rd	4 th	5 th
% of shape variance	53.45	7.09	7.50	4.47	5.70
% of LAVI variance	83.61	5.45	2.03	2.07	0.96

we use LDDMM shooting to calculate shapes of the left atrium after deformations of the atlas on each of the first 5 PCA modes that are a standard-error away from the atlas. We compared these shapes with the atlas to observe prominent deformation patterns.

We discovered that the most prominent shape variations of the left atrium were related to size, the orientation of veins, and the displacement of veins. The PCA analysis step serves as a foundation to analyze the database, to find patterns, which are useful for modeling, exploration of correlation, prediction of pathology. The next step of our work is to realize PLS analysis and do statistical modeling of the deformation, which we discuss with more details in the next sections.

4.4.6 Partial Least Squares Analysis

We present here the first three modes of deformation related to the recurrence in AF, with a higher signal-to-noise ratio, and their prediction capabilities. Beyond the

Table 4.3: Percentage of variance explained in the second partial least squares regression, for shape and post-ablation recurrence respectively.

PLS components	1 st	2 nd	3 rd	4 th	5 th
Percentage of shape variance %	21.44	9.02	14.30	9.71	5.69
Percentage of recurrence variance %	27.47	18.09	5.67	3.98	3.95

third mode, components may be dominated by noise since the percentage of variance explained by them was smaller than half of the gap between the percentages of variance explained by the previous two successive modes. The percentage of variance explained is shown in Table 4.3.

4.4.7 Principal Modes Related to Post-Ablation Recurrence

The principle modes of deformation related to post-ablation recurrence can be visualized and interpreted, shown in Fig. 4.8. Area strain [Kleijn *et al.*, 2011] and the magnitude of displacement were mapped onto meshes to illustrate subtle variations in deformations. To compute area strain, which is defined as the relative ratio of surface area change, we used the equation below, for each point p_k surrounded by n triangles $cell_{1,2,3\dots}$ on the surface mesh,

$$AS_k = \frac{\frac{(A_1 - A_1^T)}{A_1^T} + \frac{(A_2 - A_2^T)}{A_2^T} + \frac{(A_3 - A_3^T)}{A_3^T} + \dots}{n} \cdot 100\% \quad (4.20)$$

where T refers to a reference mesh, often the template; A refers to surface area (of cells).

For area strain, red indicates enlargement of triangular elements, while blue indicates shrinking. For displacement, regions in red deform with a larger scale of displacement than regions in blue.

Results show that the most dominant mode has an emphasis on regions underneath PVs, both with area strain and displacement of mesh elements. Clinical experts confirmed that this is one of the most complicated areas to ablate in PV isolation. Besides, the remodeling around PVs seems to be an essential aspect of AF. The second mode contains a twist of the upper-left part of the left atrium (from the posterior view, including roof, lateral, and anterior segments) and changes in orientation of PVs. The third mode, from less recurrence to more recurrence, reflects a slight change of roundness. These 3D deformation sequences can also be shown as videos to be better illustrated. The subtle regional variations need further interpretation.

4.4.8 Predictive Capabilities

We compared prediction capabilities of shape score with that of the classical clinical index LAVI, using the student's t-test and receiver operating characteristic (ROC) curves. The indices are shown in Table 4.4.

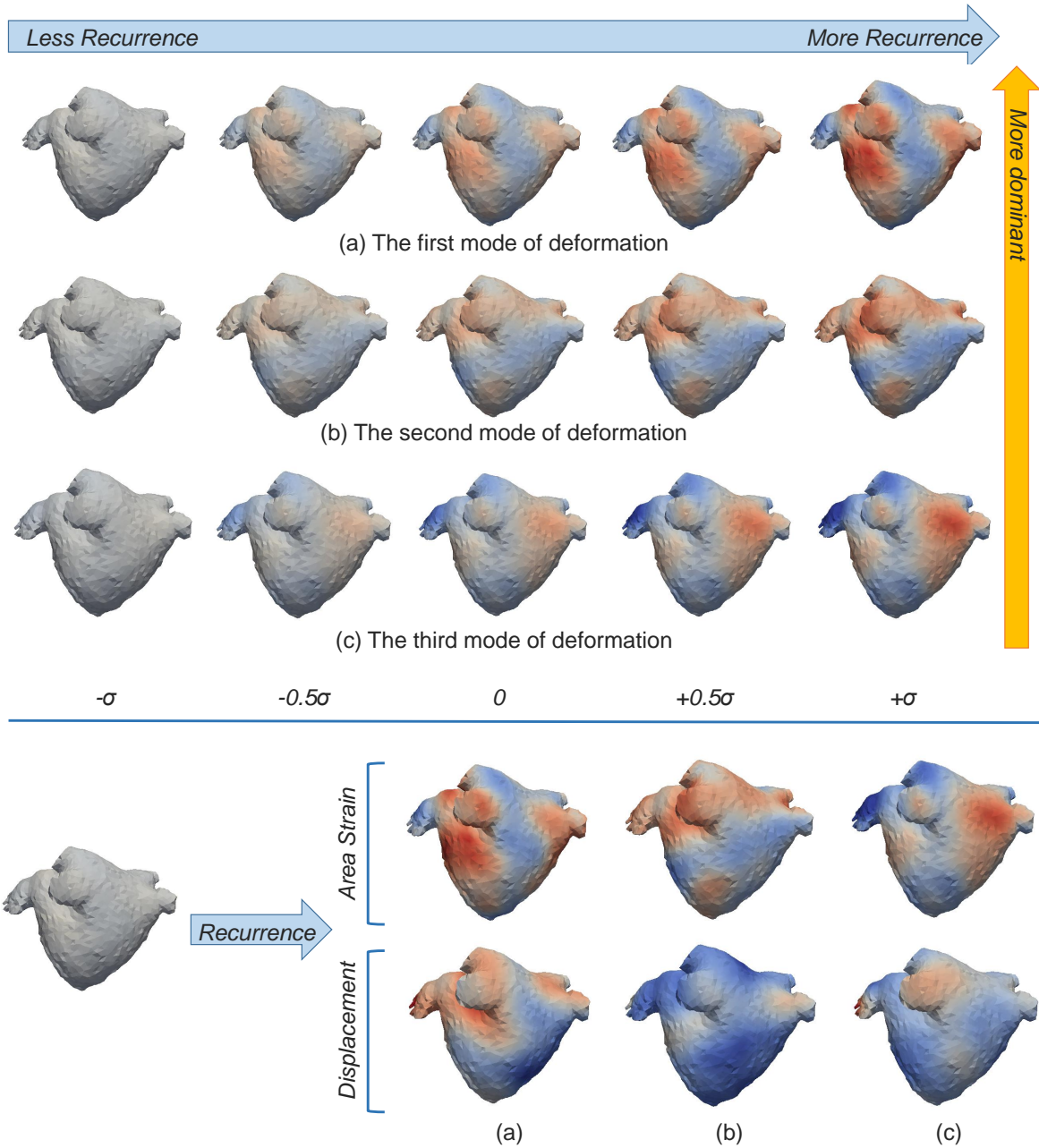


Figure 4.8: The first three modes of deformation involved in post-ablation recurrence. σ represents the standard derivation of each mode in the population. (top) the principal modes of deformation from less recurrence to more recurrence, where the color of meshes represents area strain. (bottom) the shape at σ on each principal axis, where the color illustrates area strain and displacement.

Table 4.4: Student's *t*-test to compare shape score and left atrial volume index (LAVI) in two sub-groups and area under receiver operating characteristic curves (AUC).

Paroxysmal AF patients	Non-recurrence	Recurrence	P-value	AUC
Score - 1 PLS component	0.28 ± 0.20	0.41 ± 0.23	0.04	0.65
Score - 2 PLS components	0.29 ± 0.22	0.48 ± 0.26	0.01	0.73
Score - 3 PLS components	0.30 ± 0.21	0.51 ± 0.34	0.01	0.70
LAVI mL/m_2	64.25 ± 19.34	64.97 ± 22.23	0.46	0.47

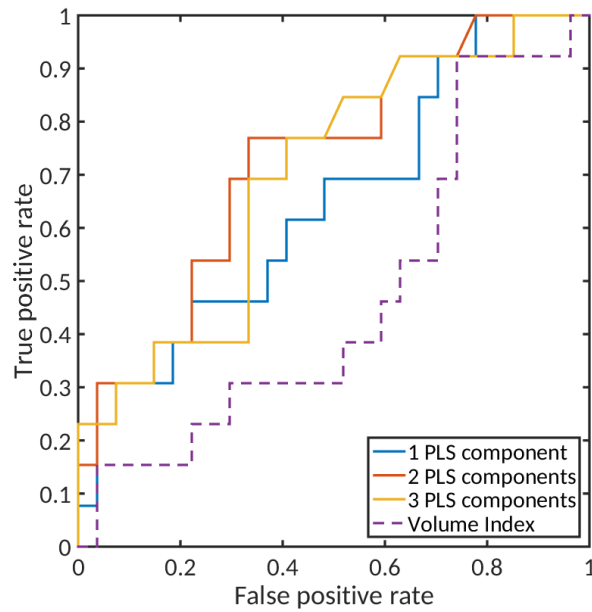


Figure 4.9: Receiver operating characteristic curves of 6-month post-ablation recurrence prediction.

- Shape score derived from PLS regression differed significantly between recurrence and non-recurrence groups, with p-value reaching $p = 0.01 < 0.05$ with the first two components, while LAVI did not, with $p = 0.46$.
- Shape score show a better classification performance as the discrimination threshold varies. We draw ROC curves of the shape score and the volume index in Fig. 4.9. The area under the ROC curve (AUC) using the first two components is 0.73, compared with 0.47 for LAVI.
- With discrimination threshold $t = 0.36$ for shape score with the first two components, we predicted recurrence with 0.77 sensitivity and 0.67 specificity.

From the differences, we can conclude that the shape analysis discovered extra anatomical features compared with the volume index for the understanding of post-ablation recurrence. Meanwhile, the principal modes of deformation revealed in this study turned out to be clinically meaningful.

4.5 Application on an Extended Database

Based on the promising results of the first experiments, the database was enlarged to validate the finding. We continue the study with the extended database, which not only includes subjects with paroxysmal AF, but also persistent AF, and long-standing persistent AF. I present the results in this section.

4.5.1 Population

158 patients referred for catheter ablation of atrial fibrillation were prospectively enrolled. The inclusion criterion was an indication for catheter ablation following current guidelines. Non-inclusion criteria included age < 18 years, dilated aortic root > 45 mm, pectus excavatum, history of catheter ablation, other percutaneous cardiac interventions or cardiac surgery, and intra-cardiac thrombus on CT.

At the time of inclusion, patients underwent a review of medical history, physical examination, laboratory assessment of cardiovascular risk factor, trans-thoracic echocardiography (TTE), and contrast-enhanced cardiac CT. Paroxysmal and persistent AF were distinguished according to the European Society of Cardiology criteria [Kirchhof *et al.*, 2016]. Mitral regurgitation was considered significant if higher than Grade 1 on TTE, and left ventricular dysfunction if left ventricular ejection fraction $< 45\%$ on TTE. The institutional review board approved the study, and all patients included provided informed consent.

17 patients were then excluded, 11 due to insufficient image quality, and 6 failure to obtain follow-up data.

4.5.2 Benchmarking Left Atrial Descriptors

We calculated atrial volumes, anteroposterior diameter, sphericity, and vertical asymmetry based on image processing results. The left atrium and LAA volumes (mL) were measured separately without PVs, indexed by body surface area (BSA) (m^2). The sphericity and the vertical asymmetry were measured according to previous studies [Bisbal *et al.*, 2018; Varela *et al.*, 2017]. The computation of the sphericity is slightly different from [Bisbal *et al.*, 2018], owing to the usage of detailed left atrial shapes instead of a sphere.

4.5.3 Inference Statistics and Multivariate Models

We studied the distribution and correlation of clinical characteristics, benchmarking left atrial descriptors, shape score, and catheter ablation outcome. Quantitative variables were expressed as either $mean \pm SD$ in case of normal distributions or median [interquartile range], according to the Shapiro-Wilk test of normality. We compared them using parametric (Student's t-test) or non-parametric (Mann-Whitney U-test) test, respectively; categorical variables were expressed as fractions (%). We compared them using Chi-squared or Fisher exact test. All statistical tests were two-tailed, and the significance level was 0.05.

Univariate and multivariate analyses investigated the relationship between predictors and catheter ablation outcomes. For quantitative variables, optimal cut-off values to categorize were obtained from ROC analysis. Multivariate analyses selected variables whose univariate analysis results follow the criteria of $p < 0.05$ for inclusion and $p > 0.10$ for removal, using a backward stepwise procedure. We estimated their odds ratio (OR), 95% confidence intervals (CI), and coefficients of determination (R^2) according to the Nagelkerke method.

Finally, probabilities of recurrence were estimated using a Bayesian decision tree, taking into account the most relevant predictors⁴.

4.5.4 Results

4.5.4.1 Univariate Predictability

Univariate analysis results are presented in this section. Among clinical characteristics, catheter ablation failure was found to relate to AF persistence ($p = 0.005$), alcohol abuse ($p = 0.033$), ischemic cardiomyopathy ($p = 0.047$), longer radiofrequency ($p = 0.03$), fluoroscopy ($p = 0.04$) and total procedure durations ($p = 0.01$), and additional lesions performed after PV isolation ($p = 0.028$). Among left atrial size-related metrics, catheter ablation failure related to increased LAVI ($p = 0.019$) and anteroposterior diameter ($p = 0.021$), but not to LAA volume. Among left atrial shape-related metrics, catheter ablation failure related to left atrial sphericity index ($p = 0.024$) and shape score ($p = 0.001$), but not to vertical asymmetry or the presence of common left trunk.

⁴SPSS 25.0 software, Chicago.

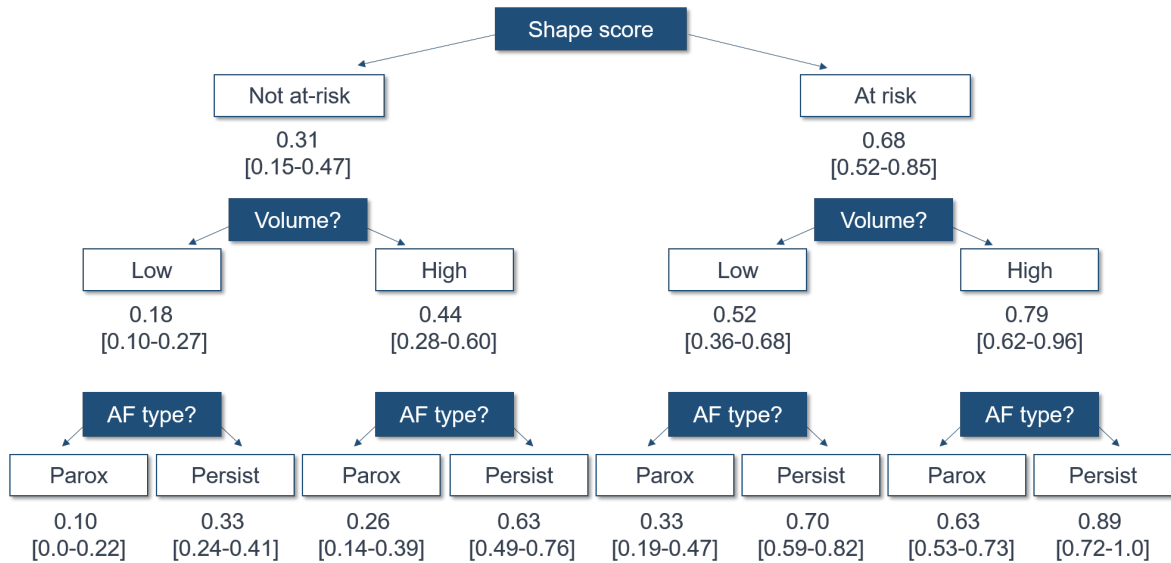


Figure 4.10: Bayesian Model of Catheter Ablation Response.

ROC analysis quantified their predictability: shape score (AUC = 0.7, 95% CI 0.61-0.79), followed by LAVI (AUC = 0.66, 95% CI 0.55-0.77), AF type (AUC = 0.64, 95% CI 0.43-0.75), left atrial sphericity (AUC = 0.63, 95% CI 0.52-0.74), and left atrial anteroposterior diameter (AUC = 0.62, 95% CI 0.51-0.74).

4.5.4.2 Probabilistic Predictive Modeling

We included in multivariate analysis the most significant clinical predictor (AF persistence), atrial size-related predictor (LA indexed volume), and atrial shape-related predictor (LA shape score) from univariate analysis. The shape score did not correlate with the other two predictors, while indexed left atrial volume and AF persistence were weakly correlated. Additionally, paroxysmal and persistent AF groups owned significant differences in terms of LAVI ($p = 0.001$), LAA volume ($p < 0.001$), and anteroposterior diameter ($p < 0.001$). The two AF groups had, conversely, week differences in terms of left atrial sphericity ($p = 0.051$), vertical asymmetry ($p = 0.87$), and shape score ($p = 0.55$).

We included the three indicators sequentially in a Bayesian decision tree to stratify the risk of ablation failure. Results are shown in Fig. 4.10. Persistent AF patients with shape score > 0.509 and LAVI $> 60.8 \text{ mL/m}^2$ showed 89% (72% - 100%) probability of ablation failure. Contrarily, paroxysmal AF patients with shape score < 0.509 and LAVI $< 60.8 \text{ mL/m}^2$ showed 10% (0% - 22%) probability of ablation failure.

4.5.5 Heterogeneous Regional Remodeling

We further analyzed local left atrial remodeling features to get a finer understanding of its link to arrhythmia recurrence. Previously we introduced the mapping of local left atrial surface area change compared with the average left atrial shape, which enabled

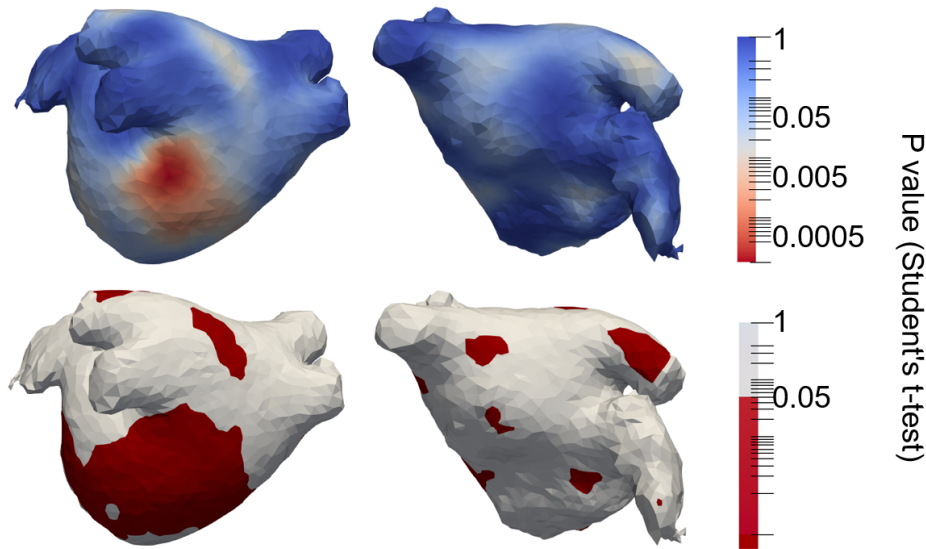


Figure 4.11: *Critical regions implicated in catheter ablation failure.*

detailed measurements of local remodeling in terms of surface area enlargement. We compared this feature locally between groups of patients with and without ablation failure using the Student t-test. Critical regions ($p < 0.05$) significantly associated with catheter ablation outcomes are displayed on the 3D template mesh in Fig. 4.11. They were mostly found on a large area extending from the inferior part of the posterior left atrium up to the mitral isthmus, covering left inferior PV. More focal differences laid close to the antrum of left and right superior veins, as well as within the septum and anterior wall. The local surface enlargement of these regions indicated the risk of arrhythmia recurrence.

Hypothesis Local remodeling was significantly larger in critical regions implicated in ablation failure. Our primary hypothesis is that these regions are more prone to structural or electrophysiological remodeling, which is indirectly taken into account when analyzing left atrial shape. This hypothesis is supported by the fact that the same regions were also found to be common sites for atrial fibrosis on MRI [Cochet *et al.*, 2015], low voltage on contact mapping [Cutler *et al.*, 2016], and re-entrant drivers during AF on electrocardiographic imaging [Haissaguerre *et al.*, 2014]. Consequently, these regions are usually targeted by most ablation strategies (PVs antral ablation, mitral isthmus line). The relation between shape features and atrial remodeling remains a going hypothesis and needs future work to conclude regarding AF pathophysiology.

4.6 Region Segmentation of Left Atrial Meshes

The left atrial shape is more complicated than the ventricles. To segment the meshes into different regions, the methods of finding the transverse section and an offset angle range used to define the left ventricular segments do not work in this case. Tak-

ing advantage of the point-to-point correspondence established during the registration process, we develop a package to segment automatically the left atrial meshes.

Because of the mechanism of LDDMM, we understand that the shape matching works between two shapes of the same topology. Thus, we classified the left atria first into two categories: the regular model, the common-left-trunk model.

Then, we label the triangles manually on the two template meshes, assigning to which regions they belong. With LDDMM, the label is automatically transported onto the rest of meshes, as the process illustrated in Fig. 4.12. More detailed region segmentation is performed and shown in Fig. 4.13

4.7 Discussions

In this chapter, we analyzed the shape of the left atrium within a population of controls and AF patients without previous ablation. As explained, the deformation, between group-wise average shape and a subject's shape, was used to quantify the specific left atrial shape for this subject. Diffeomorphisms parameterize deformation by initial momenta attached on the surface of the template. Quantifying anatomical variability based on diffeomorphism allows us to capture more delicate shape variations (greater than the kernel width) without the need for pre-defined markers. We controlled the momenta so that they were associated with the same set of control points. We worked with the LDDMM framework implemented in Deformetrica software to encode the subject-specific shape information. Last, statistical modeling was performed on momenta, normalized into space where basis vectors are orthogonal, to analyze the clinical problem of arrhythmia recurrence in AF.

4.7.1 Main Contributions

Performing comprehensive shape-based statistics on a large database of CT images acquired prior to catheter ablation, we have identified left atrial shape score carrying additional prognostic and predictive value for arrhythmia recurrence.

Compared with previous literature, prospective ECG gating was applied to acquire data at end-systole, when left atrial motion is minimal, which is vital for reducing the impact of heartbeat in shape modeling.

The limited size of datasets has been an obstacle to medical image analysis. In this study, we were able to perform statistical analysis in a 150+ AF population, with different types of AF, and clinical factors for each subject, including age, BSA, and post-ablation recurrences.

Combining the shape score, LAVI, and AF persistence in a multivariate model allows stratifying recurrence risk on a patient-by-patient basis. The shape score, derived from two-step PLS regression, was not correlated with clinically available predictors and outperforms reported shape markers. From the differences of AUC in PLS analysis, we can conclude that the shape analysis discovered extra anatomical features compared with the volume index for the understanding of post-ablation recurrence. Meanwhile,

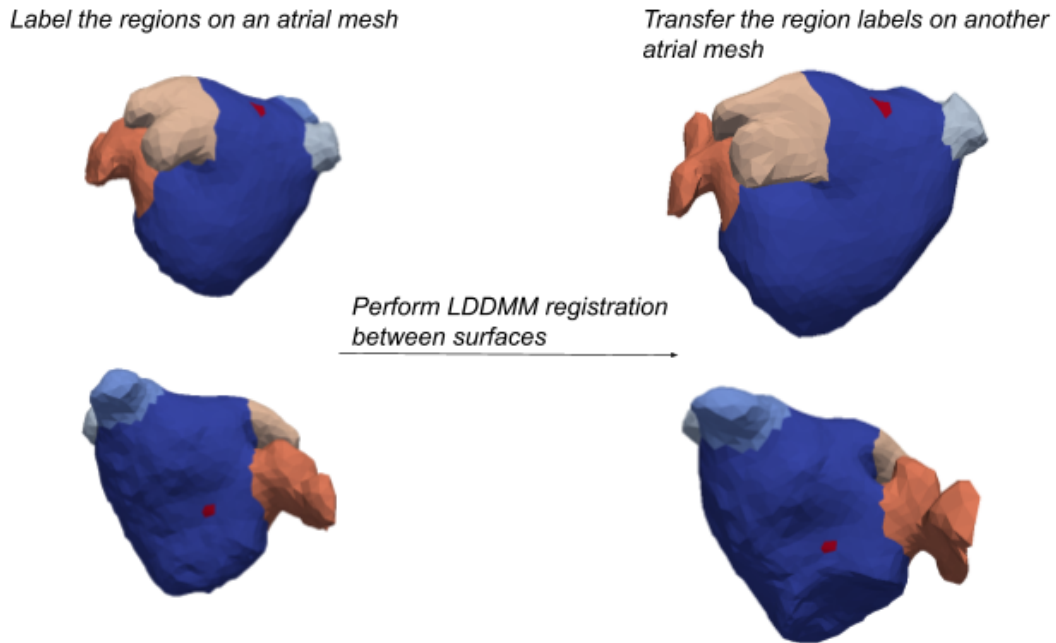


Figure 4.12: *Efficient left atrial region labeling I: automatically transferring region labels on the template to another mesh through diffeomorphic registration. PVs (common left trunk, yellow and right PVs, light blue), appendage (orange), and body (dark blue). The red triangular cells are at the center of the anterior wall and posterior wall, used to compute the anteroposterior diameter of the left atrium.*

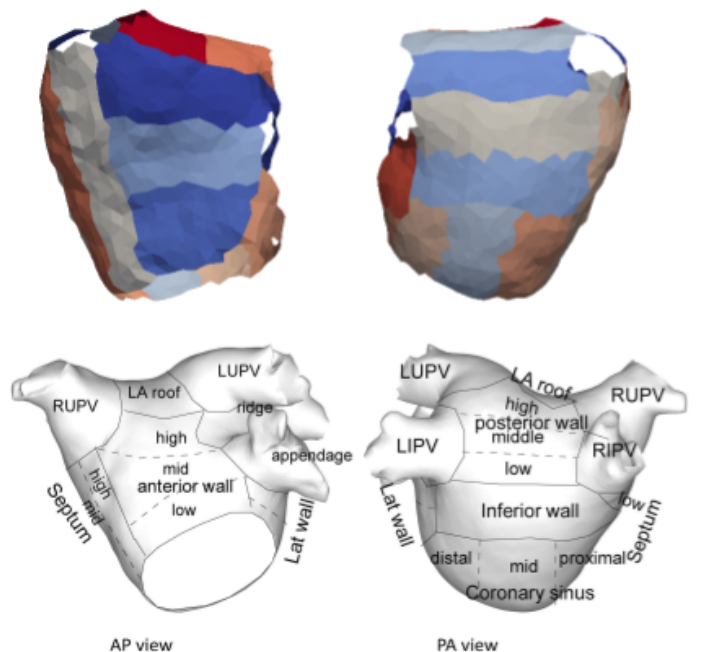


Figure 4.13: *Efficient left atrial region labeling II: more detailed anatomic divisions of the left atrium (top), according to a 22-segment model of the left atrium (bottom) [Hunter et al., 2011, 2012].*

the principal modes of deformation that were related to a higher post-ablation recurrence risk revealed in this study turned out to be clinically meaningful.

From a clinical viewpoint, some anatomical details were consistent with the complexity of ablation in clinical practice. Results show that the most dominant mode has an emphasis on regions underneath PVs, both with area strain and displacement of mesh elements. Clinical experts confirmed that this is one of the most complicated areas to ablate in PV isolation. These features also bring new insights on how a left atrial shape evolves during remodeling, apart from volume change.

The assessment is potentially related to an asymmetric and heterogeneous regional remodeling process. We found that critical regions whose local remodeling closely associated with ablation failure included a vast area covering the inferior part of the posterior left atrium, the left inferior PV, and the mitral isthmus. Smaller areas resided on the antrum of left and right superior veins, the septum and the anterior wall.

The adverse structural findings, both global and regional, could lead to potential ablation targets outside PVs for treatment planning.

We also developed a package for region segmentation on left atrial meshes. Considering the specific characteristic shape features of the left atrium, we devised a framework to transfer region labels with the LDDMM algorithm, which performed efficiently in identifying different regions and establishing correspondence on meshes automatically.

4.7.2 Limitations and Future Work

To understand the physiological meaning of the features found in the retrospective population-based studies, we need to future investigate atrial physiology. Some questions arose about the underlying causality of AF and its associated consequences (stroke, heart failure), which cannot be answered by statistical shape analysis.

Future work also includes combining shape variations with other factors, such as age, sex, and electrocardiography, to stratify the risk of recurrence.

In the next chapter, we study, not the static heart shape, but the temporal deformation of the heart, towards statistical modeling of the cardiac motion in the cardiac cycle.

"Blessed are the hearts that can bend; they shall never be broken."

— Albert Camus

CHAPTER 5

Deformation Analysis

The cardiac motion contains information underlying disease development and complements the anatomical information extracted for each subject. However, normalization of temporal trajectories is necessary due to anatomical differences between subjects. This chapter extends the work on statistical shape analysis to deformation analysis.

We encode inter-subject shape variations and temporal deformations in common spaces of diffeomorphic registration. Previous normalization algorithms applied in medical imaging were first-order approximations of parallel transport. In contrast, the pole ladder was recently shown to be a third-order scheme in general affine connection spaces and exact in one step in affine symmetric spaces. We further improve this procedure with a more symmetric mapping scheme, which relies on geodesic symmetries around mid-points. Besides, we propose a continuum of decompositions of the space of diffeomorphisms, which approximates better a symmetric space by taking into account the residuals in registration.

We apply the method to analyze cardiac motion among pulmonary hypertension populations. Evaluation is performed on a 4D cardiac database, with meshes of the right ventricle obtained from echo-cardiogram. We assess the stability of the algorithms by computing their numerical inverse error and other properties of symmetric spaces. Our method turns out to be very accurate and sufficient in terms of cardiac function transport.

Part of this chapter is based on the following scientific articles:

1. Jia S, Duchateau N, Mocerri P, Sermesant M, Pennec X. Parallel transport of surface deformations from pole ladder to symmetrical extension. In International Workshop on Shape in Medical Imaging 2018;116-124. Held in conjunction with MICCAI [*Jia et al.*, 2018b].
2. Guigui N, Jia S, Sermesant M, Pennec X. Symmetric Algorithmic Components for Shape Analysis with Diffeomorphisms. In Geometric Science of Information 2019 [*Guigui et al.*, 2019].

Contents

5.1	Background	78
5.2	Methodology	80
5.2.1	Pole Ladder	80
5.2.2	Numerical Accuracy	80
5.2.3	LDDMM-Based Transport	82
5.2.4	SVF-Based Transport	83
5.2.5	Benchmark Transport Algorithm	83
5.3	Experiments	84
5.3.1	Materials	84
5.3.2	Template Estimation and Registration	84
5.3.3	Consistency	85
5.3.4	Strain Analysis	85
5.3.5	Statistical Modeling of Cardiac Deformation	88
5.3.5.1	Modes	88
5.3.5.2	Compactness	88
5.4	Algorithmic Improvement for Riemannian Geodesics	90
5.4.1	Decomposition with Deformation and Residual	90
5.4.2	Formulations Accounting for Residuals	90
5.4.2.1	Formulation of Midpoint with Residuals	91
5.4.2.2	Formulation of Symmetry with Residuals	91
5.4.3	Affine Symmetric Space	92
5.4.4	Types of Errors	92
5.4.5	Decomposition Continuum	93
5.4.6	Results	95
5.5	Discussions	95
5.5.1	Limitations	95
5.5.2	Main Contributions	97
5.5.3	Future Work	98

5.1 Background

Analyzing cardiac function, notably myocardial deformation along the cardiac cycle, can reveal subtle changes underlying disease development, and therefore improve risk stratification for patients. Nevertheless, it is a challenging task to construct a robust method for the normalization of temporal deformations, both theoretically and numerically. Transporting the temporal deformations from a subject’s anatomy to another one (or to a template) is more complicated than resampling a scalar function because some reorientation is needed. The choice of a normalization method may affect the following analysis in terms of accuracy and reliability to characterize diseases.

In this context, we assume that 3D anatomical heart models are provided from image segmentation or speckle-tracking, and we start from investigating how to normalize the transformations of surface meshes. Diverse non-rigid registration algorithms

may be suitable in different scenarios depending on the characteristics of the shapes. We hypothesize that cardiac shape variations and temporal deformations can be more faithfully modeled in the space of diffeomorphic transformations, flows of velocity fields, which are parameterized by their initial values.

Previous studies used conjugate action given its relative simplicity. It consists of assuming a stationary change of coordinates between anatomies thanks to which we can compute a local reorientation of myocardial velocities [Duchateau *et al.*, 2011; Bai *et al.*, 2015].

In differential geometry, parallel transport specifies how to realize an infinitesimal transformation (a tangent vector) along a curve from one point to another of a manifold, as illustrated in Fig. 5.1(left). The notion was introduced in medical imaging by [Younes, 2007] for the large deformation diffeomorphic metric mapping (LDDMM) framework and used for neuroimaging studies in [Qiu *et al.*, 2008]. A fanning scheme for parallel transport using iterative local approximation with Jacobi fields was proposed in [Louis *et al.*, 2017]. These methods are first-order approximation schemes, which need to be iterated along the curve.

[Lorenzi *et al.*, 2011; Lorenzi and Pennec, 2014] later proposed more simple discrete numerical schemes called Schild’s and pole ladders, in the stationary velocity fields (SVFs) [Vercauteren *et al.*, 2008] framework (constant velocity field during the integration, hence the name SVFs). Because they are only based on geodesics, they can be easily implemented using registration algorithms. The pole ladder is particularly interesting because it realizes the exact parallel transport in symmetric spaces in only one step (for instance, with SVFs), and was recently discovered to be of third-order in general affine connection spaces [Pennec, 2018]. So far, these schemes were mainly used to model brain deformations in neuroimaging. In terms of application, these neuroimaging studies often consist of few samples along a very smooth longitudinal trajectory, while the spatiotemporal analysis of cardiac sequences encompasses uniformly sampled instants with higher variations in duration and relative timing of physiological events.

To apply parallel transport to cardiac sequences, we need to:

- Parameterize the temporal deformations Φ_{t_i} from the subject-specific shape S at baseline to its shape S'_{t_i} at time t_i by SVF v_{t_i} ; this step amounts to computing the logarithm of the deformations such that $\Phi_{t_i} = \exp(v_{t_i})$, or to register S to S'_{t_i} .
- Transfer these SVFs along the inter-subject deformation geodesic Φ_S from the space of S to a common geometry T , often called a template.

These steps lead to a representation of all the subject-specific deformations as infinitesimal deformations of the same anatomy. We can thus perform proper population comparison in terms of shape evolution along the cardiac cycle, as shown in Fig. 5.1(right).

Despite that the definition of logarithm may be well developed in theory, implementations of its computation could be unstable due to numerical inconsistency. When computing registration/geodesics, the logarithms of surface deformations are

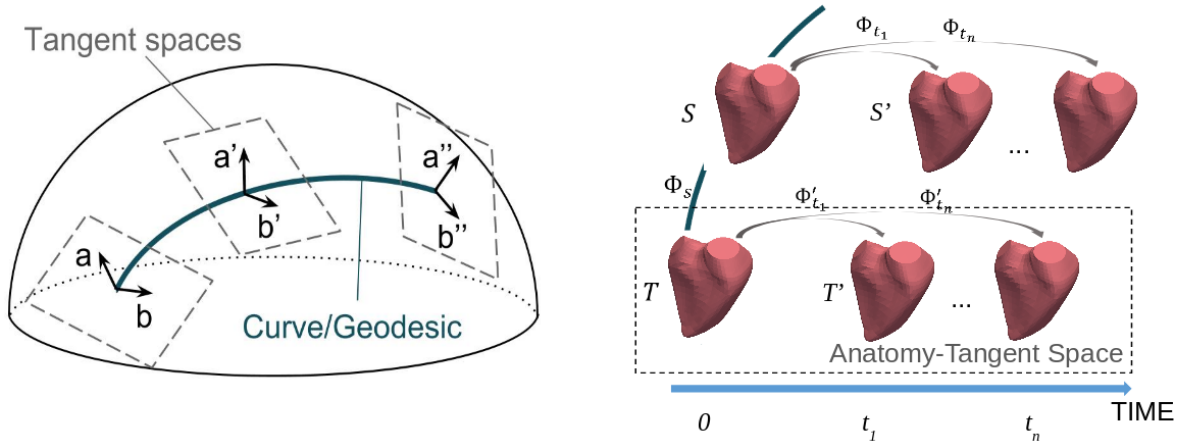


Figure 5.1: Illustration of parallel transport of vectors a and b along a curve (left) and the application of parallel transport in cardiac motion analysis focusing on surface meshes (right).

only sparsely defined in the space (on the shape), which differs from image deformations. Careful numerical implementation of parallel transport algorithms is also needed.

5.2 Methodology

5.2.1 Pole Ladder

The pole ladder is based on using the curve as the diagonal of the geodesic parallelogram to realize parallel transport (see Fig 5.2 and Algo. 1). Let u be the initial tangent vector to the geodesic segment that encodes the temporal deformation $\exp_S(tu)$ ($t \in [0, 1]$). Originally, the pole ladder computes a midpoint on the geodesic $[S, T]$ and expands twice the geodesic from the endpoint S' to the midpoint to obtain the point T'' .

We propose to reformulate the doubling of the geodesics with a mid-point geodesic symmetry (Algo. 2). The mid-point M of a geodesic segment $[S, T]$ is defined as $M = \gamma_{[S, T]}(\frac{1}{2})$. The mappings from M towards the two sides meet the definition of a geodesic symmetry: $\gamma_{[M, S]}(t) = -\gamma_{[M, T]}(t)$. Although this new version of the pole ladder is theoretically equivalent to the previous one, it is numerically more stable in our experiments. This may be emphasized by the fact that in medical imaging, we are encoding tangent vectors with infinitesimal deformations and that changing the object which is deformed may have a drastic numerical impact.

5.2.2 Numerical Accuracy

Recent mathematical developments have enabled the numerical analysis of the pole ladder in affine connection spaces with symmetric connections [Pennec, 2018]. In Lie groups, the Baker-Campbell-Hausdorff (BCH) formula provides an expansion of the

Algorithm 1: Pole ladder transport of the vector u along the geodesic $[S, T]$

Condition: S, T, S' are in a sufficiently small convex neighborhood on the geodesic curve.

- Compute the midpoint $M = \exp_S(\frac{1}{2} \log_S(T))$ on the intersubject geodesic;
 - Compute the geodesic from the endpoint $S' = \exp_S(u)$ of the temporal geodesic segment to the midpoint M , and shoot twice to get the inverse endpoint: $T'' = \exp_{S'}(2 \log_{S'}(M))$;
 - Return the vector $trans(u) = -\log_T(T'')$ and then apply it to T : $T' = \exp_T(trans(u))$.
-

composition of two group exponentials in the Lie algebra: $BCH(v, u) = \log(\exp(v) \circ \exp(u))$. This formula has been thoroughly used in registration algorithms [Bossa et al., 2007]. In general affine connection manifolds, a somewhat similar formula can be established based on the curvature instead of the Lie bracket [Gavrilov, 2006]. The double exponential $\exp_x(v, u) = \exp_y(\Pi_x^y u)$ corresponds to a first geodesic shooting from the point x along the vector v , followed by a second geodesic shooting from $y = \exp_x(v)$ along the parallel transport $\Pi_x^y u$ of the vector u . [Gavrilov, 2006] has shown that the Taylor expansion of the log of this endpoint $h_x(v, u) = \log_x(\exp_x(v, u))$ is:

$$h_x(v, u) = v + u + \frac{1}{6}R(u, v)v + \frac{1}{3}R(v, u)u + \frac{1}{12}\nabla_v R(u, v)v + \frac{1}{24}(\nabla_u R)(u, v)v + \frac{5}{24}(\nabla_v R)(u, v)u + \frac{1}{12}(\nabla_u R)(u, v)u + O(\|u + v\|^5). \quad (5.1)$$

When applied to our reformulation of the pole ladder using geodesic symmetry, we find that the error on one step of the pole ladder to transport the vector u along a geodesic segment of tangent vector $[S, T] = [\exp_M(-v), \exp_M(v)]$ (all quantities being parallel translated at the mid-point M) is:

$$\Pi_T^M trans(u) - \Pi_S^M u = \frac{1}{12} ((\nabla_v R)(u, v)(5u - 2v) + (\nabla_u R)(u, v)(v - 2u)) + O(\|v + u\|^5). \quad (5.2)$$

Algorithm 2: Mid-point symmetric pole ladder transport of the geodesic segment $[S, S']$ along the geodesic $[S, T]$

Condition: S, T, S' are in a sufficiently small convex neighborhood on the geodesic curve.

- Compute the midpoint $M = \gamma_{[S, T]}(\frac{1}{2})$ on the intersubject geodesic;
 - Compute the symmetric point $T'' = \exp_M(-\log_M(S'))$ of S' with respect to M ;
 - Compute the symmetric point $T' = \exp_T(-\log_T(T''))$ of T'' with respect to T , and return the geodesic segment $[T, T']$.
-

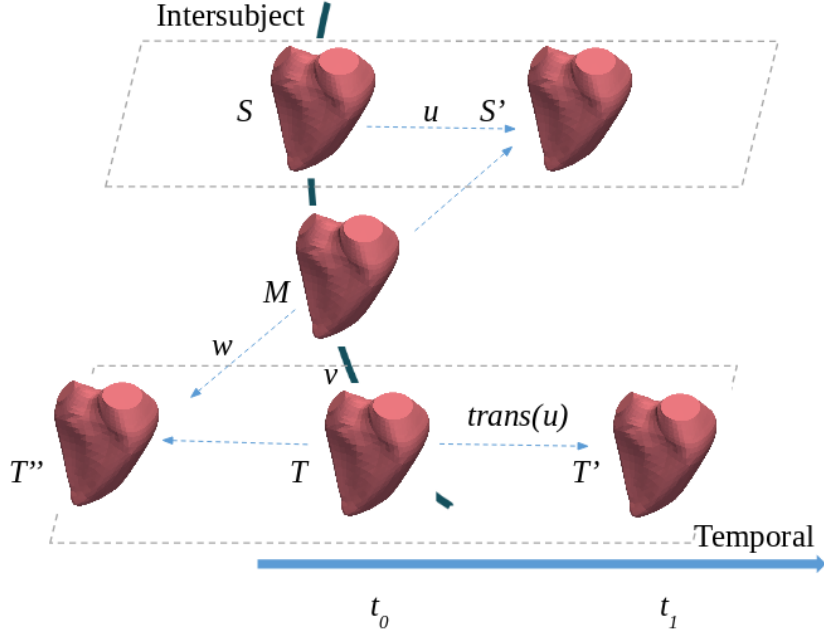


Figure 5.2: The proposed symmetry-based reformulation of the pole ladder structure.

We see here that one single step of the pole ladder is of order three, thus much more accurate than the other first-order parallel transport schemes. Moreover, the fourth-order error term vanishes in affine symmetric spaces since the curvature is covariantly constant in these spaces. In fact, one can prove that all error terms vanish in a convex normal neighborhood of an affine connection space: one step of the pole ladder realizes an exact parallel transport (provided that geodesics and mid-points are computed precisely of course) [Pennec, 2018]. This result makes the pole ladder a very attractive scheme. In particular, Lie groups have a canonical symmetric space structure thanks to the symmetry $s_g(h) = gh^{-1}g$ for any elements g, h of the Lie group. This is an affine structure that is generally not metric. The symmetry generates a canonical connection, which is exactly the symmetric Cartan-Schouten connection. Since the geodesics of this connection going through identity are parameterized the flow of SVFs, we can conclude that the pole ladder on SVFs is exact, at least theoretically.

5.2.3 LDDMM-Based Transport

We presented the LDDMM framework in the previous chapter. Flows of instantaneous velocity fields parameterize diffeomorphisms by a set of initial vectors momentum α_0 at discrete initial positions of control points c_0 , whose convolution with the transformation kernel specifies the Riemannian log of the transformation [Durrleman et al., 2014]. The trajectory of control points and time-varying momentum vectors follows the path that minimizes kinetic energy to reach the given deformation.

We performed careful parameter-testing for LDDMM registration to achieve satisfying shape matching. In particular, the current-based representation of shapes resulted

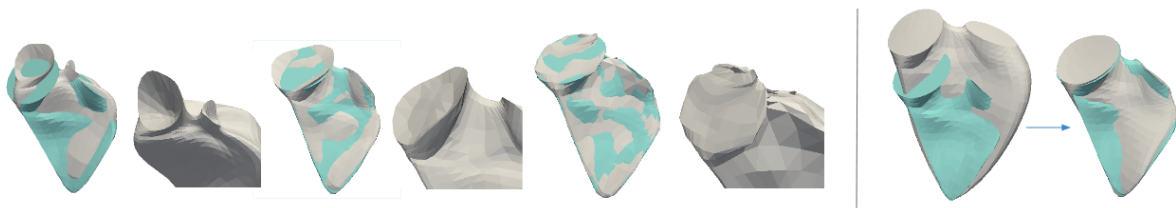


Figure 5.3: Artifacts (left) to avoid in registration due to inappropriate kernel size and shape representation, compared with (right) a registration with chosen parameters.

in artifacts located mainly at the ostia closure. We, therefore, opted for a landmark-based or a Varifold-based representation of the shapes. We finetuned the kernel widths and minimized errors in registration, to avoid amplifying defects during transport. Some artifacts caused due to inappropriate parameter settings during the parameter-testing phase are shown in Fig. 5.3.

For LDDMM, there is no explicit logarithm computation for a combination of transformations. The pole ladder builds a geodesic parallelogram using the symmetry structure. We define symmetry as shooting from the same point by flows of velocity fields defined by initial momenta of opposite sign.

5.2.4 SVF-Based Transport

In practice, we consider sparse point-to-point correspondences between two shapes (established here with the commercial speckle-tracking software) to compute diffeomorphic transformation. Thus, the solution for the log is not unique and needs to be spatially regularized. Following [Rohé et al., 2017], the sparse displacement field on the mesh vertices is interpolated to a dense image grid using a standard thin-plate spline (TPS) kernel (stiffness of zero) [Davis et al., 1997]. The TPS is a smoothing spline with parameters defining how resistant the surfaces are to bending. Then, a symmetric iterative procedure computes a SVF explicitly from the displacement field using the BCH formula. The result gives a smooth SVF that linearly extends outside the grid borders, as illustrated in Fig. 5.4.

The SVFs for temporal and intrasubject transformations are then used to compute the transported SVF to the template space using our symmetric pole ladder transport.

Remarks. The detailed shape variability lost during the registration process cannot be transported. That is the reason why we report fiducial localization error due to shape registration in Sec 5.3.

5.2.5 Benchmark Transport Algorithm

Simple transport, conjugate action, which has been tested for cardiac motion analysis [Duchateau et al., 2011; Bai et al., 2015], serves as a benchmark. The conjugate action of two transformations is defined as $Conj_{\Phi_s}(\Phi_t) = \Phi_s \Phi_t \Phi_s^{-1}$. Numerically, it can be

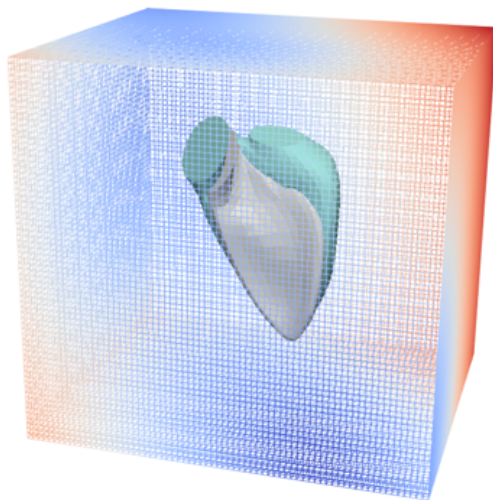


Figure 5.4: *Illustration of stationary velocity field computation for surface matching.*

computed as the solution of $\exp(\text{trans}(v_t)) = \exp(v_s) \exp(v_t) \exp(-v_s)$ in the SVF setting using iterated BCH formulas.

5.3 Experiments

We assess the SVF and LDDMM parallel transport of subjects end-diastole-end-systole (ED-ES) deformations to the template according to two criteria (i) the mesh consistency after forward transport to the template and backward to the subject along inter-subject trajectory; and (ii) the changes they induce on myocardial deformation (global and local strain) modeled between end-diastole and end-systole.

5.3.1 Materials

For evaluation, we used a 4D cardiac mesh database of right-ventricular meshes in 138 subjects. The population includes 34 healthy subjects, and 104 subjects with pulmonary hypertension, which are divided into three classes according to the severity of the disease (New York Heart Association - NYHA, classes II, III and IV). The motion of the myocardium was given by point-to-point correspondences from commercial speckle-tracking of the right-ventricular from 3D trans-thoracic echocardiography¹. For the acquisition of images, please refer to [Moceri *et al.*, 2017].

5.3.2 Template Estimation and Registration

The meshes were spatially aligned at baseline time, end-diastole, using rigid deformations with the iterative closest point algorithm. Then for meshes of different instants

¹Commercial speckle-tracking by 4D RV Function 2.0 software, TomTec Imaging Systems GmbH, Germany

Table 5.1: Numerical consistency of parallel transports. Fiducial localization error (FLE) due to shape registration (left) and to forward/backward transport (right) ($\mu \pm \sigma$ in mm).

Registration error (FLE)			
SVF		LDDMM	
0.15 \pm 0.15		0.59 \pm 0.17	
Inverse Transport			
Pole Ladder SVF	Pole Ladder LDDMM	ConjAction SVF	ConjAction LDDMM
0.12 \pm 0.10	1.32 \pm 0.43	0.22 \pm 0.12	1.57 \pm 0.76

but belonging to one subject, we preserved their relative position between cardiac sequences by applying to them the same rigid deformation. A template was built at baseline time end-diastole as a mean shape in the healthy group using point distribution model.

Then we compute the deformation from each subject’s shape at end-diastole towards the template. The middle point on this geodesic serves as the midpoint for the two symmetric mappings in the pole ladder to transport temporal deformations, $[M, S']$, $[M, T'']$ and $[T, T'']$, $[T, T']$, as shown in Fig 5.2. The computation of SVFs is implemented in C++. The computation of LDDMM momenta uses the Deformetrica Software.

5.3.3 Consistency

Inverse consistency was tested by transporting the velocity field corresponding to the ED-ES deformation forward along the geodesic encoding the subject-specific right-ventricular shape changes with respect to the template at end-diastole, and then backward along the reverse geodesic. If the numerical implementation is accurate, the result of the inverse transport should be exactly the original vector.

Consistency was quantified by the error between the final warped end-systole shape and the original subject’s end-systole shape (Table 5.1). The errors should be compared to the mismatch of each registration method (fiducial localization error of vertices). We can see that SVF pole ladder transport was very consistent while LDDMM pole ladder multiplied the registration error by 2. Conjugation was in all cases less reproducible.

5.3.4 Strain Analysis

We also evaluated the different parallel transports schemes according to the changes they induced on area strain, a local cardiac function parameter defined as the deformation of each surface cell from end-diastole to end-systole. This feature is commonly used by clinicians to characterize the cardiac motion [Kleijn *et al.*, 2011]. The local cardiac feature provides valuable information regarding cardiac function. In particular,

right-ventricular area strain has been related to patient clinical condition and survival in this type of population [Moceri *et al.*, 2017]. Area strain is the equivalent on surfaces of the Jacobian in 3D images to measure a relative local change of volume.

The local area strain (LAS) between end-diastole and end-systole was computed at every landmark of the mesh. For an area of n corresponding triangular cells on two surfaces, we compute the difference of area combining these cells between S and S' .

$$LAS^{S-S'} = \frac{(A_S - A_{S'})}{A_S} \quad (5.3)$$

Here we use it to test the isometric property of the parallel transport scheme: we measure the area strain between the original subject's meshes S and S' , and compare it to the one measured between the atlas T and the deformed atlas T' obtained by the parallel transport algorithm.

$$ASE^2 = \sum_i (LAS^{S-S'} - LAS^{T-T'})^2 \quad (5.4)$$

On our data, area strain was computed for the original subject's ED-ES changes using point-to-point correspondences (original area strain), and for the warped template's ED-ES changes after parallel transport (algorithm-specific area strain). Figure 5.5 compares different algorithms to see how well they preserve area strain during transport. We show here global area strain as well as that of two regions, the lateral and inferior wall, where deformation of the right ventricle predominates. The regions follow the standard in [Haddad *et al.*, 2008].

Here are the main findings of strain analysis for parallel transport algorithms:

- Pole ladder and conjugation action with SVF showed similar distributions compared to the original, including in the lateral wall. Surface wrinkles in the lateral wall at end-systole, increasing the difficulty in transport. This detail implies that the SVF setting is suitable for describing subtle deformations.
- Conjugate action with SVF was not consistent in terms of median area strain in the inferior wall.
- Pole ladder with LDDMM worked globally, was robust in class I,II, but exhibited higher area strain differences in Class III and IV. Since class III and IV are more distant from the template, we think that these differences are due to less satisfying registration (major issue with LDDMM here) quality in these two classes.
- Conjugate action for LDDMM stretched the range of area strain and was less adequate in distinguishing the classes.

We conclude that the pole ladder is rather suitable with SVF and LDDMM (even if LDDMM needs more delicate settings for the registration parameters), while conjugation has slightly lower performance, especially for LDDMM.

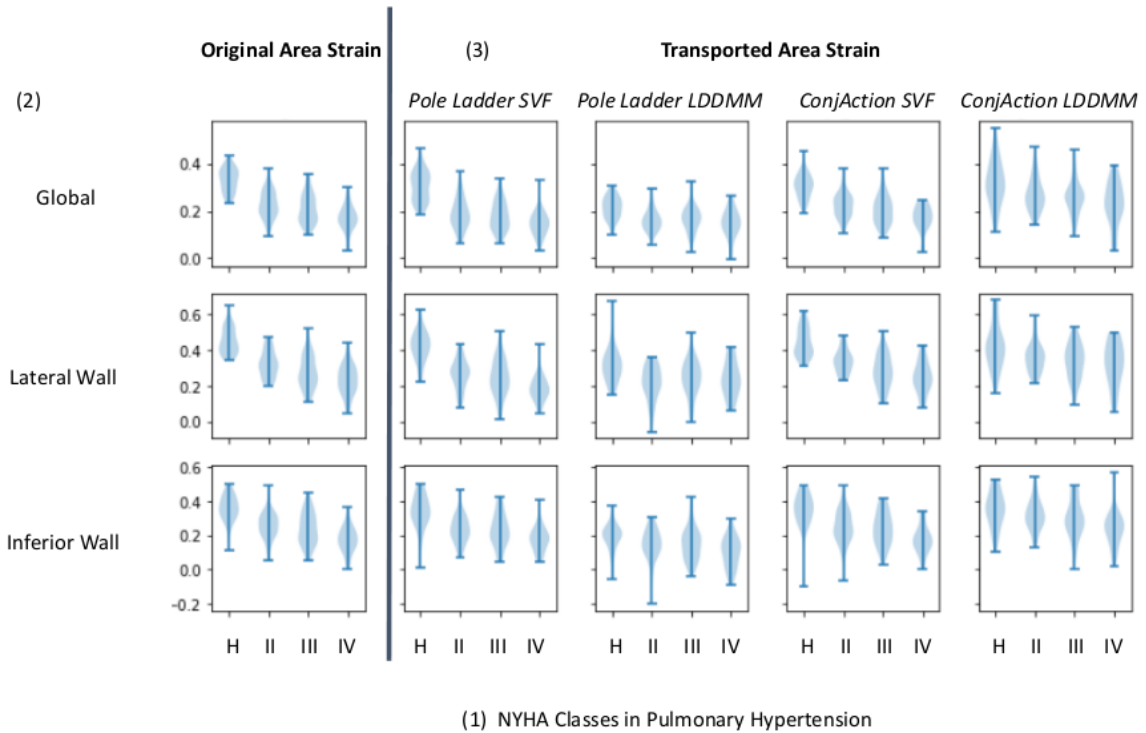


Figure 5.5: Comparison of different algorithms for the preservation of area strain across clinical subgroups during transport. (1) *H* represents the healthy subgroup, *II*, *III*, *IV* represent NYHA classes for pulmonary hypertension. (2) Global area strain of the right ventricle, as well as the area strain of the lateral wall and the inferior wall. (3) "Original" means the original subject's ED-ES deformation, while for parallel transport algorithms, the warped template's ED-ES deformation after transport. Mismatch of the trend of area strain in disease progression for conjugate action for SVF, on the inferior wall.

Table 5.2: *Compactness of the representations*

Explained variations	85%	95%	98%
Displacement	6	11	16
Pole Ladder SVF	7	10	14
Pole Ladder LDDMM	13	20	25

5.3.5 Statistical Modeling of Cardiac Deformation

In this subsection, we model ED-ES deformation in the whole subgroup of healthy subjects using parallel transports. Similar to the first step described in the previous experiments, we transported the velocity fields associated to each subject’s ED-ES changes to the template at end-diastole. Then, we applied principal component analysis (PCA) on the transported velocity fields, and warped the template with resulting principal components to show the main modes of deformation among this subgroup. We also compared this with the PCA modes obtained from the point-to-point ED-ES displacement.

5.3.5.1 Modes

The first mode from point-to-point displacement accounts for the elongation (no relative displacement of the two valves), the second accounts for the vertical displacement and a slight orientation of the tricuspid valve. The first two modes from the pole ladder with SVF are mainly related to the orientation and the relative position of the tricuspid valve and the pulmonary valve. Figure 5.6 summarizes these results for the point-to-point displacement and the pole ladder with SVF in the healthy subgroup.

When we project all populations on the first two modes, the direction following the progress from class II to IV is also the path control-patient in displacement, while in the mapping of the first two modes derived from the pole ladder with SVF, healthy subjects are randomly distributed along the path from class II to IV.

Nevertheless, the generative quality of SVF and LDDMM models clearly outperforms the PCA on displacement vectors since they avoid any self-intersection of meshes in the range of the population motion variability.

5.3.5.2 Compactness

We compared the compactness of the representations (Table 5.2) and found the pole ladder with SVF the best explanation, while the pole ladder with LDDMM a tedious explanation.

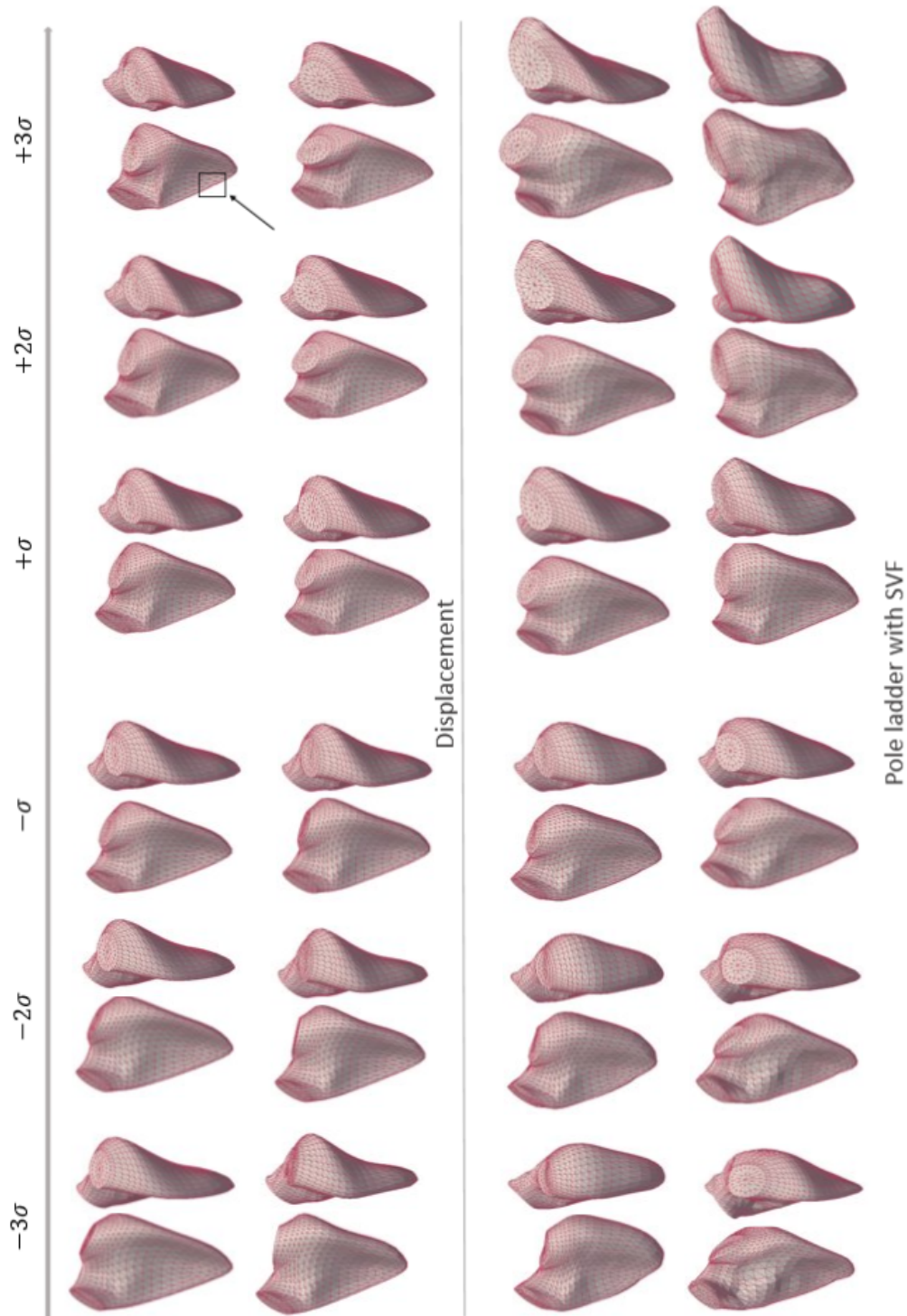


Figure 5.6: Comparison of point-to-point displacement (top) and the pole ladder with SVF (bottom) in the compact representation of end-diastole-end-systole (ED-ES) deformation. First two modes of variation are very different after applying PCA on the transported ED-ES changes. Surface folds appear at 3σ for point-to-point displacement (arrow).

5.4 Algorithmic Improvement for Riemannian Geodesics

The previous section shows that not only is the pole ladder of SVFs *exact* in theory, as in affined symmetric space, it also shows higher reliability and consistency in practice. While, for LDDMM, the velocity fields are endowed with right-invariant metric, whose flows are Riemannian geodesics, for which the pole ladder is not exact. The registration error (FLE) is significant.

To improve the numerical accuracy of the pole ladder in LDDMM setting, I did a joint study with Nicolas Guigui. We propose new computations of mid-point and symmetry, which take into account the registration error as residuals, transport it together with the deformation.

5.4.1 Decomposition with Deformation and Residual

The registration problem, as defined in Eq. 4.2.2.1, between a template shape T and a target mesh S optimizes the sum of residuals and a regularization term. In LDDMM, the optimization problem minimizes the following criterion:

$$C(c, \vec{\alpha}) = \|S - \phi^{c, \vec{\alpha}}(T)\|_2^2 + \frac{1}{\sigma^2} \cdot \|v_0^{c, \vec{\alpha}}\|_H, \quad (5.5)$$

where initial control points and momenta are noted as $c, \vec{\alpha}$; v_0 is the initial velocity field; the scalar product of velocity fields $\|\cdot\|_H$ is defined as $\langle v, v' \rangle_H = \sum_i \sum_j K(c_i, c'_j) \vec{\alpha}_i^T \vec{\alpha}'_j$ forming a pre-Hilbert space ².

If we measure the distance between shapes by the L_2 distance between points of the meshes, the resulting v_0 is a logarithm at the identity of ϕ . The regularization factor $\frac{1}{\sigma^2}$ impacts the geometry of the underlying space. It allows a smooth interpolation between solutions that belong to two paradigms - exact matching of LDDMM and point distribution models (no deformation).

5.4.2 Formulations Accounting for Residuals

According to the registration definition, $S_i = \phi_i T + \delta_i$, we propose to decompose the space of shapes into a deformation part encoding the orbit of the template, and a Euclidean space of residual displacement field (corresponding to point distribution model).

With this new definition of the deformation process, a diffeomorphic matching plus a residual displacement, we can recalculate the midpoint and symmetry based on the previous proposed Algo. 2. This small change in formulation, as to be demonstrated later, is sufficient to improve the parallel transport.

²Any pre-Hilbert space that is additionally also a complete space is a Hilbert space.

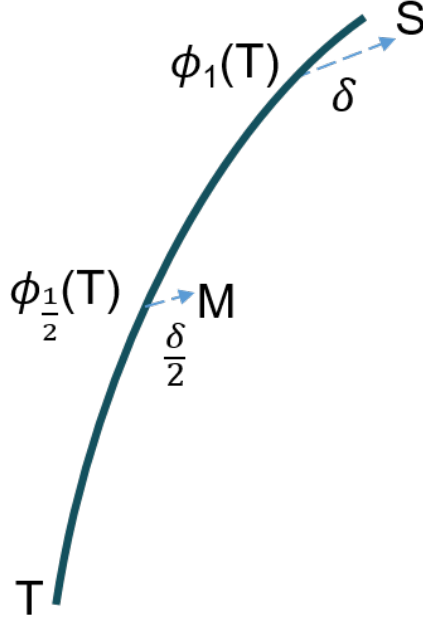


Figure 5.7: Midpoint with residuals

5.4.2.1 Formulation of Midpoint with Residuals

With this decomposition, a midpoint between T and S as shown in Fig. 5.7 is defined by:

$$M = \phi_1\left(\frac{T}{2}\right) + \frac{1}{2}\delta = \text{Exp}_T\left(\frac{1}{2}\text{Log}_T(S)\right) + \frac{1}{2}\delta. \quad (5.6)$$

This elementary algorithmic component constructs the midpoint shape on the geodesic between two original shapes. However, as the definition is not symmetric with respect to source and target shape, we will examine how much different if we obtain two midpoint with the two deformation directions.

5.4.2.2 Formulation of Symmetry with Residuals

Similarly, a symmetry is defined by inverting the geodesics and the residuals, as shown in Fig. 5.8:

$$s_T(S) = \text{Exp}_T\left(-\text{Log}_T(S)\right) - \delta. \quad (5.7)$$

This elementary algorithmic component constructs the symmetric shape of an original shape with respect to another one. To evaluate the symmetry in practice, we examine how much different are the original shape and the shape if we map the symmetry twice.

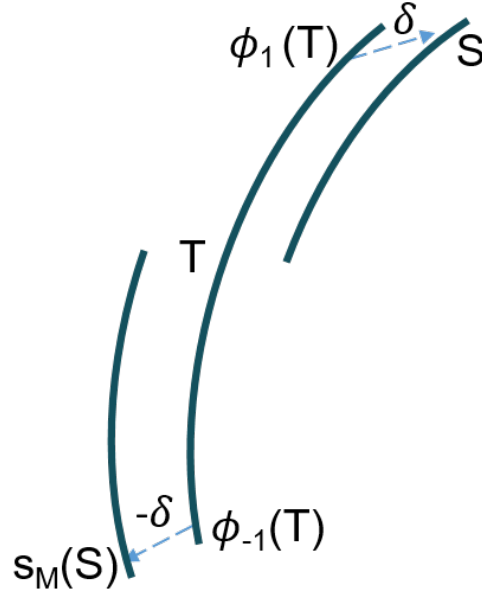


Figure 5.8: *Symmetry with residuals*

5.4.3 Affine Symmetric Space

As proven in Eq. 5.2.2, all error terms vanish in a convex normal neighborhood of an affine connection space (provided that geodesics and mid-points are computed precisely).

We first recall the definitions of symmetric space [Postnikov, 2001, chap. 1-10]. A Hausdorff connected manifold \mathcal{X} is called symmetric if for each $p \in \mathcal{X}$, there exists a diffeomorphism $s_p : \mathcal{X} \mapsto \mathcal{X}$ that verifies the following properties:

1. the map $(p, q) \in \mathcal{X} \times \mathcal{X} \mapsto s_p q \in \mathcal{X}$ is smooth.
2. $\forall p \in \mathcal{X}, s_p \circ s_p = Id$ (symmetry).
3. $\forall p \in \mathcal{X}, p$ is an isolated fixed point of s_p .
4. $\forall p, q \in \mathcal{X}$, writing $p' = s_p q$ then $s_p \circ s_q = s_{p'} \circ s_p$ (transvection).

Then there exists a unique affine connection ∇ such that \mathcal{X} is both locally symmetric ($\nabla R = 0$ and $T = 0$) and globally symmetric (the s_p are the local geodesic symmetries and are defined on the whole manifolds \mathcal{X}), which means a covariantly constant curvature (∇R).

5.4.4 Types of Errors

To evaluate our proposed symmetric pole ladder, we defined the following desired properties, based on midpoint and symmetry formulation, and the basic properties that symmetries must verify in an affine symmetric space. We examine these properties to assess the performance of the algorithm and the implementation error.

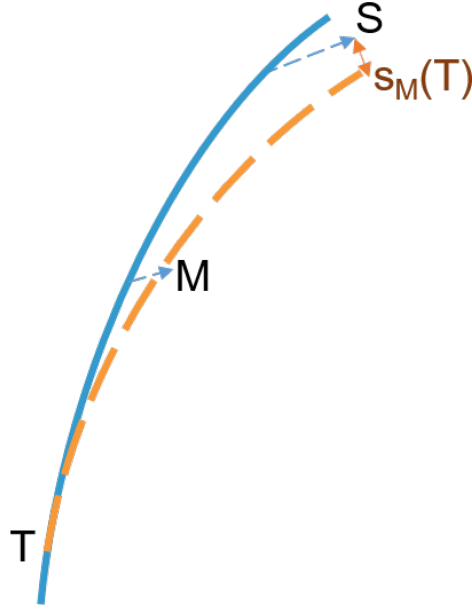


Figure 5.9: Type of error I: Centrality

Centrality the first desired consistency property is the compatibility of the midpoint with the symmetry, $s_M(T) = S$. However, these symmetries are affine mappings if and only if the space is locally symmetric [Postnikov, 2001, Prop 4.2].

Involutivity the second desired property is that the symmetry formulation is inversely consistent, $s_M(s_M(S')) = S'$. Ideally, if the log and exp maps are exact, $s_M \circ s_M = Id$.

Transvectivity the third desired property is that in an affine globally symmetric space, symmetries must verify the transvection property [Postnikov, 2001, Prop 5.3], $\forall M, S \in \mathcal{V} \quad s_M \circ s_S = s_T \circ s_M$, where $T = s_M(S)$. Using the deviation to this ideal case, we can also have the proxy to measure the gradient of the curvature of the space in the directions of interest (Eq. 5.2.2).

These properties relate to the inverse consistency that we evaluated previously. The three types of errors are illustrated respectively in Fig. 5.9, Fig. 5.10 and Fig. 5.11.

5.4.5 Decomposition Continuum

Now, let us look back at the decomposition of shape space with deformation and residuals (Sec. 5.4.1. If we put a regularization factor $\frac{1}{\sigma^2}$ like in the optimization process of LDDMM registration, $S_i = \phi_i T + \frac{1}{\sigma^2} \delta_i$, it allows to form a continuum of decompositions of the space of diffeomorphisms under consideration:

- $\sigma \rightarrow \infty, \delta \rightarrow 0$: LDDMM - Riemannian space of deformations of Levi-Civita connection where the metric is not compatible with the Cartan-Shouten connection.

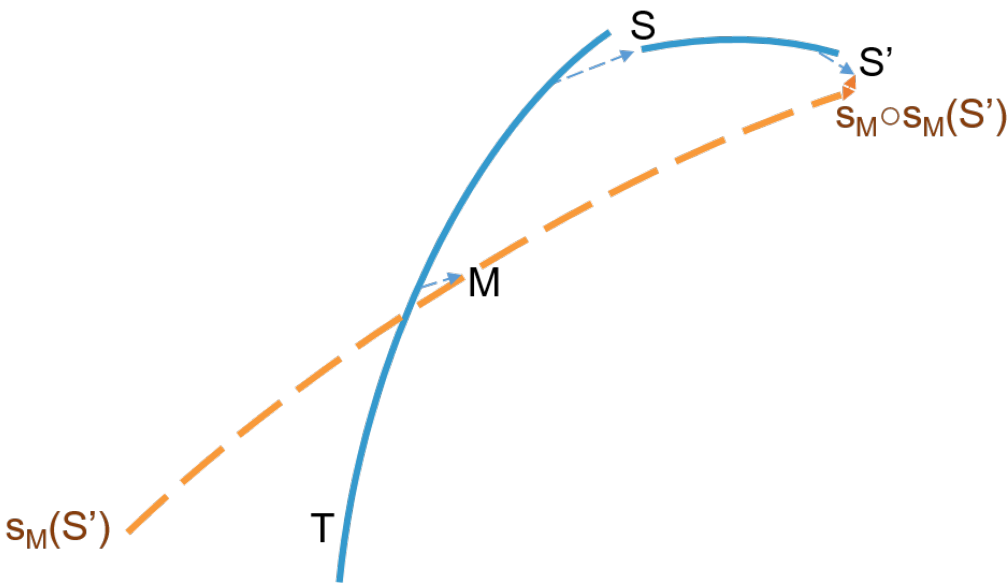


Figure 5.10: Type of error II: Involutivity

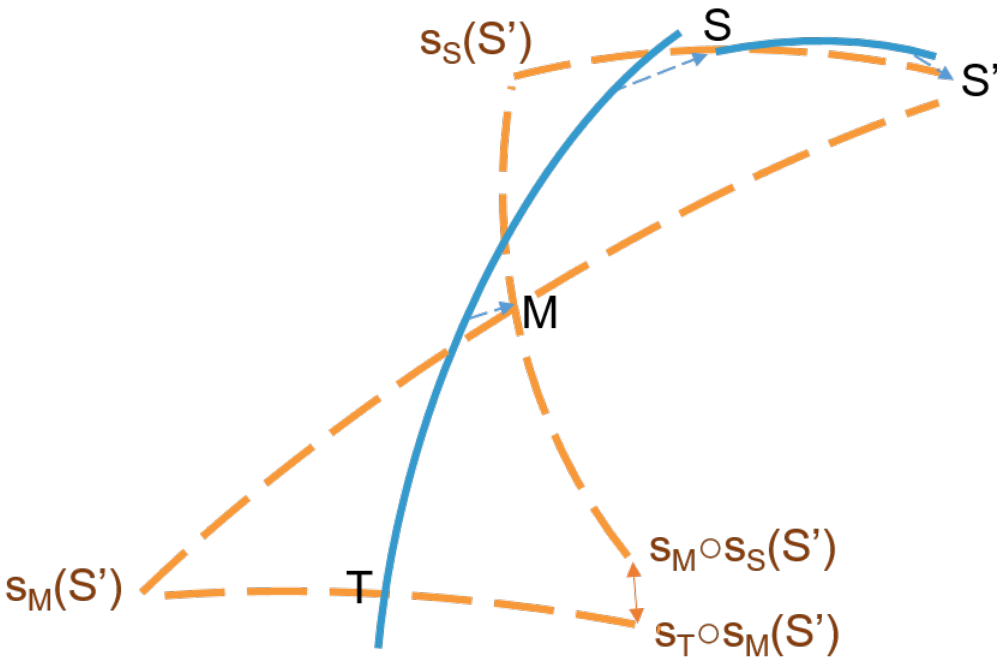


Figure 5.11: Type of error III: Transvectivity

This space is not symmetric.

- $\sigma \rightarrow 0, v_0 \rightarrow 0$: Ambient space with Euclidean norm, which is symmetric. This extremality corresponds to the point distribution model framework.

Accounting for residuals under this scheme, we expect to improve centrality and transvectivity. Deviations from these three types of errors are due to a non-zero covariant derivative of the curvature tensor with the LDDMM metric. Conversely, we may interpret transvection errors as estimates of the numerical curvature gradient that encompass all the approximations due to the implementation.

5.4.6 Results

We used the same database of 138 4D cardiac meshes of right-ventricular meshes. We transported individual ED-ES deformation to the template using the previous method and the newly developed method with residuals (the choice of regularization term σ) to compare the performance. The evaluation process includes the three types of errors.

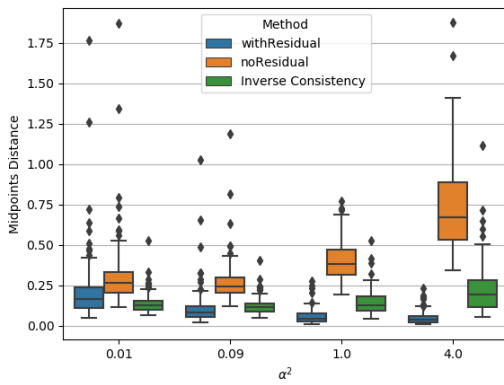
The main findings are:

- using residuals in the symmetry considerably improves the numerical accuracy of the computation of a midpoint, as displayed in Fig. 5.12a. The distance between midpoints computed by shooting from T or from S is reduced when using the residuals. This error compares well with the inverse consistency error in general and is even significantly lower for $\alpha \geq 1$.
- using residuals increases numerical accuracy in terms of centrality and involutivity errors, as displayed in Fig. 5.12b and Fig. 5.12c. For centrality, the error when using residuals is consistently smaller than without residuals, and this gain becomes larger as α grows. Centrality error is significantly lower than the registration error for $\alpha \geq 1$. The same behavior is observed for the involutivity.
- the LDDMM space endowed with the right invariant metric is not symmetric, and the transvectivity error reflects the covariant derivative of the curvature. Pushing registration with a small α generates larger errors, and there is an optimal $\alpha \in [1; 2]$ for which the space is closest to being symmetric, as displayed in Fig. 5.12d. Using residuals, this error decreases as the space flattens to Euclidean space, and deformations tend to the identity.

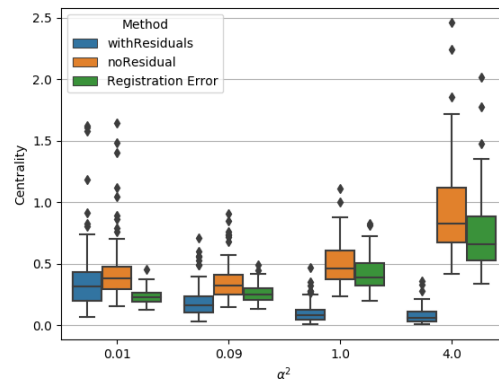
5.5 Discussions

5.5.1 Limitations

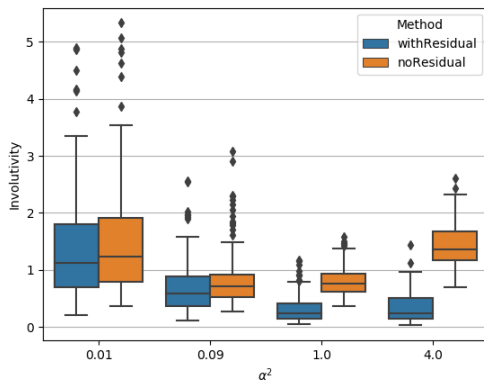
Cardiac motion tracking established point-to-point correspondences between mesh vertices, available here to benchmark our method. For databases that do not have such correspondence, one option is to register the segmented surfaces to the template, with



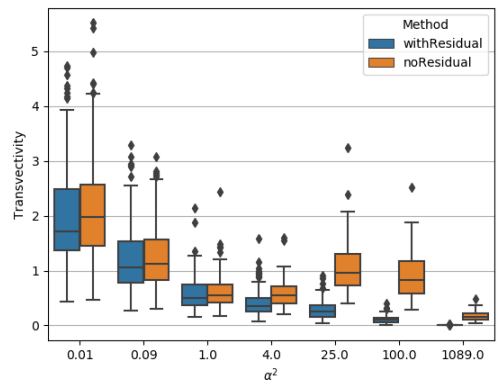
(a) Distance between Midpoints



(b) Centrality



(c) Involutivity



(d) Transvectivity

Figure 5.12: The four errors for different values of regularization α^2 , with and without residuals in the computation of the midpoint and the symmetries.

the framework of currents or Varifold-based deformation, which provides elegant mathematical approaches to match surfaces and establish point-to-point correspondence.

With more extensive datasets, it is promising to explore and discover more pathology patterns in the whole sequence of cardiac motion, with the help of deep learning and computational technologies, which shall benefit researches in medicine and patients.

5.5.2 Main Contributions

We proposed a general scheme to perform statistical modeling of the temporal deformation of the heart, directly based on meshes. We encoded the motion/the intrasubject deformation, and the intersubject shape variations, with diffeomorphisms parameterized either by stationary SVFs or by time-varying velocity fields in the LDDMM framework. Experiments on a 4D right-ventricular endocardial meshes database demonstrated the stability of our transport algorithm, of importance for the assessment of pathological changes. The method is adaptable to other anatomies with temporal or longitudinal data.

We first contributed a stable and very efficient adaptation of the pole ladder algorithm for the parallel transport of deformation of meshes instead of images.

Then, we proposed an extension of this pole ladder scheme, which relies on finding a middle point on the inter-subject geodesic and two symmetry computations. The reformulation of the pole ladder with mid-point and symmetry provided a more consistent method for parallel transport of surface shape.

We demonstrate the numerical consistency and stability of our transport algorithms by computing their inverse-consistency and the consistency of the transported deformation features of the mesh, area strain (a surfacic equivalent of the Jacobian in images), related to patient risk stratification and survival.

The statistical modeling of temporal deformation of the population using PCA showed that the pole ladder with SVFs exhibited a more compact and interpretable description of the normal variability of ED-ES deformation, with an equivalent predictive power for the pathological states. The algorithm also prevented surface folds in the range of population variability.

Because the right invariant structure does not give rise to a symmetric space, the pole ladder is an approximation in the LDDMM setting. The introduction of residuals to compute the midpoint and symmetry for the pole ladder resulted in improvement for the pole ladder with LDDMM. This work improved the previously tedious performance with LDDMM primarily due to the issue of registration robustness.

Furthermore, this reformulation decomposed the space of shape into deformations and residuals. We estimated how far the continuum of decomposition of shape space is from symmetric space using the basic properties of affine symmetric space. Taking into account residuals in transport, we found an optimal regularization factor to achieve a space closest to being symmetric, between non-symmetric LDDMM-Riemannian space and Euclidean space.

We integrated the two frameworks SVF and LDDMM in this newly formulated pole ladder scheme.

5.5.3 Future Work

Perspectives notably include synthetic experiments, the possibility to simulate a physiologically realistic motion on a given subject's anatomy, of relevance to understanding shape and motion interactions better, or inversely to generate template sequences derived from populations, to be used for physiological modeling. Besides, transporting modes of motion on subject-specific anatomy, or inversely, can be used to generate 4D sequences for physiological (mechanical/electrical) modeling. The transport also provided theoretical rationality for learning algorithms to learn motion from training data [*Krebs et al.*, 2018].

"All our knowledge begins with the senses, proceeds then to the understanding, and ends with reason. There is nothing higher than reason."

— Emmanuel Kant

Conclusion and Perspectives

Contents

6.1	Main Contributions	99
6.1.1	Imaging - Robust Image Segmentation	99
6.1.2	Computational Anatomy - Shape and Deformation	100
6.1.3	Clinical Implications	101
6.2	Future Work	101
6.2.1	Short Term	101
6.2.1.1	Fat and Epicardial Tissue Classification	101
6.2.1.2	SysAFib Cohort	102
6.2.2	Long Term	102
6.2.2.1	Cardiac Motion Modeling	102
6.2.2.2	Simulation	102

6.1 Main Contributions

The main objective of the thesis was to develop tools to analyze pre-ablation imaging data in atrial fibrillation (AF), stratify individual disease status and risk of arrhythmia recurrence.

6.1.1 Imaging - Robust Image Segmentation

Non-invasive extraction of the anatomical structures of the heart is a critical prerequisite in this study.

We developed an interactive region growing pipeline and a deep 3D convolution neural network model - dual 3D U-Nets structure - to segment the left atrium from computed tomography (CT) images. The region growing pipeline allows radiologists to use their expertise in the process of isolating the left atrium from its surrounding environment, which guarantees reliable segmentation. The results can generate accurate 3D models of the left atrial shape for shape analysis and ablation guidance, whereas

the neural network model reduces the time-consumption of the segmentation process significantly. To take into consideration the left atrial shape specificities, we proposed to include distance maps and created a Contour loss function for convolutional neural networks. Contour loss can play a fine-tuning role because it focuses on the boundary of the left atrium, which is the target of segmentation instead of the volume inside the left atrium. With Contour loss, the prediction showed smaller Hausdorff distance and less granular errors. Finally, to improve the performance and robustness of the method, we trained multiple models with different parameter settings, deployed the bootstrapping concept, and combined several U-Nets into a stronger predictive model using a majority voting strategy. Experiments with two different databases, cardiac images and renal cortex scans, supported the soundness of employing such strategy.

This work leads to the potential implementation of these image segmentation tools in a clinic-oriented AF management pipeline. The generic method can adapt to external imaging data and segmentation of other organs, such as ventricles.

We further looked into a fine layer of the heart, the left atrial myocardium. Making use of patient-specific intensity value information and clinical insights, we were able to solve the challenging task of segmenting the myocardium from cardiac CT images, which consists of only few pixels and is of low contrast. The method combined intensity-based exclusion of external tissues and shape-based active contour modeling, into a renewed geodesic active model for this specific task. Results showed that our method achieved an excellent correlation of the thickness of the wall compared with manual segmentation.

The preliminary analysis of the epicardial adipose tissue volume in the wall indicated that it is associated with AF severity.

6.1.2 Computational Anatomy - Shape and Deformation

Through population-wise analysis of the left atrial shape, we extracted features of the left atrial shape related to arrhythmia recurrence in AF, providing incremental predictive value beyond conventional indicators.

We developed a two-step partial least square regression approach to exclude first shape features linked with the left atrial volume. Then, we learned a global shape score to evaluate for each subject the risk of multi-procedural failure, based on pre-ablation left atrial images. Combining global shape scores with indexed left atrial volume and AF persistence, we stratified recurrence risk on a patient-by-patient basis in a multivariate model.

On a local level, we performed statistical testing of area change on the vertices of the left atrial surface. We found critical regions significantly associated with arrhythmia recurrence mostly on a large area extending from the inferior part of the posterior atrial body up to the mitral isthmus, covering left inferior pulmonary vein. More focal differences laid close to the antrum of left and right superior veins, as well as within the septum and anterior wall.

In addition to static shape analysis of the left atrium, we also proposed a general scheme to perform statistical modeling of the temporal deformation of the heart. The

extensions of the pole ladder to a mid-point and symmetry formulation improved the numerical consistency and stability of parallel transport in practice. We built pole ladder with a midpoint computation and two symmetry computations. The error terms of parallel transport show that the pole ladder is exact in one step in symmetric spaces.

Flows of stationary velocity fields (SVFs) are geodesics of symmetric Cartan-Schouten connection. Additionally to the pole ladder on SVFs being exact in theory, we also found higher consistency in numerical implementation. Next, we introduced residuals in registration, which resulted in a continuum of decomposition of the shape space, from Riemannian space to Euclidean space of the point distribution model, which is symmetric. For large deformation diffeomorphic metric mapping (LDDMM) whose flows are endowed with the right-variant metric, the results showed that the symmetric pole ladder with residuals approximated more closely symmetric space. A stable and accurate parallel transport to mesh deformations is of importance for the assessment of pathological changes.

6.1.3 Clinical Implications

Given the existing indications of pre-procedural CTs and the rapidly developing automatic image processing techniques, we could easily implement the approach described in this manuscript in clinically-oriented software to extract prognostic information and personalize patient management. This study can be extended to magnetic resonance imaging following appropriate image segmentation.

In persistent forms of AF, the indications for catheter ablation are still rising debates. Tailoring individual treatment strategies can improve the response rate to catheter ablation. One strategy consists of better identifying patients who are unlikely to respond to therapy, while another recognizing better ablation target. The adverse structural findings on pre-operative imaging (left atrial at-risk shape and critical regions of enlargement), could potentially lead to additional ablation targets outside pulmonary veins for treatment planning.

6.2 Future Work

6.2.1 Short Term

In the short term, future work includes the following two projects.

6.2.1.1 Fat and Epicardial Tissue Classification

Based on the left atrial wall segmentation, we further investigate the distribution of tissues inside the heterogeneous LA wall, notably the adipose tissue. Clinicians observed that patients with higher Body Mass Index (BMI) proceed higher risk of arrhythmia recurrence, therefore they recommend weight control for AF management.

2D/3D mapping of the fat, combined with computational anatomy tools, can potentially reveal more features related to patient classification. We could further improve the segmentation of the left atrial wall by coupled U-Nets. We could develop generic and patient-specific parametric models for fat distribution in AF. New methods need to be developed to represent such unstructured data.

6.2.1.2 SysAFib Cohort

The goal of the SysAFib project is to create several individual risk scores from various types of pre-ablation information and then integrate these scores into a single decision support system. The evaluation cohort consisting of 30 patients is collected at Oslo University Hospital and Maastricht University.

Interdisciplinary collaborators run the individual risk stratification separately based on genetic profiling, ECG analysis, and statistical shape analysis. Then, the proposed combination method is to build a Bayesian multivariate model to be evaluated on this external database for validation.

6.2.2 Long Term

In the long term, the study leads to multiple future potential projects.

6.2.2.1 Cardiac Motion Modeling

The work on parallel transport is continuing with the PhD project of Nicolas Guigui in the team. The application of the symmetric pole ladder in multiple databases can produce a comparison of our method with other methods on various types of shape/deformation with diffeomorphism.

It would be interesting to extend the current mesh-based approach to image data (3D volume). The computation of mid-point and symmetry for images need to be implemented and tested. As the registration of images (non-affine transformation + intensity variations) is different from that of meshes, how to reach a numerical consistency remains a critical issue. In addition, extending the end-diastole to end-systole analysis to the analysis of the whole cardiac sequences may reveal pathological motion patterns in the cardiac cycle. With each interval between two instances being a small step of parallel transport, the pole ladder needs to be performed in a consistent manner for the whole sequence.

6.2.2.2 Simulation

We raise some questions during the study about the underlying causality of AF and its associated consequences (stroke, heart failure). Potential future work includes the extension to atrial physiology, investigating the physiological meaning of the features found in the retrospective population-based studies.

Other than shape remodeling, the cardiac electrophysiology and intervention procedure also play a vital role in determining the outcome of catheter ablation. The

electrophysiological and interventional data can be analyzed through parametric biophysical models.

Finally, two future PhD projects within a European project continue investigating atrial physiology from the perspective of fluid flow simulation inside the left atrium with different anatomies for stroke prediction. Detailed region-wise anatomical models may be useful in such flow simulation. Another perspective is to study the relationship between the critical regions and typical sites for atrial fibrosis.

Integrating these models should give us a comprehensive understanding of the left atrial features, reveal the relevance between shape and cardiac function (contraction, electrophysiology), and ultimately inspire new treatment methods in the AF.

Appendices

Contents

A	Data Science Tools	105
A.1	Principal Component Analysis	105
A.2	Partial Least Squares Regression	106
B	Coding Platforms	106
B.1	DTK Visual Programming	106
C	Parameter-Setting for JFR 2018 Renal Cortex Segmentation	107

A Data Science Tools

Here we present the mathematical formulation of two conventional approaches for dimension reduction in statistical learning, principal component analysis (PCA), and partial least squares (PLS) regression.

A.1 Principal Component Analysis

PCA uses an orthogonal transformation to convert a set of observations of possibly correlated variables into a set of values of linearly uncorrelated variables called principal components. The most significant variance of the observations comes to lie on the first coordinate, called the first principal component, the second most significant variance on the second coordinate, and so on [Jolliffe, 2002].

We summarize the process of PCA and pathological analysis as: selecting the first p modes that explain at least $\pi\%$ of the deformation variability; representing a subject by a low-dimensional shape vector space, as Eq. 6.1; relating the shape vector, whose elements quantify the amount of variability along the m^{th} mode, to clinical parameters, such as the type of atrial fibrillation, and identifying pathological shape features.

$$\begin{aligned} f_{PCA}^i &= \{f_{PCA}^{i,m}\}_{m=1,2\dots p} \\ f_{PCA}^{i,m} &= K_V(v_0^i, v_0^m), \end{aligned} \tag{6.1}$$

where v_0^m is the m^{th} PCA mode.

Statistical tests following PCA analysis determine the reliability of correlation.

A.2 Partial Least Squares Regression

The general model of PLS regression is

$$\begin{aligned}\mathbf{X} &= \mathbf{TP}^\top + \mathbf{E} \\ \mathbf{Y} &= \mathbf{UQ}^\top + \mathbf{F},\end{aligned}\tag{6.2}$$

using the notations in [Geladi and Kowalski, 1986].

PLS explores fundamental relations between two matrices, X , predictors, and Y , the responses/observations. PLS models the covariance structures in these two spaces. It finds the multidimensional direction in the X space that explains the maximum variance in the Y space. Compared with PCA in regression, instead of finding hyperplanes of maximum variance between two spaces, it finds a linear regression model by projecting X , predictors, and Y , the response, to a new space [Geladi and Kowalski, 1986].

We summarize the process of PLS regression as: computing the first q modes of the deformations span an optimal subspace that simultaneously explains $\pi_X\%$ of the variance of the predictors and $\pi_Y\%$ of the variance of the response; representing a subject by a low-dimensional shape vector, as Eq. 6.3; identifying pathological shape features.

$$\begin{aligned}f_{PLS}^i &= \{f_{PLS}^{i,m}\}_{m=1,2,\dots,q} \\ f_{PLS}^{i,m} &= K_V(\beta^i, m_{th} \text{ PLS mode}).\end{aligned}\tag{6.3}$$

B Coding Platforms

The interface of MUSIC software allows interactive image and mesh processing by clinicians, as shown in Fig. 6.1. It is developed based on the medInria software platform. I used the software to visualize, filter, pre-process images, and generate meshes from binary masks using the VTK library. Several pipelines dedicated to cardiac imaging have been implemented, including the one for atrial fibrillation. The clinical-oriented pipelines aim to integrate the whole workflow of patient management, ranging from image processing, detailed anatomy modeling, mesh manipulation, and interventional guidance [Liryc and Inria, 2019].

B.1 DTK Visual Programming

DTK is a meta platform developed at Inria for software development, providing the foundation for the development of specific and modular science platforms. With image and mesh data type and other basic functionalities integrated via low-level bricks - plugins, the additional layers can be developed across coding libraries, notably ITK and VTK for manipulating medical images and other scientific data, via aggregating top-level scripts and plugins. It also provides a visual programming tool to connect the inputs and outputs of the modules. The pipeline can run the program for multiple files

in a directory with a loop. I used this platform to program my task-specific modules for the very first project in my Ph.D. program, as shown in Fig. 6.2.

C Parameter-Setting for JFR 2018 Renal Cortex Segmentation

Fixed parameters Training-validation split ratio = 0.8; Number of base filters = 16; Learning rate will be reduced to half after 10 epochs if the validation loss is not improving; Training will be stopped when the validation loss does not improve after 50 epochs; Initial learning rate = $5e^{-4}$; Batch size = 1; Max number of epochs = 500, Steps per epoch = 200; Horizontal flip for augmentation = True.

Changing parameters For image augmentation, Rotation range set to 10, 15, 30 or 45 degree; Width shift range and height shift range set to 0.1, 0.15, 0.3; Zoom in or not; Zoom range set to 0.2 or 0.3.

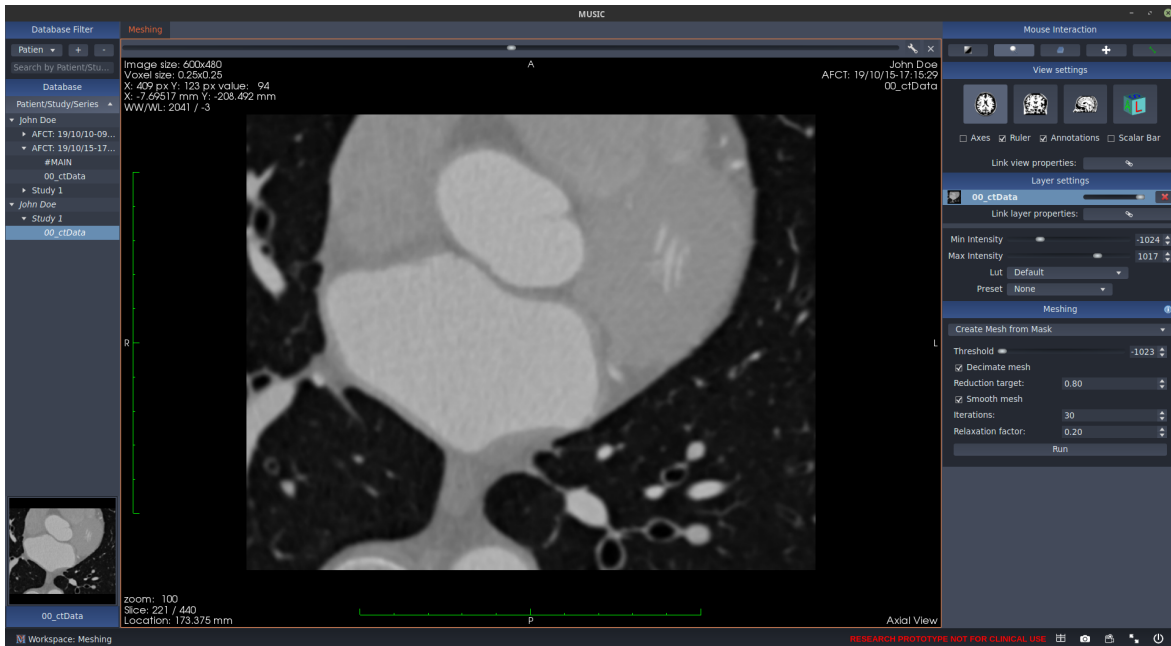


Figure 6.1: The interface of MUSIC software.

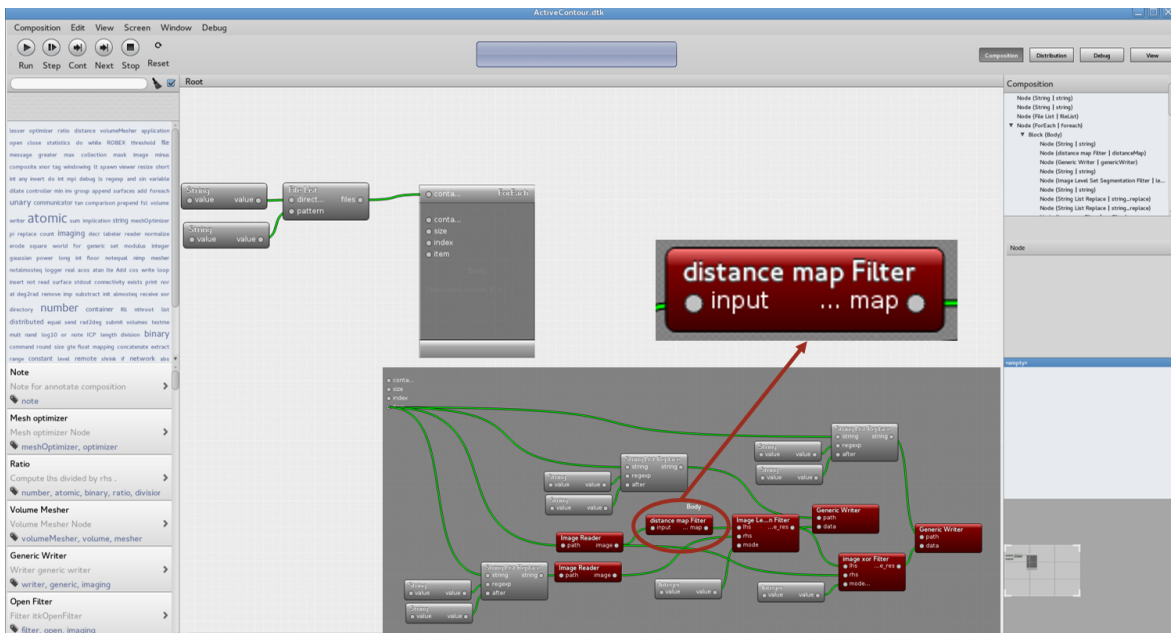


Figure 6.2: The implementation of the left atrial wall segmentation pipeline with DTK Visual Programming platform.

Bibliography

- Ablitt, N. A., J. Gao, J. Keegan, L. Stegger, D. N. Firmin, and G.-Z. Yang, Predictive cardiac motion modeling and correction with partial least squares regression, *IEEE transactions on medical imaging*, *23*(10), 1315–1324, 2004.
- Al Chekakie, M. O., C. C. Welles, R. Metoyer, A. Ibrahim, A. R. Shapira, J. Cytron, P. Santucci, D. J. Wilber, and J. G. Akar, Pericardial fat is independently associated with human atrial fibrillation, *Journal of the American College of Cardiology*, *56*(10), 784–788, 2010.
- Atrial Fibrillation Fact Sheet, Division for Heart Disease and Stroke Prevention, National Center for Chronic Disease Prevention and Health Promotion, 2016.
- Bai, W., W. Shi, A. de Marvao, T. J. Dawes, D. P. O’Regan, S. A. Cook, and D. Rueckert, A bi-ventricular cardiac atlas built from 1000+ high resolution mr images of healthy subjects and an analysis of shape and motion, *Medical image analysis*, *26*(1), 133–145, 2015.
- Balk, E. M., A. C. Garlitski, A. A. Alsheikh-Ali, T. Terasawa, M. Chung, and S. Ip, Predictors of atrial fibrillation recurrence after radiofrequency catheter ablation: a systematic review, *Journal of cardiovascular electrophysiology*, *21*(11), 1208–1216, 2010.
- Barghout, L., and L. Lee, Perceptual information processing system, US Patent App. 10/618,543, 2004.
- Bengio, Y., A. Courville, and P. Vincent, Representation learning: A review and new perspectives, *IEEE transactions on pattern analysis and machine intelligence*, *35*(8), 1798–1828, 2013.
- Benjamin, E. J., P. A. Wolf, R. B. D’Agostino, H. Silbershatz, W. B. Kannel, and D. Levy, Impact of atrial fibrillation on the risk of death: the Framingham Heart Study, *Circulation*, *98*(10), 946–952, 1998.
- Berruezo, A., D. Tamborero, L. Mont, B. Benito, J. M. Tolosana, M. Sitges, B. Vidal, G. Arriagada, F. Méndez, M. Matiello, et al., Pre-procedural predictors of atrial

- fibrillation recurrence after circumferential pulmonary vein ablation, *European heart journal*, 28(7), 836–841, 2007.
- Bieging, E. T., A. Morris, B. D. Wilson, C. J. McGann, N. F. Marrouche, and J. Cates, Left atrial shape predicts recurrence after atrial fibrillation catheter ablation, *Journal of Cardiovascular Electrophysiology*, 29(7), 966–972, 2018.
- Bisbal, F., E. Guiu, N. Calvo, D. Marin, A. Berruezo, E. Arbelo, J. Ortiz-Pérez, T. M. de Caralt, J. M. Tolosana, R. Borràs, et al., Left atrial sphericity: a new method to assess atrial remodeling. impact on the outcome of atrial fibrillation ablation, *Journal of cardiovascular electrophysiology*, 24(7), 752–759, 2013.
- Bisbal, F., F. Alarcón, A. Ferrero-de Loma-Osorio, J. J. González-Ferrer, C. Alonso, M. Pachón, H. Tizón, P. Cabanas-Grandío, M. Sanchez, E. Benito, and Others, Left atrial geometry and outcome of atrial fibrillation ablation: results from the multicentre LAGO-AF study, *European Heart Journal - Cardiovascular Imaging*, 19(9), 1002–1009, 2018.
- Bookstein, F. L., et al., Size and shape spaces for landmark data in two dimensions, *Statistical science*, 1(2), 181–222, 1986.
- Bossa, M., M. Hernandez, and S. Olmos, Contributions to 3D diffeomorphic atlas estimation: application to brain images, in *International Conference on Medical Image Computing and Computer-Assisted Intervention*, pp. 667–674, Springer, 2007.
- Bruse, J. L., K. McLeod, G. Biglino, H. N. Ntsinjana, C. Capelli, T.-Y. Hsia, M. Sermesant, X. Pennec, A. M. Taylor, S. Schievano, et al., A statistical shape modelling framework to extract 3d shape biomarkers from medical imaging data: assessing arch morphology of repaired coarctation of the aorta, *BMC medical imaging*, 16(1), 40, 2016.
- Caselles, V., R. Kimmel, and G. Sapiro, Geodesic active contours, *International journal of computer vision*, 22(1), 61–79, 1997.
- Cecco, C. N. D., G. Muscogiuri, A. Varga-Szemes, and U. J. Schoepf, Cutting edge clinical applications in cardiovascular magnetic resonance, *World Journal of Radiology*, 9(1), 1, doi:10.4329/wjr.v9.i1.1, 2017.
- CGAL, Cgal 4.8.1 - 3D mesh generation, 2016.
- Charon, N., and A. Trouvé, The varifold representation of nonoriented shapes for diffeomorphic registration, *SIAM Journal on Imaging Sciences*, 6(4), 2547–2580, 2013.
- Çiçek, Ö., A. Abdulkadir, S. S. Lienkamp, T. Brox, and O. Ronneberger, 3D U-net: Learning dense volumetric segmentation from sparse annotation, *Lecture Notes in Computer Science*, 9901 LNCS, 424–432, 2016.

- Cochet, H., R. Dubois, F. Sacher, N. Derval, M. Sermesant, M. Hocini, M. Montaudon, M. Haïssaguerre, F. Laurent, and P. Jaïs, Cardiac arrhythmias: multimodal assessment integrating body surface ecg mapping into cardiac imaging, *Radiology*, 271(1), 239–247, 2013.
- Cochet, H., A. Mouries, H. Nivet, F. Sacher, N. Derval, A. Denis, M. Merle, J. Relan, M. Hocini, M. Haïssaguerre, and Others, Age, atrial fibrillation, and structural heart disease are the main determinants of left atrial fibrosis detected by delayed-enhanced magnetic resonance imaging in a general cardiology population, *Journal of Cardiovascular Electrophysiology*, 26(5), 484–492, 2015.
- Cutler, M. J., J. Johnson, K. Abozguia, S. Rowan, W. Lewis, O. Costantini, A. Natale, and O. Ziv, Impact of voltage mapping to guide whether to perform ablation of the posterior wall in patients with persistent atrial fibrillation, *Journal of cardiovascular electrophysiology*, 27(1), 13–21, 2016.
- Dagres, N., H. Kottkamp, C. Piorkowski, S. Weis, A. Arya, P. Sommer, K. Bode, J.-H. Gerds-Li, D. T. Kremastinos, and G. Hindricks, Influence of the duration of holter monitoring on the detection of arrhythmia recurrences after catheter ablation of atrial fibrillation: implications for patient follow-up, *International journal of cardiology*, 139(3), 305–306, 2010.
- Davis, M. H., A. Khotanzad, D. P. Flamig, and S. E. Harms, A physics-based coordinate transformation for 3-d image matching, *IEEE transactions on medical imaging*, 16(3), 317–328, 1997.
- Dewland, T. A., M. Wintermark, A. Vaysman, L. M. Smith, E. Tong, E. Vittinghoff, and G. M. Marcus, Use of computed tomography to identify atrial fibrillation associated differences in left atrial wall thickness and density, *Pacing and Clinical Electrophysiology*, 36(1), 55–62, 2013.
- Donal, E., G. Y. Lip, M. Galderisi, A. Goette, D. Shah, M. Marwan, M. Lederlin, S. Mondillo, T. Edvardsen, M. Sitges, et al., Eacvi/ehra expert consensus document on the role of multi-modality imaging for the evaluation of patients with atrial fibrillation, *European Heart Journal - Cardiovascular Imaging*, 17(4), 355–383, 2016.
- Duchateau, N., M. De Craene, G. Piella, E. Silva, A. Doltra, M. Sitges, B. H. Bijnens, and A. F. Frangi, A spatiotemporal statistical atlas of motion for the quantification of abnormal myocardial tissue velocities, *Medical image analysis*, 15(3), 316–328, 2011.
- Durrleman, S., X. Pennec, A. Trouvé, and N. Ayache, Statistical models of sets of curves and surfaces based on currents, *Medical image analysis*, 13(5), 793–808, 2009.
- Durrleman, S., M. Prastawa, N. Charon, J. R. Korenberg, S. Joshi, G. Gerig, and A. Trouvé, Morphometry of anatomical shape complexes with dense deformations and sparse parameters, *NeuroImage*, 101, 35–49, 2014.

- Flüchter, S., D. Haghi, D. Dinter, W. Heberlein, H. P. Köhl, W. Neff, T. Sueselbeck, M. Borggrefe, and T. Papavassiliu, Volumetric assessment of epicardial adipose tissue with cardiovascular magnetic resonance imaging, *Obesity*, 15(4), 870–878, 2007.
- Gavrilov, A. V., Algebraic properties of covariant derivative and composition of exponential maps, *Matematicheskie Trudy*, 9(1), 3–20, 2006.
- Geladi, P., and B. R. Kowalski, Partial least-squares regression: a tutorial, *Analytica chimica acta*, 185, 1–17, 1986.
- Gray, H., *Anatomy of the human body*, vol. 8, Lea & Febiger, 1878.
- Gronemeyer, S. A., R. G. Steen, W. M. Kauffman, W. E. Reddick, and J. O. Glass, Fast adipose tissue (FAT) assessment by MRI, *Magnetic Resonance Imaging*, 18(7), 815–818, 2000.
- Guibert, R., K. Mcleod, A. Caiazzo, T. Mansi, M. A. Fernández, M. Sermesant, X. Pennec, I. Vignon-Clementel, Y. Boudjemline, and J.-F. Gerbeau, Group-wise Construction of Reduced Models for Understanding and Characterization of Pulmonary Blood Flows from Medical Images, *Medical Image Analysis*, 18(1), 63–82, 2013.
- Guigui, N., S. Jia, M. Sermesant, and X. Pennec, Symmetric algorithmic components for shape analysis with diffeomorphisms, *arXiv preprint arXiv:1906.05921*, 2019.
- Haddad, F., S. A. Hunt, D. N. Rosenthal, and D. J. Murphy, Right ventricular function in cardiovascular disease, part i: anatomy, physiology, aging, and functional assessment of the right ventricle, *Circulation*, 117(11), 1436–1448, 2008.
- Haissaguerre, M., M. Hocini, A. Denis, A. J. Shah, Y. Komatsu, S. Yamashita, M. Daly, S. Amraoui, S. Zellerhoff, M.-Q. Picat, et al., Driver domains in persistent atrial fibrillation, *Circulation*, 130(7), 530–538, 2014.
- Hassink, R. J., H. T. Aretz, J. Ruskin, and D. Keane, Morphology of atrial myocardium in human pulmonary veins: a postmortem analysis in patients with and without atrial fibrillation, *Journal of the American College of Cardiology*, 42(6), 1108–1114, 2003.
- Ho, S. Y., D. Sanchez-Quintana, J. A. Cabrera, and R. H. Anderson, Anatomy of the left atrium: implications for radiofrequency ablation of atrial fibrillation., *Journal of cardiovascular electrophysiology*, 10(11), 1525–1533, 1999.
- Hou, R., C. Chen, and M. Shah, An end-to-end 3d convolutional neural network for action detection and segmentation in videos, *arXiv preprint arXiv:1712.01111*, 2017.
- Huda, W., *Review of Radiologic Physics*, 74 pp., Lippincott Williams and Wilkins, Philadelphia, United States, 2010.

- Hunter, R. J., I. Diab, M. Tayebjee, L. Richmond, S. Sporton, M. J. Earley, and R. J. Schilling, Characterization of fractionated atrial electrograms critical for maintenance of atrial fibrillation: a randomized, controlled trial of ablation strategies (the cfae af trial), *Circulation: Arrhythmia and Electrophysiology*, 4(5), 622–629, 2011.
- Hunter, R. J., Y. Liu, Y. Lu, W. Wang, and R. J. Schilling, Left atrial wall stress distribution and its relationship to electrophysiologic remodeling in persistent atrial fibrillation, *Circulation: Arrhythmia and Electrophysiology*, 5(2), 351–360, 2012.
- Iacobellis, G., Epicardial and pericardial fat: close, but very different, *Obesity*, 17(4), 625–625, 2009.
- Inoue, J., A. C. Skanes, J. A. White, M. Rajchl, and M. Drangova, Patient-specific left atrial wall-thickness measurement and visualization for radiofrequency ablation, in *SPIE Medical Imaging*, pp. 90,361N–90,361N, International Society for Optics and Photonics, 2014.
- Inoue, J., J. S. Baxter, and M. Drangova, Left atrial wall segmentation from ct for radiofrequency catheter ablation planning, in *Workshop on Clinical Image-Based Procedures*, pp. 71–78, Springer, 2015.
- Isensee, F., P. Kickingereder, W. Wick, M. Bendszus, and K. H. Maier-Hein, Brain tumor segmentation and radiomics survival prediction: Contribution to the brats 2017 challenge, in *International MICCAI Brainlesion Workshop*, pp. 287–297, Springer, 2017.
- Jamin, C., P. Alliez, M. Yvinec, and J.-D. Boissonnat, CGALmesh: a generic framework for delaunay mesh generation, *ACM Transactions on Mathematical Software (TOMS)*, 41(4), 23, 2015.
- Jean, S., *Image Analysis and Mathematical Morphology*, Academic Press, Inc., Orlando, FL, USA, 1983.
- Jia, S., L. Cadour, H. Cochet, and M. Sermesant, STACOM-SLAWT Challenge: Left Atrial Wall Segmentation and Thickness Measurement Using Region Growing and Marker-Controlled Geodesic Active Contour, in *7th International Statistical Atlases and Computational Modeling of the Heart (STACOM) Workshop, Held in Conjunction with MICCAI 2016, LNCS*, vol. 10124, pp. 211–219, Springer, 2017a.
- Jia, S., C. Camaioni, M.-M. Rohé, P. Jaïs, X. Pennec, H. Cochet, and M. Sermesant, Prediction of post-ablation outcome in atrial fibrillation using shape parameterization and partial least squares regression, in *International Conference on Functional Imaging and Modeling of the Heart*, pp. 311–321, Springer, 2017b.
- Jia, S., A. Despinasse, Z. Wang, H. Delingette, X. Pennec, P. Jaïs, H. Cochet, and M. Sermesant, Automatically segmenting the left atrium from cardiac images using successive 3d u-nets and a contour loss, in *International Workshop on Statistical Atlases and Computational Models of the Heart*, pp. 221–229, Springer, 2018a.

- Jia, S., N. Duchateau, P. Mocerì, M. Sermesant, and X. Pennec, Parallel transport of surface deformations from pole ladder to symmetrical extension, in *International Workshop on Shape in Medical Imaging*, pp. 116–124, Springer, 2018b.
- Jolliffe, I., *Principal component analysis*, Wiley Online Library, 2002.
- Karim, R., STACOM Left Atrial Wall Thickness Challenge, 2016.
- Karim, R., L.-E. Blake, J. Inoue, Q. Tao, S. Jia, R. J. Housden, P. Bhagirath, J.-L. Duval, M. Varela, J. M. Behar, L. Cadour, R. J. van der Geest, H. Cochet, M. Drangova, M. Sermesant, R. Razavi, O. Aslanidi, R. Rajani, and K. Rhode, Algorithms for left atrial wall segmentation and thickness – evaluation on an open-source ct and mri image database, *Medical Image Analysis*, 50, 36 – 53, 2018.
- Kirchhof, P., S. Benussi, D. Kotecha, A. Ahlsson, D. Atar, B. Casadei, M. Castella, H.-C. Diener, H. Heidbuchel, J. Hendriks, G. Hindricks, A. S. Manolis, J. Oldgren, B. A. Popescu, U. Schotten, B. Van Putte, P. Vardas, and E. S. D. Group, 2016 ESC Guidelines for the management of atrial fibrillation developed in collaboration with EACTS, *European Heart Journal*, 37(38), 2893–2962, doi:10.1093/eurheartj/ehw210, 2016.
- Kleijn, S. A., M. F. Aly, C. B. Terwee, A. C. van Rossum, and O. Kamp, Three-dimensional speckle tracking echocardiography for automatic assessment of global and regional left ventricular function based on area strain, *Journal of the American Society of Echocardiography*, 24(3), 314–321, 2011.
- Krebs, J., T. Mansi, B. Mailhé, N. Ayache, and H. Delingette, Unsupervised probabilistic deformation modeling for robust diffeomorphic registration, in *Deep Learning in Medical Image Analysis and Multimodal Learning for Clinical Decision Support*, pp. 101–109, Springer, 2018.
- Kurotobi, T., K. Iwakura, K. Inoue, R. Kimura, Y. Toyoshima, N. Ito, H. Mizuno, Y. Shimada, K. Fujii, S. Nanto, et al., The significance of the shape of the left atrial roof as a novel index for determining the electrophysiological and structural characteristics in patients with atrial fibrillation, *Europace*, 13(6), 803–808, 2011.
- Kutra, D., A. Saalbach, H. Lehmann, A. Groth, S. P. Dries, M. W. Krueger, O. Dössel, and J. Weese, Automatic multi-model-based segmentation of the left atrium in cardiac mri scans, in *International Conference on Medical Image Computing and Computer-Assisted Intervention*, pp. 1–8, Springer, 2012.
- Labarthe, S., Y. Coudière, J. Henry, and H. Cochet, A Semi-Automatic Method To Construct Atrial Fibre Structures : a Tool for Atrial Simulations, in *CinC 2012 - Computing in Cardiology*, vol. 39, pp. 881–884, 2012.
- Li, X., H. Chen, X. Qi, Q. Dou, C.-W. Fu, and P.-A. Heng, H-denseunet: hybrid densely connected unet for liver and tumor segmentation from ct volumes, *IEEE transactions on medical imaging*, 37(12), 2663–2674, 2018.

- Liryc, I., and Inria, Music: Multi-modality platform for specific imaging in cardiology, [Online; accessed 16-October-2019], 2019.
- Litjens, G., T. Kooi, B. E. Bejnordi, A. A. A. Setio, F. Ciompi, M. Ghafoorian, J. A. W. M. van der Laak, B. van Ginneken, and C. I. Sánchez, A survey on deep learning in medical image analysis, *Medical Image Analysis*, 42, 60–88, doi:10.1016/j.media.2017.07.005, 2017.
- Liu, J., Y. Pan, M. Li, Z. Chen, L. Tang, C. Lu, and J. Wang, Applications of deep learning to MRI images: A survey, *Big Data Mining and Analytics*, 1(1), 1–18, doi:10.26599/BDMA.2018.9020001, 2018.
- Lombaert, H., L. Grady, X. Pennec, N. Ayache, and F. Chriet, Spectral log-demons: diffeomorphic image registration with very large deformations, *International journal of computer vision*, 107(3), 254–271, 2014.
- Lorenzi, M., and X. Pennec, Efficient parallel transport of deformations in time series of images: from schild’s to pole ladder, *Journal of Mathematical Imaging and Vision*, 50(1-2), 5–17, 2014.
- Lorenzi, M., N. Ayache, and X. Pennec, Schild’s ladder for the parallel transport of deformations in time series of images, in *Biennial International Conference on Information Processing in Medical Imaging*, pp. 463–474, Springer, 2011.
- Louis, M., A. Bône, B. Charlier, S. Durrleman, A. D. N. Initiative, et al., Parallel transport in shape analysis: a scalable numerical scheme, in *International Conference on Geometric Science of Information*, pp. 29–37, Springer, 2017.
- Lupercio, F., J. C. Ruiz, D. F. Briceno, J. Romero, P. A. Villablanca, C. Berardi, R. Faillace, A. Krumerman, J. D. Fisher, K. Ferrick, et al., Left atrial appendage morphology assessment for risk stratification of embolic stroke in patients with atrial fibrillation: a meta-analysis, *Heart Rhythm*, 13(7), 1402–1409, 2016.
- Mansi, T., I. Voigt, B. Leonardi, X. Pennec, S. Durrleman, M. Sermesant, H. Delingette, A. M. Taylor, Y. Boudjemline, G. Pongiglione, et al., A statistical model for quantification and prediction of cardiac remodelling: Application to tetralogy of fallot, *IEEE transactions on medical imaging*, 30(9), 1605–1616, 2011.
- Marrouche, N. F., D. Wilber, G. Hindricks, P. Jais, N. Akoum, F. Marchlinski, E. Kholmovski, N. Burgon, N. Hu, L. Mont, et al., Association of atrial tissue fibrosis identified by delayed enhancement mri and atrial fibrillation catheter ablation: the decaaf study, *Journal of the American Medical Association (JAMA)*, 311(5), 498–506, 2014.
- McLeod, K., M. Sermesant, P. Beerbaum, and X. Pennec, Spatio-temporal tensor decomposition of a polyaffine motion model for a better analysis of pathological left ventricular dynamics, *IEEE transactions on medical imaging*, 34(7), 1562–1575, 2015.

- Miller, M. I., L. Younes, and A. Trouvé, Diffeomorphometry and geodesic positioning systems for human anatomy, *Technology*, 2(01), 36–43, 2014.
- Moceri, P., N. Duchateau, D. Baudouy, E.-D. Schouver, S. Leroy, F. Squara, E. Ferrari, and M. Sermesant, Three-dimensional right-ventricular regional deformation and survival in pulmonary hypertension, *European Heart Journal - Cardiovascular Imaging*, 2017.
- Morillo, C. A., A. Banerjee, P. Perel, D. Wood, and X. Jouven, Atrial fibrillation: the current epidemic, *Journal of geriatric cardiology: JGC*, 14(3), 195, 2017.
- Nedios, S., M. Tang, M. Roser, N. Solowjowa, J.-H. Gerds-Li, E. Fleck, and C. Kritselis, Characteristic changes of volume and three-dimensional structure of the left atrium in different forms of atrial fibrillation: predictive value after ablative treatment, *Journal of Interventional Cardiac Electrophysiology*, 32(2), 87–94, 2011.
- Nelson, A. J., M. I. Worthley, P. J. Psaltis, A. Carbone, B. K. Dundon, R. F. Duncan, C. Piantadosi, D. H. Lau, P. Sanders, G. A. Wittert, et al., Validation of cardiovascular magnetic resonance assessment of pericardial adipose tissue volume, *Journal of Cardiovascular Magnetic Resonance*, 11(1), 15, 2009.
- Oakes, R. S., T. J. Badger, E. G. Kholmovski, N. Akoum, N. S. Burgon, E. N. Fish, J. J. Blauer, S. N. Rao, E. V. DiBella, N. M. Segerson, et al., Detection and quantification of left atrial structural remodeling using delayed enhancement mri in patients with atrial fibrillation, *Circulation*, 119(13), 1758, 2009.
- Oktay, O., E. Ferrante, K. Kamnitsas, M. Heinrich, W. Bai, J. Caballero, S. A. Cook, A. De Marvao, T. Dawes, D. P. O’Regan, et al., Anatomically constrained neural networks (acnns): application to cardiac image enhancement and segmentation, *IEEE transactions on medical imaging*, 37(2), 384–395, 2017.
- OpenStax College, Anatomy & Physiology, [Online; accessed 12-November-2019], 2013.
- Pei, S.-C., C.-L. Lai, and F. Y. Shih, An efficient class of alternating sequential filters in morphology, *Graphical Models and Image Processing*, 59(2), 109–116, 1997.
- Pennec, X., Parallel transport with pole ladder: a third order scheme in affine connection spaces which is exact in affine symmetric spaces, *arXiv preprint arXiv:1805.11436*, 2018.
- Postnikov, M. M., *Geometry VI: Riemannian Geometry*, Encyclopaedia of Mathematical Sciences, Geometry, Springer-Verlag, Berlin Heidelberg, 2001.
- Qiu, A., L. Younes, M. I. Miller, and J. G. Csernansky, Parallel transport in diffeomorphisms distinguishes the time-dependent pattern of hippocampal surface deformation due to healthy aging and the dementia of the alzheimer’s type, *NeuroImage*, 40(1), 68–76, 2008.

- Rao, A., P. Aljabar, and D. Rueckert, Hierarchical statistical shape analysis and prediction of sub-cortical brain structures, *Medical image analysis*, 12(1), 55–68, 2008.
- Rohé, M.-M., M. Datar, T. Heimann, M. Sermesant, and X. Pennec, Svf-net: Learning deformable image registration using shape matching, in *International Conference on Medical Image Computing and Computer-Assisted Intervention*, pp. 266–274, Springer, 2017.
- Romero, J., S. A. Husain, I. Kelesidis, J. Sanz, H. M. Medina, and M. J. Garcia, Detection of left atrial appendage thrombus by cardiac computed tomography in patients with atrial fibrillation: a meta-analysis, *Circulation: Cardiovascular Imaging*, 6(2), 185–194, 2013.
- Ronneberger, O., P. Fischer, and T. Brox, U-net: Convolutional networks for biomedical image segmentation, in *International Conference on Medical image computing and computer-assisted intervention*, pp. 234–241, Springer, 2015.
- Sánchez-Quintana, D., J. A. Cabrera, V. Climent, J. Farré, M. C. de Mendonça, and S. Y. Ho, Anatomic relations between the esophagus and left atrium and relevance for ablation of atrial fibrillation, *Circulation*, 112(10), 1400–1405, 2005.
- Shapiro, L. G., and G. Stockman, *Computer Vision: Theory and Applications. 2001*, Prentice Hall, 2001.
- Shin, S.-H., M.-Y. Park, W.-J. Oh, S.-J. Hong, H.-N. Pak, W.-H. Song, D.-S. Lim, Y.-H. Kim, and W.-J. Shim, Left atrial volume is a predictor of atrial fibrillation recurrence after catheter ablation, *Journal of the American Society of Echocardiography*, 21(6), 697–702, 2008.
- Singh, K. K., and A. Singh, A study of image segmentation algorithms for different types of images, *International Journal of Computer Science Issues (IJCSI)*, 7(5), 414, 2010.
- Thanassoulis, G., J. M. Massaro, C. J. O’Donnell, U. Hoffmann, D. Levy, P. T. Ellinor, T. J. Wang, R. B. Schnabel, R. S. Vasan, C. S. Fox, et al., Pericardial fat is associated with prevalent atrial fibrillation: the framingham heart study, *Circulation: Arrhythmia and Electrophysiology*, 3(4), 345–350, 2010.
- Tobon-Gomez, C., J. Peters, J. Weese, K. Pinto, R. Karim, T. Schaeffter, R. Razavi, and K. S. Rhode, Left atrial segmentation challenge: a unified benchmarking framework, in *International Workshop on Statistical Atlases and Computational Models of the Heart*, pp. 1–13, Springer, 2013.
- Tops, L. F., J. J. Bax, K. Zeppenfeld, M. R. M. Jongbloed, H. J. Lamb, E. E. van der Wall, and M. J. Schalij, Fusion of multislice computed tomography imaging with three-dimensional electroanatomic mapping to guide radiofrequency catheter ablation procedures, *Heart Rhythm*, 2(10), 1076–1081, 2005.

- Tran, D., L. Bourdev, R. Fergus, L. Torresani, and M. Paluri, Learning spatiotemporal features with 3d convolutional networks, in *Proceedings of the IEEE international conference on computer vision*, pp. 4489–4497, 2015.
- Trouvé, A., Diffeomorphisms groups and pattern matching in image analysis, *International journal of computer vision*, 28(3), 213–221, 1998.
- Vaillant, M., and J. Glaunès, Surface matching via currents, in *Biennial International Conference on Information Processing in Medical Imaging*, pp. 381–392, Springer, 2005.
- Varela, M., C. Kolbitsch, A. Theron, R. Morgan, M. Henningsson, T. Schaeffter, and O. Aslanidi, 3D high-resolution atrial wall thickness maps using black-blood psir, *Journal of Cardiovascular Magnetic Resonance*, 17(1), 1, 2015.
- Varela, M., F. Bisbal, E. Zacur, A. Berruezo, O. V. Aslanidi, L. Mont, and P. Lamata, Novel computational analysis of left atrial anatomy improves prediction of atrial fibrillation recurrence after ablation, *Frontiers in Physiology*, 8, 68, 2017.
- Vercauteren, T., X. Pennec, A. Perchant, and N. Ayache, Symmetric log-domain diffeomorphic registration: A demons-based approach, in *International conference on medical image computing and computer-assisted intervention*, pp. 754–761, Springer, 2008.
- Verma, A., C.-y. Jiang, T. R. Betts, J. Chen, I. Deisenhofer, R. Mantovan, L. Macle, C. A. Morillo, W. Haverkamp, R. Weerasooriya, et al., Approaches to catheter ablation for persistent atrial fibrillation, *New England Journal of Medicine*, 372(19), 1812–1822, 2015.
- VTK, vtktrianglefilter class reference, 2016.
- Wapcaplet, Diagram of the human heart, [Online; accessed 12-November-2019], 2006.
- Wolf, F., P. Ourednicek, C. Loewe, B. Richter, H. D. Gössinger, M. Gwechenberger, C. Plank, R. E. Schernthaner, M. Toepker, J. Lammer, et al., Evaluation of left atrial function by multidetector computed tomography before left atrial radiofrequency-catheter ablation: comparison of a manual and automated 3d volume segmentation method, *European journal of radiology*, 75(2), e141–e146, 2010.
- Wong, C. X., H. S. Abed, P. Molaei, A. J. Nelson, A. G. Brooks, G. Sharma, D. P. Leong, D. H. Lau, M. E. Middeldorp, K. C. Roberts-Thomson, et al., Pericardial fat is associated with atrial fibrillation severity and ablation outcome, *Journal of the American College of Cardiology*, 57(17), 1745–1751, 2011.
- Younes, L., Jacobi fields in groups of diffeomorphisms and applications, *Quarterly of applied mathematics*, pp. 113–134, 2007.

- Zeiler, M. D., and R. Fergus, Visualizing and Understanding Convolutional Networks arXiv:1311.2901v3 [cs.CV] 28 Nov 2013, *Computer Vision–ECCV 2014*, 8689, 818–833, doi:10.1007/978-3-319-10590-1_53, 2014.
- Zhao, A., G. Balakrishnan, F. Durand, J. V. Guttag, and A. V. Dalca, Data augmentation using learned transformations for one-shot medical image segmentation, in *Proceedings of the IEEE Conference on Computer Vision and Pattern Recognition*, pp. 8543–8553, 2019.
- Zheng, Q., H. Delingette, N. Duchateau, and N. Ayache, 3-d consistent and robust segmentation of cardiac images by deep learning with spatial propagation, *IEEE transactions on medical imaging*, 37(9), 2137–2148, 2018.
- Zoni-Berisso, M., F. Lercari, T. Carazza, and S. Domenicucci, Epidemiology of atrial fibrillation: European perspective, *Clinical epidemiology*, 6, 213, 2014.